THE UNIVERSITY OF CHICAGO

ON THE FEASIBILITY OF POSITRON EMISSION TOMOGRAPHY IMAGING SYSTEMS UTILIZING MIXED SPATIAL RESOLUTION DETECTORS

A DISSERTATION SUBMITTED TO
THE FACULTY OF THE DIVISION OF THE BIOLOGICAL SCIENCES
AND THE PRITZKER SCHOOL OF MEDICINE
IN CANDIDACY FOR THE DEGREE OF
DOCTOR OF PHILOSOPHY

COMMITTEE ON MEDICAL PHYSICS

BY
NEVILLE ECLOV

CHICAGO, ILLINOIS
DECEMBER 2018

For Isobel, who reminds me every day of a brighter future,

and for Rachel, who lights up my present.

TABLE OF CONTENTS

LIST OF FIGURES

LIST OF TABLES

ACKNOWLEDGMENTS

I would like to thank my advisor Chien-Min Kao for his generosity, understanding, patience, and encouragement as I pursued my studies. He gave me direction when I needed inspiration, freedom when I wanted to pursue new ideas, and a contagious positivity when I was discouraged. Thank you for getting me across the finish line.

I am grateful for the mentorship of my committee members: Chin-Tu Chen for exposure to his expertise in nuclear medicine and Xiaochuan Pan for sharing his expansive knowledge of image reconstruction. I would also like to thank the faculty of the GPMP for their teaching and advice, especially Bill O'Brien-Penney for his invaluable perspective on clinical nuclear medicine.

Many thanks to my friends and fellow students with whom I have shared this journey. From constructive discussions in the Collaboratorium to Friday nights on the softball field, the fun and camaraderie helped me through the more difficult days.

I would not be where I am today without the love and support of my parents. My father instilled a love of physics starting in kindergarten, and my mom showed me every day the reward that is working to help others. Thank you to my daughter Isobel for the smiles that cheered up long days.

Finally, thank you to my wife Rachel, the first Dr. Eclov in our family. The insight from her own PhD helped me push through the tough times and ask the right questions. Words cannot express what your love, patience and support have meant.

ABSTRACT

Positron emission tomography (PET) is a powerful molecular imaging modality used to address a wide assortment of pathologies, including cancer, neurodegenerative diseases, psychiatric conditions, and cardiac disease. It is capable of providing specific and quantitative information about biological processes, but this capability is dependent on its ability to resolve regions of interest in the body accurately. In recent years, while preclinical and research systems have pushed spatial resolution capability toward sub-millimeter levels, improvements in spatial resolution performance for clinical PET systems have plateaued at around 4 mm due to practical constraints on cost and engineering complexity. However, resolution performance better than 4 mm is desirable to multiple applications in brain, breast, prostate and pediatric PET imaging among others. Therefore, alternative strategies to boost spatial resolution performance in at least part of the imaging field of view (FOV) are of interest.

The work presented examined the feasibility of replacing some fraction of a standard resolution scanner's detectors with higher spatial resolution detectors as a method to improve spatial resolution performance, generating data containing a mix of the resolution properties of the different detectors. Two scanner configurations were investigated: (1) a scanner configuration with a centrally located region of high resolution detectors and (2) a scanner configuration with an end-located region of high resolution detectors.

In order to account for the mixed intrinsic resolution properties of the collected data from these geometries, a three-dimensional iterative maximum likelihood expectation maximization reconstruction method was developed and validated. The algorithm employed a ray-tracing projection method using CPU multithreading for speed up in order to flexibly calculate system matrices for the different scanner geometries studied. An image-space resolution model created from sparse axial sampling of the point system responses along the axial FOV was used to account for the variable spatial resolution caused by the mixed resolution data. Reconstructions using this model demonstrated improved resolution performance

compared to those without.

Each of the mixed resolution scanner configurations examined were compared to scanners using a single type of spatial resolution detector, either high or standard. The standard resolution systems had the same overall geometry as the mixed resolution systems but had uniformly lower resolution detectors and was used to evaluate the improvements in spatial resolution performance of the mixed resolution systems. In order to understand the sensitivity benefits of additional but lower resolution lines of response of the mixed resolution systems, the compared high resolution systems had the same geometry as the high resolution detector module region of the corresponding mixed resolution system. Studies evaluating sensitivity, spatial resolution performance and contrast recovery showed advantages of the mixed resolution systems.

Initial work on an evaluation system using a transformable gantry was performed. Data acquisition software was developed for a four-module system of high resolution detectors arranged in a box-like geometry. Further development and characterization of this system is ongoing with the goal of validating the mixed resolution concept using real data.

In summary, this work developed methods to study the feasibility of a mixed resolution PET scanner geometry and evaluated two candidate system geometries, determining that mixed resolution systems have potential benefits in terms of both sensitivity and spatial resolution performance. Initial work was performed developing an evaluation system for real data validation.

CHAPTER 1

INTRODUCTION

1.1 Overview of Positron Emission Tomography

Positron emission tomography (PET) is common nuclear medicine imaging technique favored because of its ability to provide quantitative information about biological processes in the human body. PET combines the principles of radiotracer kinetics and tomographic imaging and applies them to data acquired from positron emitting particles in the body. These particles can be linked to targeted molecules or biologics of interest such that imaging their location provides information specific to some physiological mechanism *in vivo*. The most prevalent example of a radiolabeled molecule used in 90% of routine PET studies [37], to the extent that it has become almost synonymous with the modality itself, is fluorodeoxyglucose or ^{18}F-FDG. ^{18}F-FDG provides information about glucose metabolism that is useful for studying a whole host of disease processes.

The radiotracer principle used in PET was originally developed by George de Hevesy, who received the Nobel Prize for his work, in the early 1900s [117]. Because radioactive particles participate in physiological processes in much the same way as non-radioactive particles, trace amounts of radioactive substance can be incorporated in the body and detected without disturbing the existing state one hopes to study. Briefly, a radionclide-labeled agent, also known as a radiotracer or radiopharmaceutical, is introduced into the subject in very small quantitities and is carried through the body following the biokinetic patterns of the agent it is designed to mimic. PET data from external measurement of emitted 511 keV photons after positron emission can be acquired throughout the process of biodistribution of the radiotracer and reconstructed into images showing the tracer's spatial distribution. The presence or absence of radiotracer signal can provide strong indications about biological processes, both normal and diseased. For instance, uptake of ^{18}F-FDG in a lymph node

for a patient already diagnosed with a cancer can indicate that disease progression has occurred, potentially leading to a change in treatment. Such information might not be available from standard anatomical imaging modalities like computed tomography (CT) or magnetic resonance imaging (MRI) and highlights the important role of functional and molecular imaging techniques like PET in clinical decision-making.

While de Hevesy used naturally occurring radioisotopes, we are now able to manufacture specialized radioactive compounds and attach them to an ever-growing list of targeted agents. Of the positron-emitting particles that exist, common ones found in PET radiotracers include ^{18}F, ^{11}C, ^{15}O, ^{13}N due to their biocompatibility. During a PET scan, one of these radioisotopes is put into the body and begins emitting positrons, which travel a short distance in the body before annihilating with an electron and creating two 511 keV photons, which travel in nearly opposite directions. Due to their high energy, a large fraction of these photons will make it out of the body to the PET detection system. If both photons from a single positron annihilation are detected, one knows the path along which the event occurred, and by collecting hundreds of thousands to millions of photon pairs, one can use tomographic methods to reconstruct the three-dimensional distribution of the emitter in the body.

1.2 Utility and Challenges of PET Imaging

PET is primarily useful because it fills (along with single photon emission computed tomography, or SPECT) the functional and molecular imaging void left by the other main medical imaging modalities CT and MRI, which are primarily anatomical or structural imaging techniques (though functional or molecular imaging techniques for both are available). For a variety of disease processes, biological and physiological changes that can be imaged by a molecular imaging technique like PET can occur months or even years before anatomical changes that are visible using standard x-ray, CT or MRI. The information provided by PET

can help assess disease severity, inform a differential diagnosis not provided by anatomical imaging, or provide diagnosis of disease prior to it causing any anatomical changes.

The clinical role of PET, at present almost entirely performed by ^{18}F-FDG, is primarily seen in three areas: cancer diagnosis and management, cardiology, and neurological and psychiatric evaluation. In cancer, PET is used for many of the most common types of cancer in order to diagnose disease, grade the malignancy of specific disease sites, stage the overall state of the disease, find residual disease after surgery, detect recurrence, and evaluate response of the disease to therapeutic intervention. PET's wide-ranging role in cancer care is the primary utilization of PET systems in clinics today. In cardiology, PET is used in making two important physiological measurements of cardiac health: myocardial perfusion (using ^{13}N-ammonia or ^{82}Rb) and myocardial viability (using ^{18}F-FDG). These measurements are used to characterize the severity of coronary artery disease (CAD), to assess the viability of damaged myocardial tissue, and in the work-up of patients under consideration for cardiac tranplantation. For neurological and psychiatric evaluations, PET is seeing an increasing role in the diagnosis of dementias using newly developed amyloid-, tau-, and neuroinflammation-targeting radiotracers [50]. PET also is used in the management of epilepsy and tumors causing neo-plastic syndromes. Beyond these three areas, researchers are actively pushing PET into new areas of medicine every day as scanners and radiotracers become more generally available, a growth driven by their heavy use in the three areas mentioned above.

While PET is increasingly used in the clinic and has the potential for even more use with the advent of the personalized medicine, personalized health, and molecular imaging paradigms, many challenges exist that could slow or prevent that broader utilization of PET. Particularly, PET system's high cost, poor spatial resolution (compared to modalities like CT and MRI), and low SNR stand as major barriers.

First, cost affects the kinds of PET systems that can be built and made affordable for

hospitals and clinics. A typical clinical PET scanner costs several million dollars, with photodetectors, readout electronics and scintillation crystal all contributing to the high cost. While the cost of scintillator is almost necessarily fixed due to the crystal's overall importance in determining system sensitivity, the detector and electronics can vary substantially in performance and cost. However, in general cost considerations serve to limit the hardware available for the detector modules and the size of the imaging FOV, since larger scanners require more materials. Morevoer, these considerations do not include the cost of additional infrastructure required to produce clinical-grade radiopharmaceuticals.

There is a joke in the medical imaging field that nuclear medicine is often referred to as "unclear" medicine, an unflattering reference to SPECT and PET's generally worse spatial resolution and SNR performance compared to other imaging modalities. In PET, poor spatial resolution results in reduced image contrast and the partial volume effect, which create problems for detecting small and low-contrast objects and introduce artifacts in the quantitiation of biological parameters of interest. To overcome this, system designers generally attempt to incorporate smaller individual detector elements and advanced hardware to refine knowledge of the timing and location of detected events. These efforts contribute to the cost mentioned in the previous paragraph, but also introduce engineering challenges as more detector channels are introduced and more data is collected, requiring advanced readout methods for the detectors as well. An entire area of PET research is devoted to reducing the size and expense of detector readout hardware.

Beyond developments in hardware, there have been consistent efforts to improve image quality in PET by developing better image reconstruction methods, especially techniques making use of knowledge of the physics and statistical properties of the detection process. Development of fast, iterative reconstruction algorithms based on expectation-maximization and other optimization methods have led to the widespread replacement of the previous standard filtered backprojection (FBP) algorithm in clinical systems, which has been demon-

strated to provide both qualitatively and quantitatively inferior image quality. The general growth in compuational speed has also meant a transition from two-dimensional reconstruction to three-dimensional reconstruction techniques, which makes better use of the full sensitivity of PET systems when performing image reconstruction. While these efforts have born fruit in improved image quality, more work on choosing the appropriate algorithm and noise controls for specific imaging tasks remains in order to realize the full benefits of these techniques.

1.3 Objectives of the Present Work

In order to address issues of cost and spatial resolution performance mentioned in the previous section, in this work we propose a new PET scanner geometry which combines detector modules with different intrinsic resolution properties. We propose this approach to incorporate higher resolution performance into PET systems but to do so without increasing the overall cost of the scanner by as much as developing an entire system out of high resolution detectors.

We expect a mixed resolution scanner will be able to provide high resolution performance in the sub-volume encompassed by the high resolution detectors, with resolution performance gradually relaxing to the lower resolution performance in regions under the lower spatial resolution detector modules. However, the ability to achieve this spatial resolution performance is determined by the method by which the image reconstruction algorithm accounts for the difference in spatial resolution between different detector pairs as well as the specific geometry of the system under consideration.

Specific objectives of the research described in this dissertation are: (1) to develop reconstruction methods capable of using and realizing the benefit of incorporating mixed spatial resolution data; (2) to understand the potential performance benefits of mixed resolution systems compared to systems with uniform detector size, whether high or standard resolu-

tion; and (3) to evaluate the specific advantages and challenges of some different potential system geometries for mixed resolution PET systems.

1.4 Organization of the Dissertation

The rest of this dissertation is organized according to the following scheme. The technical concepts underlying PET's role as a successful medical imaging modality are laid out in Chapter 2, including discussions of PET system design, modeling the PET imaging chain, and image reconstruction. Efforts to improve engineering limitations on spatial resolution performance are also detailed, leading to the proposal of the mixed spatial resolution PET system under consideration in this work. In Chapter 3, simulation and image reconstruction tools for studying mixed spatial resolution PET systems are developed and validated. An image reconstruction algorithm is developed to account for the combination of intrinsic spatial resolution properties of the data acquired by mixed resolution systems. With these methods in hand, we move on in Chapter 4 to examine the feasibility of a specific mixed spatial resolution design incorporating a centrally located region of high resolution detectors sandwiched axially between two sections of standard resolution detectors. The performance is judged relative to two other PET systems, one using only high resolution detectors and one using only standard resolution detectors. In Chapter 5, an alternative mixed resolution detector geometry is explored which incorporates the high resolution performance region at one end of the axial extent of the detector, a configuration which has a separate set of potential applications and challenges. Chapter 6 presents initial developments in building and evaluating a mixed resolution evaluation system on a transformable gantry. Chapter 7 summarizes the results of this work and discusses potential future avenues of research for this mixed resolution concept.

CHAPTER 2

BACKGROUND

In this chapter, the physics of PET imaging and the challenges of PET system design are reviewed. In Section 2.1, we describe the concepts underlying PET imaging and a simple model of the imaging process. Section 2.2 covers the rationale for system design choices in PET and describes detector instrumentation limitations which complicate this ideal imaging model, and a more reaslistic model for how we detect events in PET systems is outlined in Section 2.3, along with a discussion of deviations from this model and potential refinements. Section 2.4 discusses common image reconstruction techniques for PET. We then move on to examine spatial resolution performance of PET systems in Section 2.5, including nontraditional PET system geometries to improve resolution compared to standard cylindrical PET systems.

2.1 Fundamental Principles of PET Imaging

2.1.1 Principle of Coincidence Detection

The underlying principle of PET imaging is coincidence detection, which is depicted in Figure 2.1. A radioactive positron-emitting isotope introduced into the subject releases a positron, which loses energy through local ionization, encounters an electron and annihilates, releasing two 511 keV gamma ray which travel in directions approximately opposite from each other. If the gamma rays reach the detection system, they may be detected by interacting in one of two ways: (1) a Compton scattering event in which some of the gamma ray's energy is deposited in the crystal emitting optical photons while the rest of the energy is remitted as secondary gamma rays which may be absorbed in another crystal, or (2) a photoelectric interaction where all of the 511 keV gamma ray's energy is deposited in the crystal, resulting in optical photon emission. Gamma rays may also pass through the detector altogether, but

if detected, each is recorded as a "single" event with a corresponding energy and time. Two singles events, if they fall in the right energy range and are detected nearly simultaneously, can paired together as a coincidence event corresponding to a pair of detectors and the line connecting them, which is known as the line of response (LOR).

While some coincidence events are "true" coincidence events emanating from the same annihilation event along the detected LOR, coincidence events can also be designated as "random" or "scatter". Random coincidence events occur when two singles events are detected simultaneously but were emitted from separate positron annihilations, resulting in a false event along the specified LOR. Scatter coincidence events occur when one or both of the two 511 keV gamma rays from the same positron emission undergo Compton scattering away from their original path before reaching the detector, resulting in a misidentification of the LOR upon which the positron emission occurred. While trues and scatter events originate from the same positron emission and are therefore proportional to the the singles event rate, randoms are proportional to the square of the singles rate and become more prominent with higher detected event rates.

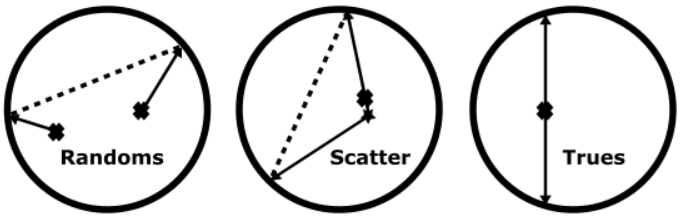

Figure 2.1: The three types of coincidence events. As depicted, randoms and scatter events lead to the identification of incorrect lines of response (LOR).

Coincidence detection localizing an event to a LOR occurs electronically, either in hardware by a coincidence circuit or via utilizing a computer algorithm on singles data. This spares PET imaging from the use of collimators to localize the source of the gamma ray emission as is required for single photon emission computed tomography (SPECT). This is

significant because collimators reduce the solid angle of detection covered by detectors and also reduce by attenuation the number of gamma rays that arrive at the detector. Both of these result in inferior sensitivity for SPECT when compared to the electronic collimation performed in PET. Because of this sensitivity advantage, PET systems can use smaller individual detector elements to achieve higher spatial resolution and quantitative measurement.

Another advantage that coincidence detection provides is it simplifies attenuation correction. For any emission tomography system, a proportion of gamma rays traveling through the imaged subject can be attenuated inside the subject and never reach a detector. For PET, each 511 keV gamma ray must reach the detector, and the probability of detection of a true event given a path ℓ through the subject and assuming perfect detection efficiency can be described by

$$e^{-\int_{\ell_1} \mu(\mathbf{r}) d\gamma} \times e^{-\int_{\ell_2} \mu(\mathbf{r}) d\gamma} = e^{-\int_{\ell} \mu(\mathbf{r}) d\gamma}, \tag{2.1}$$

where $\mu(\mathbf{r})$ is the attenuation coefficient for a 511 keV gamma ray at $\mathbf{r}$ within the imaged subject, and the integrals over the line between the annihilation event and the detector for each photon ℓ_1 and ℓ_2, and the LOR we assume, ℓ, which is the line between the detectors. Because the attenuation does not depend on the location of the event along the LOR, the attenuation for gamma ray pairs traveling on each LOR can be accounted for using attenuation coeffecient maps of the subject derived from CT images, the current standard of care for clinical PET. However, in SPECT, the attenuation of gamma rays is dependent on the depth of the source in the subject, and accounting for it becomes quite complicated and puts limitation on quantitative accuracy in SPECT.

2.1.2 Model of Ideal PET Imaging System

The following describes an idealized PET imaging system following the example of Kao [55]. The expected number of coincidence events measured by a detector pair during a time

interval T (and accounting for the attenuation factor described in Equation 2.1) is given by

$$E\left\{y^{[T]}\right\} = \int_T \int_\ell f\left(\mathbf{r},t\right) e^{-\int_\ell \mu(\mathbf{r}) d\gamma'} d\gamma dt = \left\{\int_\ell f^{[T]}\left(\mathbf{r}\right) d\gamma\right\} e^{-\int_\ell \mu(\mathbf{r}) d\gamma'}, \tag{2.2}$$

where $f^{[T]}\left(\mathbf{r}\right) = \int_T f\left(\mathbf{r},t\right) dt$ and $f\left(\mathbf{r},t\right)$ is the spatial distribution of positron sources at time t. Because the detection of events is a Poisson process, the measured counts $y^{[T]}$ is a random variable with a probability distribution following

$$p\left(y^{[T]}\right) = \frac{E\left\{y^{[T]}\right\}^{y^{[T]}} e^{-E\left\{y^{[T]}\right\}}}{y^{[T]}!}. \tag{2.3}$$

We can now rewrite Equation 2.2

$$y^{[T]} = \mu_\ell \int_\ell f^{[T]}\left(\mathbf{r}\right) d\gamma + \xi^{[T]}, \tag{2.4}$$

where $\mu_\ell = e^{-\int_\ell \mu(\mathbf{r}) d\gamma}$ accounts for attenuation and $\xi^{[T]}$ accounts for the Poisson measurement noise. This can be thought of as a zero-mean, signal-dependent random variable with a variance of $E\left\{y^{[T]}\right\}$. While this idealized model misses many of the complicating factors that make PET imaging a challenging field, it demonstrates the processes underlying PET imaging which we will build upon in the review that follows.

2.2 Design of PET Systems

2.2.1 Determining a Geometry

While nearly all clinical PET systems are roughly cylindrical in design, there are some variations in how this geometry is achieved. One method is to use an array of large, continuous flat-panel detector modules oriented in an octagonal or other higher-order-polygonal-shape similar to the early PENN-PET system [57]. Another method, utilized by the RPT-2 sys-

tem [110], is to use two opposed partial rings of detector blocks and rotate them to get an adequate sampling of the imaged object. By far the most common method adopted by essentially all modern clinical PET systems is to use an array of discrete scintillating crystals organized into multiple modules to more finely approximate a cylindrical shape that represents the ideal imaging model for reconstruction. While systems with other geometries exist and many variations have been proposed (some of which will be discussed in Section 2.5), they are in the minority.

Originally PET systems operated primarily in two-dimensional(2D) mode with collimation in the axial direction. While three-dimensional (3D) mode was frequently available, 2D was preferred due to reductions in scatter and limitations in detector technology that made constraining acquired data to a single plane desirable (i.e. straightforward and computationally inexpensive 2D image reconstruction). However, septa used for collimation also greatly reduced sensitivity, and so beginning in the 1990s with advances in fully 3D reconstruction and scatter correction methods [21, 22, 27, 29, 112], PET systems began to transition away from septas such that today septaless, 3D scans are the regular protocol.

2.2.2 Factors in Event Detection

A typical PET detector is made up of a scintillation crystal (or array of crystals) optically coupled to a photodetector. Energy deposited by a gamma ray interacting with the scintillation crystal is converted to visible light which propagates through the crystal to the photodetector. Traditionally the photodetector has been a photomultiplier tube (PMT) as part of a "block detector", with PMTs sharing and accepting light from multiple crystals to enable event position decoding via an adapted Anger logic [5, 67]. At the PMT, the scintillation light from the crystal is converted into photoelectrons which are amplified and become an electrical pulse read out by data acquisition electronics. Current state-of-the-art systems have replaced PMTs with solid-state silicon-photomultipliers (SiPMs) or avalanche

photodiodes (APDs) with the potential for one-to-one coupling between scintillator and photodetector. Regardless of the photodetector type, the pulse generated in the scintillator has a fast rise time (important for timing resolution) and a long tail that decays at a characteristic rate for the scintillator material (important for count rate performance). We can calculate the energy of the detected gamma ray by integrating the area under the pulse and the arrival time using a threshold criteria for the rising edge. If the detected gamma ray has an energy above some predetermined threshold and occurs at the same time as another event in a separate detector, it is registered as a coincident event.

Because the emitted gamma rays have an energy of 511 keV, their primary mode of interaction as they travel to the detector is Compton scattering. We would like to omit these scattered events, which are lower energy than the original 511 keV gamma, from our data, and so energy discrimination using a fixed energy window is employed to reduce low-energy events in the data. For older systems using BGO scintillators, typical thresholds of 350 keV were used, but with more modern Lutetium-based scintillators, current clinical systems use thresholds above 400-450 keV [113, 31, 90]. Extremely narrow energy windows (i.e. accepting *only* 511 keV photons) are not used due to limitations of most detectors. Uncertainty in the measured energy of the incoming gamma is determined by the number of scintillation photons generated and that reach the photodetector, and this uncertainty generally comes in the form of a Gaussian distribution of some full width at half maximum (FWHM) around the 511 keV peak. This FWHM is taken to be the energy resolution of the detector. In addition to this measurement uncertainty, if scintillation crystal elements are small enough (desirable for higher spatial resolution performance), photons can Compton scatter in a crystal, depositing some energy, before escaping the crystal altogether. An energy window that is too tight would reject these desirable events and reduce sensitivity.

Fast timing measurement performance of the detector is also essential for PET systems. Each electronic pulse generated by an event's scintillation photons' interaction with the

photodetector has a pulse shape and duration τ directly related to the event time of the gamma ray interaction in the scintillator. Since coincidences occur when two such pulses overlap, we define a quantity 2τ as the coincidence resolving time (CRT), in which if any two events are detected, they are considered coincident. Generally a small CRT is desirable since allowing longer windows for coincidence increases the likelihood that a gamma ray from an unrelated (or *random*) annihilation event will be determined coincident. However, the CRT cannot be too small due to uncertainties in time measurement by the detector electronics. Moreover, one must account for the time required of each photon to arrive at a detector given the physical size of the field-of-view (FOV). This condition would require the 70 cm FOV Philips Gemini TF scanner to have a CRT of at least 4.7 ns, and it is reported to use a coincidence window of 6 ns [113]. Current state-of-the-art clinical systems report coincidence windows between 4.1-4.9 ns [113].

2.2.3 Detector Module Design

In designing PET detector modules, choosing the right scintillation material, photodetector, and readout method and electronics are paramount in determining the imaging performance of the entire system. Table 2.1 shows the physical properties of some scintillators used in PET. In the last few decades, the two primary scintillators used for clinical PET applications have been bismuth germanate (BGO) and the class of lutetium-based scintillators, including lutetium oxyorthosilicate (LSO), lutetium-yttrium oxyorthosilicate (LYSO), and lutetium fine silicate (LFS). BGO was the original choice for widespread use in PET systems due to its high effective atomic number (Z = 74), availability, cost-effectiveness, and ease-of-machining. BGO's high effective atomic number results in more 511 keV photons undergoing photoelectric interactions in the scintillator, reducing intercrystal scatter and crystal penetration. However, BGO's timing performance due to it's relatively long decay constant (300 ns) and low light yield (15% of Na(Tl)) led to the development of the lutetium-based scin-

	Na(Tl)	BaF_2	BGO	LSO	GSO	LYSO	$LaBr_3$	LFS
Effective atomic number (Z)	51	54	74	66	59	60	47	63
Linear attenuation coefficient (cm^{-1})	0.34	0.44	0.92	0.87	0.62	0.86	0.47	0.82
Density (gm/cm^3)	3.67	4.89	7.13	7.4	6.7	7.1	5.3	7.3
Index of refraction	1.85	-	2.15	1.82	1.85	1.81	1.88	1.78
Light yield (% Na(Tl))	100	5	15	75	30	80	160	77
Peak wavelength (nm)	410	220	480	420	430	420	370	430
Decay constant (ns)	230	0.8	300	40	65	41	25	35
Hydroscopic	Yes	Slight	No	No	No	No	No	No

Table 2.1: Basic properties of some scintillators used in PET [67].

tillators and their eventual supplanting of BGO as the primary scintillator in clinical PET systems. While these scintillators have lower effective atomic number, their primary advantages include a light output approximately five times higher and a decay constant an order of magnitude less than that of BGO. Higher light yield has meant more precise measurements of event time due to increased signal from the scintillator for each event while shorter decay has greatly reduced PET systems CRTs. However, because the raw materials to manufacture lutetium-based scintillators are very expensive, use of these crystals contribute substantially to the overall cost of PET systems. For this reason, there has been renewed interest in getting better timing performance from BGO scintillators using the proposed Cerenkov light mechanism for fast timing performance [64, 15]

The traditional workhorse photodetector of emission tomography has long been the PMT due to its proven strong amplification properties and reliability. Especially in the period when BGO was the primary scintillator used for PET imaging, several PMTs were coupled to multiple individual BGO crystals or a single BGO crystal cut in a way to allow for event

position detection. This arrangement, known as a "block detector", allowed the low light yield of BGO to be amplified by multiple PMTs (typically 4) to improve the overall signal for each pulse. The readout method then used a variant of Anger logic to decode the position of the pulse in the crystals [67]. The GE Discover IQ PET/CT is one of the few systems still using BGO block detectors. Each block consists of an 8×8 matrix of 6.3×6.3×30 mm^3 BGO crystals coupled to 4 PMTs and shared among them via a light guide [92]. The downside of this approach is the the potential for a long dead-time for the entire block detector when any event occurs in one crystal. There are also position decoding errors that remain due to the limited statistics of sharing the low light yield among several detectors.

The alternative approach to the block detector is coupling photodetectors one-to-one with scintillation crystals. This dispenses with position decoding via Anger logic and can potentially avoid the issue of dead-time for surrounding detectors depending on the electronics readout method for the photodetector. Therefore, one-to-one coupling is expected to yield higher resolution performance for the same size crystal element and better count rate performance, increasing overall sensitivity. On the other hand, it is more expensive as it requires many more individual detector elements.

Modern systems are also pairing lutetium-based scintillators with a transition to solid-state photodetectors like APDs or SiPMs, for which a full review can be found in [93]. These silicon detectors have several added benefits in that they are physically much smaller than PMTs, do not require the same high operation voltages as PMTs, and are generally compatible for use in MR imaging systems. APDs have some operational challenges since they require cooling for adequate signal-to-noise and careful bias voltage and temperature control for stable operation, since both strongly affect the generated pulse [93]. Nonetheless, APDs were used to make the PET/MR hybrid Siemens Biograph mMR scanner [44]. However, SiPMs appear to be the photodetector of choice for high performance PET systems going forward, with recent clinical system releases from Philips (the Vereos PET/CT) and GE

(the Signa PET/MR), as well as a prototype system from Siemens [17], all utilizing SiPMs. SiPMs provide equal or more gain than PMTs but operate at bias voltages of less than 100 V, and they do not require cooling for adequate signal-to-noise performance in many applications, unlike APDs. Excellent timing performance is also reported [40]. The Philips Vereos PET/CT combines specialized photon-counting digital-SiPMs (dSiPMs) with one-to-one coupling to LYSO scintillator elements [73]. However, despite these advances reaching clinical systems, cost remains a significant barrier to further development of detector technology, which is why less costly scanners using traditional block detectors and BGO are still available.

2.3 Detection Model for 3D PET Systems

2.3.1 Factors Affecting Spatial Resolution

Spatial resolution in PET is determined by several factors, including detector size, positron range, acollinearity, detected position decoding, crystal penetration, and sampling error [74]. The intrinsic spatial resolution of two opposed detector elements of the same size is symmetric around the central point between them, with its shape approaching a triangle at the center and a rectangle at either end. For positions in between, the profile is approximately a trapezoid. The width of the base of the profile is the width of the detector element, w, whereas the width at the peak of the profile is determined by the distance between the crossed lines connecting opposite sides of the detectors. At the center, the peak has a width of zero which extends to w at the edge of the system. This implies that the full width at half maximum (FWHM) of the detection profile is $\frac{w}{2}$ at the center and w near the edge.

Blurring due to positron range occurs because of the remaining kinetic energy of the positron when it is ejected from the nucleus. Usually, the energy is a few MeV, and as a result the positron travels some distance from its emitted location before thermalizing and

capturing an electron to form positronium. The positronium then decays, releasing the two 511 keV gamma rays. The difference between the positron and gamma ray emission locations causes a blurring, and the potential range of the positron and its subsequent blurring is determined by the parent isotope. Table 2.2 shows some ranges for positron-emitting isotopes commonly used in PET.

Isotope	Endpoint Energy (MeV)	FWHM (mm)
^{18}F	0.64	0.54
^{11}C	0.96	0.92
^{13}N	1.22	1.49
^{15}O	1.72	2.48
^{68}Ga	1.90	2.83
^{82}Rb	3.35	6.14

Table 2.2: Contributions to spatial resolution performance from positron range for some commonly used radioisotopes for PET [74].

When the positronium decays into two 511 keV gamma rays it has non-zero kinetic energy, and though the gamma rays are emitted at 180° in the positronium reference frame, in the lab frame the gamma rays are emitted with a slight acollinearity, for which the mean value is reported in the range of 0.25° and 0.5° FWHM [26, 28]. The subsequent angular uncertainty results in a Gaussian blurring factor proportional to the distance between the emission location and the detectors. For resolution at the center of the scanner, this is often expressed as a blur equal to $0.0022 \cdot D$ (in FWHM) where D is the diameter of the scanner, but it can also be written more generally as

$$R_{180^\circ} = 0.0088 \cdot \frac{d_1 \cdot d_2}{d_1 + d_2}, \tag{2.5}$$

where d_1 and d_2 are the distances from the emission location to the detectors for gamma rays 1 and 2, respectively [106]. This implies that when the emission occurs very close to one of the detectors, $d_1 >> d_2$, and the blur can be much smaller than the canonical $0.0022 \cdot D$.

Other sources of resolution degradation stem from errors in decoding the detected position of gamma ray at the detector. One cause is the use of optical multiplexing to reduce the number of photodetectors per scintillation detector element in each detector module. This factor can reasonably be modeled as a Gaussian blur of $\frac{w}{3}$ where w is the width of the scintillation crystal element [74], and for systems where each scintillator is coupled one-to-one with a single photodetector, no decoding is necessary and the blur is zero. Another cause of crystal misidentification is the potential penetration of the gamma ray laterally through the first crystal it encounters and into its neighboring crystals before it is detected. The event is then assigned to the "wrong" location and LOR. The resulting "depth-of-interaction" blur or "parallax error" occurs in the radial direction, increasing as the point of the gamma ray emission occurs closer to the edge of the field of view [33, 46] . Quantitative values depend on the detector, but for commonly used LSO scintillators, it is a Gaussian function with a FWHM (in mm) given by $\frac{12.5r}{\sqrt{r^2+R^2}}$ [74]. This blur can also occur axially in scanners utilizing 3D reconstruction that include oblique LORs. Finally there is a factor to account for the non-uniform sampling of the field of view (FOV). Voxels are intersected by many or few LORs depending on their location within the FOV, and the resulting blur from undersampling and oversampling different parts of the FOV has been empirically found to multiply the other contributions by 1.25 [33] for cylindrical systems.

Altogether, though not all of the factors contributing to spatial resolution blurring are Gaussian, they are considered to add in quadrature such that, for a point source at distance r from the FOV's center, the FWHM in mm is

$$PSF = 1.25 \cdot \sqrt{\left(\frac{w}{2}\right)^2 + s^2 + \left(0.0088 \cdot \frac{d_1 \cdot d_2}{d_1 + d_2}\right)^2 + b^2 + \frac{(12.5r)^2}{r^2 + R^2}}, \tag{2.6}$$

where the 1.25 multiplier derives from the sampling error, w is the width of the detector element, s is the FWHM of the positron range effect, d_1 and d_2 are the distances of the source to detector 1 and 2, respectively, b is the factor due to position decoding (zero for one-to-one coupling of crystal to photodetector or $\frac{w}{3}$ for optical multiplexing between multiple crystals and one photodetector), and R is the radius of the scanner.

2.3.2 Scatter and Randoms

As described in Section 2.1, scatter coincidence events (or *scatter*) and random coincidence events (or *randoms*) both result in event data that introduces errors among the true coincidence events (or *trues*), and these types of events are two of the chief sources of noise in PET imaging. Scatter and randoms can be subtracted from the coincidence data before image reconstruction, but correction procedures worsen the statistics of the data and can require increased smoothing in image reconstruction to reduce the variance, which in turn degrades spatial resolution performance. Ideally, we try to reduce the sensitivity to scatter and randoms in the design process of any PET system, while also increasing the sensitivity to trues. One metric commonly used to assess this performance is the noise equivalent count rate (NECR), which relates image signal-to-noise with the count rates of scatter, randoms and trues [103]. NECR is defined as

$$NECR = \frac{T^2}{T + S + kR}, \tag{2.7}$$

where T, S, and R represent the count rates for trues, scatter, and randoms, respectively, and k is $1 < k < 2$, depending on if the randoms estimate is derived from the singles rates or a short delayed-coincidence window (to be discussed below).

There are many methods to reduce the contribution of scatter and randoms. For scatter, at a basic level one can try to limit scatter by using collimation, but this is rejected in most

modern scanners to retain sensitivity and perform 3D reconstruction. One can also increase the lower bound on the energy window used to select potential coincident events, but this is dependent on the energy resolution of the scanner. The original generation of 2D BGO-based commercial PET-CT scanners used energy windows around 350 keV, which resulted in a scatter fraction, $\frac{S}{T+S}$, of around 10-15%. Most modern scanners have an energy resolution of approximately $10-15\%$ and do not use collimation, resulting in scatter fractions in the range of 40% [48]. Given these higher levels of scatter for modern PET systems, more involved methods for scatter compensation are required, and, following Zaidi *et al.* [126, 125], these methods can generally be divided into 5 categories: (1) hardware approaches using coarse septa or beam stoppers; (2) multiple energy-window (spectral-analytic) approaches; (3) convolution/deconvolution-based approaches; (4) approaches based on direct estimation of scatter distribution; and (5) approaches based on statistical reconstruction. Comparative evaluation studies of these methods have concluded that nearly all correction methods improve image contrast substantially compared with no correction, but any method involving subtraction from the data also decreases the signal-to-noise ratio [126].

For randoms, as noted previously, the rate of random coincidences is proportional to the singles rates of the two coincident detectors. It can be expressed as

$$R = 2\tau S_1 S_2 \tag{2.8}$$

where S_1 and S_2 are the singles rates for detectors 1 and 2, and 2τ is the coincidence resolving time. While the singles, trues and scatter rate are all linearly proportional to the activity concentration in the imaging subject, the randoms rate, due to its squared dependence on the singles rate, increases quadratically with activity. Therefore, at high activity, the randoms lead to substantially lower NECR as the they begin to dominate the overall counts. Methods to reduce randoms primarily rely on improving the timing performance of the PET system to reduce the coincidence time window (via faster decay of scintillation light and faster readout

electronics) and potentially use of time-of-flight measurements to reduce coincidence events.

The randoms rate can also be estimated and compensated for in the data, and the two most common methods are to use the singles rates (SR) or a delayed coincidence window (DCW) [47]. The SR method simply uses the singles rates per each detector pair to estimate the randoms rate as in Equation 2.5. The DCW method (which requires a k ¿ 1 in the NECR equation) duplicates the stream of singles events and delays events from one stream by a time greater than the timing resolution of the detector, recording any coincidences between events with their corresponding delayed copy event. Since there is no correlation between the detection of the original event and its delayed copy, detecting it as a coincidence makes it inherently a random. Several studies have compared these methods [13, 102], and while the DCW method is more accurate it retains several drawbacks, including implementation in hardware that introduces additional system deadtime and higher levels of statistical noise than the SR method, since SR relies on counting singles where DCW counts coincidences [13]. For this reason, research into alternative methods of randoms correction is ongoing [77], particularly with efforts to improve overall PET system sensitivity, which tend to increase the rate of randoms alongside the overall count rate.

2.3.3 Realistic PET System Model

Taking into account the factors affecting spatial resolution (PSF) along with the randoms and scatters, a more realistic model for coincidence events for a detector pair forming an LOR ℓ_{ij} is given by

$$y_{ij}^{[T]} = \epsilon_{ij}\mu_{ij} \int\int\int PSF_{ij}\left(\mathbf{r}\right) f^{[T]}\left(\mathbf{r}\right) d^3\mathbf{r} + E\left\{R_{ij}^{[T]}\right\} + E\left\{S_{ij}^{[T]}\right\} + \xi_{ij}^{[T]}, \tag{2.9}$$

where ϵ_{ij} is the sensitivity of the detector pair, μ_{ij} accounts for attenuation (assuming uniform attenuation), $E\left\{R_{ij}^{[T]}\right\}$ is the expected number of randoms, $E\left\{S_{ij}^{[T]}\right\}$ is the expected

number of scatters, and $\xi_{ij}^{[T]}$ is the Poisson distributed measurement noise as described in Section 2.1. If $\tilde{R}_{ij}^{[T]}$, $\tilde{S}_{ij}^{[T]}$, $\tilde{\mu}_{ij}$, and $\tilde{\epsilon}_{ij}$ are unbiased estimates of their corresponding parameters in Equation 2.8, then the corrected measurements can be written as

$$\tilde{g}_{ij}^{[T]} = \frac{\tilde{y_{ij}^{[T]}} - \tilde{R}_{ij}^{[T]} - \tilde{S}_{ij}^{[T]}}{\tilde{\epsilon}_{ij}\tilde{\mu}_{ij}} = \int\int\int PSF_{ij}\left(\mathbf{r}\right) f^{[T]}\left(\mathbf{r}\right) d^3 + \xi_{ij}^{\prime[T]}, \tag{2.10}$$

where $\xi_{ij}^{\prime[T]}$ is the noise after correcting the data. Versions of this model of the corrected data can be utilized for image reconstruction to be discussed in the next section.

2.4 Image Reconstruction in PET

Here we summarize the fundamental image reconstruction methods utilized for the standard cylindrical PET geometry. For further discussion, please refer to [30, 61, 65]. There are two standard formats for storing PET data. One is a histogram format where the number of coincidence events from every detector pair is stored together. The other is list mode format, where each event and its time, energy, and position information are stored individually in series. Generally scanners output list mode data which is subsequently rebinned into histogram format for reconstruction. However list mode methods for reconstruction also exist [8, 82, 97]. Historically, histogram mode reconstruction has been the standard practice for PET, despite the loss via binning of energy, timing, and crystal location data for the events. This has primarily been due to the computational complexity of implementing list mode algorithms for real systems, but research on practical list-mode reconstruction implementation is ongoing [19]. The computational methods used to perform image reconstruction on this type of PET data fall into two broad classifications: (1) analytic and (2) iterative methods. Each of these is described below.

2.4.1 Analytic Reconstruction

The filtered back-projection (FBP) algorithm is the fundamental analytic method used for tomographic image reconstruction. It is the solution for computed tomography first derived by Bracewell [12] to the more generalized inversion problem formulated by Johann Radon in 1917 [87]. FBP is based on an idealized representation of the imaging problem as in Equation 2.4, where the data collected along each line of response ℓ_{ij} represents a line integral of the source activity along the LOR and does not account for spatially variant system responses.

In the simplest case of trying to reconstruct a two-dimensional PET image from this data, it is useful to specify an LOR, ℓ by two parameters ϕ and ρ. If we define a line perpendicular to the LOR, $\ell_\perp$, going through the origin and pointing along the unit vector $\mathbf{s}_\phi$ defined by $[cos\phi, sin\phi]$. Then ϕ is the inclination angle of the LOR ℓ, and ρ is the location on $\ell_\perp$ where it intercepts ℓ. We can define the unit vector $\mathbf{t}_\phi = [-sin\phi, cos\phi]$ which points along the LOR, and of course γ is the point along ℓ where the event occured. This allows us to parameterize our LOR as follows:

$$\ell\left(\phi,\rho\right) = \left\{\rho\mathbf{s}_\phi + \gamma\mathbf{t}_\phi : \gamma \in \Re\right\} \tag{2.11}$$

We can then rewrite Equation 2.4

$$y^{[T]}_{\ell(\phi,\rho)} = \mu_{\ell(\phi,\rho)} \left\{ \int f^{[T]}\left(\rho\mathbf{s}_\phi + \gamma\mathbf{t}_\phi\right) d\gamma \right\} + \xi^{[T]}_{\ell(\phi,\rho)}, \tag{2.12}$$

where $\mu_{\ell(\phi,\rho)}$ is more fully expressed as

$$\mu_\ell\left(\phi,\rho\right) = e^{-\int \mu(\rho\mathbf{s}_\phi + \gamma\mathbf{t}_\phi) d\gamma}. \tag{2.13}$$

Now if we assume the ideal case with little measurement noise in the data and accurately measured attenuation $\mu_{\ell(\phi,\rho)}$, we can express Equation 2.12 in terms of the attenuation-

corrected data $p^{[T]}_{\ell(\phi,\rho)} = y^{[T]}_{\ell(\phi,\rho)}/\mu_{\ell(\phi,\rho)}$ so that

$$p^{[T]}_{\ell(\phi,\rho)} = \int f^{[T]}\left(\rho\mathbf{s}_\phi + \gamma\mathbf{t}_\phi\right) d\gamma \tag{2.14}$$

which is a 2D function generally referred to as the projection of the imaged object $f^{[T]}(\mathbf{r})$. In PET, the standard FBP algorithm is based on a parallel-beam geometry and utilizes the Fourier slice theorem, which relates the 1D Fourier transform of the projection $p^{[T]}(\phi,\rho)$ with respect to ρ to a slice of the 2D Fourier transform of the image $F^{[T]}(u,v)$ at angle ϕ from the u-axis. We can write this as

$$p^{[T]}(\phi,\omega) = F\left(\omega cos\phi, \omega sin\phi\right), \tag{2.15}$$

$$p^{[T]}(\phi,\omega) = \int_{-\infty}^{\infty} p^{[T]}(\phi,\rho)\, e^{-2\pi\rho\omega} d\rho, \tag{2.16}$$

$$F^{[T]}(u,v) = \int_{-\infty}^{\infty}\int_{-\infty}^{\infty} f^{[T]}(x,y)\, e^{-j2\pi(ux+vy)} dxdy, \tag{2.17}$$

where $u = \omega cos\phi$, and $v = \omega cos\phi$. By using the Fourier slice theorem, we then derive the FBP algorithm's expression for the imaged activity distribution at time T

$$f^{[T]}(x,y) = \int_0^{\pi}\int_{-\infty}^{\infty} p(\phi,\omega)\,|\omega| e^{j2\pi\omega\rho} d\omega d\phi, \tag{2.18}$$

where $\rho = x\cos\phi + y\sin\phi$.

For cylindrical scanners and when the data is binned into a parallel-beam histogram with some spacing between detector centers δd_c and a scanner radius R_s, then we can derive an expression for the spacing between LORs for each parallel beam projection

$$\delta\rho = \delta_c\sqrt{1 - \left(\frac{\rho}{R_s}\right)^2}. \tag{2.19}$$

Notably this spacing is non-uniform with different values of ρ, requiring radial interpolation between samples such that they are uniform. To implement the FBP algorithm, one takes the histogram data after this sampling correction and performs a convolution between it with the ramp filter $|\omega|$. By adding this convolved data from different angles ϕ, one can reconstruct activity distribution $f^{[T]}(x, y)$. However, images resulting from this method suffer from poor resolution and overall image quality performance, which in part stems from the PSF in the PET data not being accounted for by FBP, the resampling mentioned above which is effectively a low-pass filter, and smoothing by the filter function (usually an apodizing window function is chosen to replace the ramp filter since the ramp filter results in amplifying high frequency noise). For these reasons, we now turn our attention to iterative reconstruction techniques which more easily account for the physical and statistical properties of the PET imaging process.

2.4.2 Iterative Reconstruction

Iterative reconstruction algorithms pose the image generation problem as an optimization of an objective function. This objective function is premised on a statistical model of the PET data, which can incorporate elements of the detection process described in Equation 2.10. The iterative formulation of this problem is

$$\tilde{\mathbf{g}}^{[T]} = H\mathbf{f}^{[T]} + \xi'^{[T]}, \tag{2.20}$$

where $\tilde{\mathbf{g}}^{[T]}$, $\mathbf{f}^{[T]}$, and $\xi'^{[T]}$ are vector representations of the corrected PET data, the radioactive source distribution, and the noise, respectively. H is the projection matrix which accounts for the event detection processes that convert the source distribution into the measured PET data space.

The problem posed in Equation 2.20 is part of a larger class of inverse problems that is

broad research area on its own [95, 11, 9]. Formulations of the problem can be deterministic, which lead to the traditional maximum-likelihood (ML) approach, or random, which result in a maximum *a posteriori* (MAP) approach [78]. To begin, we return to the ideal Poisson model of the data $\tilde{\mathbf{g}}$ and for a moment ignore the other physical factors involved in detection as well as the time component $[T]$. In this case we can write the log likelihood function of $L(\mathbf{f})$, which is the Poisson probability density function of our model, as

$$l(\mathbf{f}) = \log L(\mathbf{f}) = \sum_{i=1}^{M} \left\{ \tilde{g}_i \log \left(\sum_{j=1}^{N} H_{ij} f_j \right) - \sum_{j=1}^{N} H_{ij} f_j \right\} + constant, \tag{2.21}$$

where M is the number of detector pairs in the system, and N is the number of pixels/voxels in the image. To find an ML estimate of $\mathbf{f}$, we must maximize the likelihood (or log-likelihood), and so we get an estimator of the form

$$\hat{\mathbf{f}}_{\mathrm{ML}} = \underset{\mathbf{f} \in \Omega}{\operatorname{argmax}}\, l(\mathbf{f}), \tag{2.22}$$

where Ω is the parameter space on which $\mathbf{f}$ is defined. In the case of both MAP estimation and penalized ML (PML), the estimator becomes

$$\hat{\mathbf{f}}_{\mathrm{MAP/PML}} = \underset{\mathbf{f} \in \Omega}{\operatorname{argmax}} \left[l(\mathbf{f}) + \log P(\mathbf{f}) \right], \tag{2.23}$$

where $P(\mathbf{f})$ is either a prior in the case of MAP or a penalty term in the case of PML.

PET reconstruction as in inverse problem is ill-posed (noise in the data is a significant barrier to accurate solutions), and so iterative reconstruction algorithms use a method for regularization to suppress noise [36, 56, 60, 107, 109]. With this in mind, we quickly see that most iterative methods in PET vary largely to the extent that they employ different methods for regularization, though differences in computational implementation and convergence speed are also significant factors. We now review several of the more common algorithms

used for PET reconstruction.

An ML estimate can be obtained by using the expectation maximization (EM) algorithm, a method originally proposed by Dempster *et al.* [32] and applied to emission tomography by Shepp and Vardi [99] and Lange and Carson [66]. The algorithm steps back and forth between computing the mean of the so-called "complete data" given the observed data and a current estimate of $\mathbf{f}$, or estimate $\mathbf{f}^n$, and then maximizing the probability of the "complete data" over the image space. This can be combined into a single update step, which, for a voxel j of the image estimate $\hat{f}^{(n)}$ for a current estimate n, can be written as

$$\hat{f}_j^{(n+1)} = \frac{\hat{f}_j^{(n)}}{\sum_i^M H_{ij}} \sum_i^M \left\{ H_{ij} \frac{\tilde{g}_i}{\sum_k^N H_{ik} \hat{f}_k^{(n)}} \right\}. \tag{2.24}$$

This MLEM algorithm has several attractive aspects with regard to PET reconstruction. Due to the update step being multiplicative, if one starts with a non-negative initial estimate, it carries a built-in guarantee of non-negativity with each update. It will converge to a local (if not global) ML solution, is straightforward to implement, and yields satisfactory image quality, particularly in comparison to FBP [16, 43, 69, 118].

However, MLEM has several limitations. One is its slow convergence rate, which has been one of the central challenges with its implementation in commercial systems. For this reason, Hudson and Larkin proposed the ordered subsets MLEM (or OSEM) algorithm [49], which accelerates convergence of MLEM by breaking the data into subsets and using the subset of the data during the update step. One pass through all the subsets is considered a full iteration, and convergence acceleration depends on how one chooses the subsets but can reach a factor up to the number of subsets. The subset update step can be written as

$$\hat{f}_j^{(n,\beta+1)} = \frac{\hat{f}_j^{(n,\beta)}}{\sum_{i \in S_\beta} H_{ij}} \sum_{i \in S_\beta} \left\{ H_{ij} \frac{\tilde{g}_i}{\sum_k^N H_{ik} \hat{f}_k^{(n,\beta)}} \right\} \quad \text{for } \beta = 0, 1, 2, 3, ..., B-1 \tag{2.25}$$

where a full iteration $\hat{f}_j^{(n+1)} = \hat{f}_j^{(n,B)}$ and S_β is the β-th subset. The OSEM algorithm and its variants are closely related to the general class of incremental gradient methods in which the objective function is broken into a sum of terms, and the update step for each iteration only uses the gradient with respect to one term [9]. While OSEM tends not to converge, it can be altered to include a relaxation parameter in the update step which has been shown to lead to convergence [3].

Another shortcoming of MLEM is that despite being quantitatively more accurate, the converged MLEM image is very noisy without regularization. However, one straightforward method to limit the noise is to stop MLEM before convergence, and while images qualitatively improve using this method, deciding a non-arbitrary stopping criterion can be challenging though quantitative methods have been proposed [114, 42]. Alternatively, regularization penalties can be applied to the data to reduce noise, but these often make the maximization step difficult [35]. Additional EM methods have been proposed to improve convergence and the ease of use for regularizing penalties, for instance Fessler and Hero's space-alternating generalized EM (SAGE) algorithm [34].

Moving from 2D to 3D iterative reconstruction methods, the algorithms are similar to 2D, but the computational cost becomes substantially greater. This is largely a function of accounting for the much greater number of voxels and lines of response (LORs) required for each projection to and from the image space. Put another way, the system matrix H_{ij} in Equation 2.20 becomes substantially larger for the 3D case as it takes into account the axial coordinates. However it is thought that the data redundancy in 3D increases the speed of convergence compared to 2D [111]. Methods for addressing the slow speed of 3D iterative algorithms like 3D-MLEM include using ordered subsets, parallelizing the computations (i.e. through CPU multithreading or use of GPUs), and reducing the size of the system matrix by exploiting sparsity and symmetries [30]. Another impediment to the wide adoption of 3D algorithms involves the fact that 3D data, due to its increased sensitivity to scatter and

randoms, requires methods to suppress noise from these types of events in the data. Advances on these fronts have led to 3D iterative algorithms being packaged with most commercial systems, an example of which is the GE's Q.Clear, a fully 3D Bayesian penalized likelihood algorithm [94].

2.5 Towards Improved Spatial Resolution PET Systems

While detector technology and image reconstruction methods have substantially improved PET image quality in the last several decades, PET spatial resolution performance still has significant room for improvement if we are to realize PET's potential impact on clinical care in the era of molecular imaging and personalized, targeted medicine. Here we review the spatial resolution performance of current clinical PET systems, application specific PET systems, and proposed detector insert systems.

2.5.1 Current Clinical PET Performance

As discussed in Section 2.3, to improve spatial resolution performance clinical PET systems, we must overcome substantial barriers related to the physical processes involved in event detection, including positron range, photon acollinearity, sampling errors, depth-of-interaction (DOI) blurring, errors in event location decoding, and blur due to detector size. Of these, the latter three effects are directly related to specific choices in detector module design and overall system geometry. A summary of resolution performance following the NEMA NU-2 protocol [6] for current commercially available scanners can be found in Table 2.3, which shows resolution performance in the range of 4-6 mm within the central 20 cm transaxial FOV.

Clinical PET/CT scanners typically all have the same wide cylindrical geometry ($\sim$70 cm diameter axial FOV, though simultaneous PET/MR have slightly smaller ($\sim$60 cm diameter axial FOV) and relatively small axial FOV ($\sim$20-25 cm), which serve to limit the DOI

	GE Healthcare			Siemens Healthcare		Philips Healthcare	
Parameter	Discover MI PET/CT [48]	Signa PET/MR [39]	Discovery 690/710 PET/CT [10]	Biograph mCT Flow PET/CT [90]	Biograph mMR PET/MR [31]	Vereos Digital PET/CT [51]	Ingenuity TF 128 PET/CT [62]
Spatial Resolution FWHM							
Radial, 1cm	4.10	4.46	4.70*	4.33*	4.3*	4.01*	4.84*
Tangential, 1cm	4.19	4.08	4.70*	4.33*	4.3*	4.01*	4.84*
Axial, 1cm	4.48	5.35	4.74	4.25	4.3	4.14	4.73
Radial, 10cm	5.47	5.81	5.34	5.16	5.2	NA	5.25
Tangential, 10cm	4.49	4.44	4.79	4.72	4.8	NA	5.01
Axial, 10cm	6.01	6.75	5.55	5.85	6.6	NA	5.23
Radial, 20cm	7.53	8.42	NA	5.55	NA	5.82*	NA
Tangential, 20cm	4.90	5.27	NA	6.48	NA	5.82*	NA
Axial, 20cm	6.10	7.30	NA	7.80	NA	6.17	NA

Table 2.3: NEMA NU-2 spatial resolution performance for 7 commercially available PET systems (5 PET/CT and 2 PET/MR) from 3 different manufacturers [48]. *Only averaged radial/tangential resolution was reported.

contribution to transaxial and axial resolution, respectively. Positron range for ^{18}F, the most common PET radioisotope, is relatively minor. The primary factors limiting spatial resolution are generally the physical detector size (typically between 4-6 mm in width [31, 90, 39, 92]) and any failure to decode event location due to light-sharing if using a "block detector" design. Even with one-to-one coupling of scintillator to photodetector, the Philips

Vereos system does not achieve resolution better than 4.01 mm [51].

However, resolution beyond 4 mm is desirable for many of the growing applications of PET imaging in research and the clinic. This is particularly true in brain imaging, a growing field for PET with broad applications, including in neurodegenerative diseases like Alzheimer's disease and Parkinson's disease, cancer, psychiatry, and the basic science of brain function [45]. Higher spatial resolution performance is necessary for adequately visualizing the small structures of the brain and generating accurate quantitative analyses. Higher spatial resolution performance is also desirable for pediatric imaging, where the smaller size of anatomical structures become challenging. For instance, imaging of pulmonary lesions in pediatric patients using FDG-PET is problematic since they are typically only millimeters in size [58]. Other areas where higher spatial resolution is especially desirable include breast and prostate imaging, where spatial resolution and sensitivity issues make imaging using a standard clinical PET system challenging. For these, the goal is often to catch disease at an earlier stage, which necessitates the ability to detect smaller lesions. The desire for improved lesion detection in the prostate coincides with the development of a number of choline-based radiotracers already finding some clinical success [124, 83]. In the current paradigm of molecular imaging and targeting biological specificity any further applications of novel radiotracers, targeted to biological processes requiring improved spatial resolution.

Cost remains a significant limitation in improving the image quality of clinical PET systems, which are priced on the order of several million US dollars [23]. For spatial resolution performance, designing systems with smaller photodetectors to afford one-to-one coupling with 4-6 mm scintillator elements they currently use, not to mention decreasing the scintillator crystal size to 2-3 mm, would add to this price. Decreasing the detector element size would also increase the total number of electronic channels required for detector readout, potentially requiring more or more complicated electronics, leading to higher cost as well as higher power consumption requirements, possible heat generation concerns, and a chance

of increased malfunction. Overcoming these design concerns, which are quite important in practice, can be a type of cost as well.

At the same time that there is a desire for better spatial resolution, there is a push for systems with larger FOV to increase sensitivity and reduce the number of bed positions required for a whole-body patient scan to the point where only a single bed position would be needed for what has come to be known as total-body PET [23]. The two prototype EXPLORER total-body PET scanners under development at the University of California, Davis and the University of Pennsylvania are seeking to achieve a 40-fold increase in sensitivity [1]. This increase in sensitivity has multiple potential benefits. First, if we assume the same scanning protocols as currently in use, it would lead to an increase in signal-to-noise-ratio (SNR). Second, it could lead to reduced scan times to achieve the same SNR achieved by current scanning protocols. Third, the sensitivity could be used to reduce the amount of injected radiotracer, saving patient dose, which is an attractive benefit for imaging pediatric patients and other at risk populations. Finally, systems with longer FOV and higher sensitivity are capable of imaging a larger fraction of the patient at once, allowing dynamic imaging of the whole body.

Along with these benefits of added sensitivity and increasing the FOV, all of the design concerns and costs associated with increasing spatial resolution apply here, as the total number of detector elements increases, electronic readout becomes more complicated, heating becomes a concern, etc. The estimated cost of the total-body PET system is approximately $10 million [23], or 5-7 times the cost of a typical PET scanner. Altogether, given these two competing inclinations (desire for performance vs cost practicality) in PET design, incremental improvements in spatial resolution and other image quality metrics are to be expected for standard cylindrical PET system designs. For this reason, research into alternative solutions to achieve better spatial resolution are of interest.

2.5.2 Improving Resolution with Nontraditional PET Geometries

As a workaround to the issue of cost, several groups have proposed PET-insert high resolution detectors to augment existing clinical and preclinical systems. One proposal is a silicon magnifying glass concept comprised of an inner ring of high-resolution silicon detectors inside a more typical clinical resolution detector ring comprised of traditional BGO block detectors [25, 24, 104, 80, 81]. This system has the potential for $\sim$0.7 mm spatial resolution using events from the high resolution detector alone, or $\sim$1.5 mm spatial resolution when using a mixture of high and mixed resolution events [24]. Limitations include the large size of the outer ring, complexity of the electronics for reading out events from both detector rings, constraints on the FOV due to the inner detector ring (14.0 cm diameter limiting its use to preclinical imaging), and still potentially the cost of the silicon detector.

Alternatively, researchers have proposed single detector or partial ring insert systems [59, 63, 71, 78, 106, 119, 120, 86, 127, 53]. These systems also rely on a magnifying effect from the close proximity of the high resolution insert detectors, but have some adaptability in task-specific placement of the insert detector. While these proposals do address the need to restrain the cost of a high resolution system by keeping the insert size minimal, they still have issues of readout electronics complexity, in addition to adding new problems of determining the optimality and reproducibility of the insert detectors placement within the exterior detector ring and providing reconstruction tools for these patient-specific geometries, though an initial framework for dealing with reconstruction of these arbitrary geometries has been laid out [72].

CHAPTER 3

EVALUATION TOOLS FOR MIXED RESOLUTION SYSTEMS

To design a new PET system, whether it is novel in geometry, instrumentation, or application, is a challenging task given the practical constraints of time and cost that it requires to develop and build. While new ideas for PET systems are produced semi-regularly (often specific to disease-site or a therapeutic approach needing image guidance), these costs of system design potentially inhibit the evaluation, and even the proposal, of new schemes for PET imaging along with preventing unproductive concepts from being discounted more rapidly. Providing a framework for more easily prototyping new PET systems could enable more rapid implementation of higher performance PET systems for cutting edge clinical applications and of more affordable PET systems for regions where PET systems are unavailable due to cost.

For this dissertation work, in order to better understand the performance capabilities of a potential PET system using mixed resolution detectors proposed in Section 3.1, appropriate simulation, reconstruction, and evaluation, tools for the mixed resolution imaging case were needed. Previous groups have developed simulation and also analytic and iterative reconstruction methods that utilize mixed resolution data for nonstandard detector geometries as discussed in Section 2.5. Primarily these studies have examined high resolution insert detector modules inside a traditional cylindrical PET system with standard resolution capabilities.

The proposed system in this work differs from these previous studies since the different resolution detectors do not lie in a concentric arrangement and instead occupy different positions along the axial extent of the detector module. This introduces a question of how best to generate simulated data and images for evaluation while keeping in mind limiting costs in the design process to make the overall study of mixed resolution PET systems more feasible.

Therefore, we set out in this chapter to develop and validate our own set of tools for this task. First the motivation for mixed resolution systems is explored in more depth in Section 3.1. The systems to be evaluated and their implementation in simulation are described in Section 3.2. In Section 3.3, the iterative reconstruction framework for mixed resolution data is discussed, including the method for generating the system matrix. Because of the practical considerations with regard to computation time and the desire to develop tools applicable to mixed resolution system geometries even beyond those explored in the present work, the methods developed are designed for flexibility and speed. Section 3.4 demonstrates the capabilities of the simulation and reconstruction tools from the previous two sections in several example cases, validating our framework for studying mixed resolution systems.

3.1 Motivation for Novel Mixed Spatial Resolution Geometry

The high resolution detector insert examples in Section 2.5 mix different intrinsic resolution detectors. Doing so yields regions in the image with higher resolution performance, and these regions are localized based on specific imaging tasks. This idea of mixing resolution detectors skirts the problem of replacing an entire scanner's detectors with higher resolution detectors if high resolution is only needed for part of the imaging volume. In this case, the cost incurred building a system with high resolution performance everywhere in the FOV is, in a sense, wasted. While avoiding "wasted" resolution, the insert systems have the undesirable consequence of reducing the FOV. Also, it is not easy in practice to position the insert optimally and link the electronics to the larger standard geometry scanner.

In order to escape "wasting" high resolution performance without using a detector insert, Liu *et al.* [70] explored the possibility of taking a traditional cylindrical PET design scheme and replacing choice detectors modules with higher resolution versions in order to boost spatial resolution in regions of the FOV near any high resolution detector modules. Simulating several orientations of the high resolution modules, they demonstrated improved

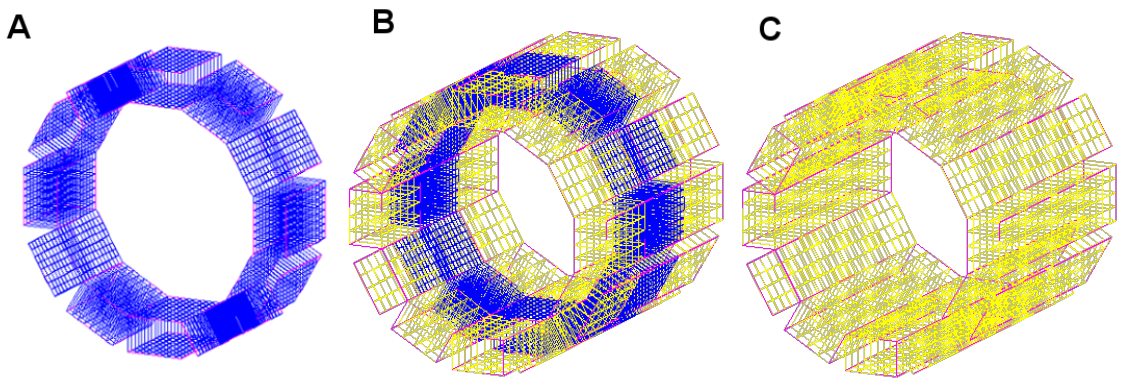

Figure 3.1: Example mixed resolution PET system concept (center), with a high resolution detector region (in blue) sandwiched between two standard resolution detector regions (in yellow) along the axial direction. For clarity, the high resolution module is shown (left) as well as a full standard resolution system (right), the center of which is replaced with the high resolution module in our mixed resolution concept. For this mixed resolution system, the ratio of high to standard resolution detector area is one-to-two.

resolution performance in regions of the FOV, but noted that the increased non-uniformity and anisotropy of resolution performance in a single slice might be be challenging to interpret without side-by-side images from the more uniform lower resolution system. However, a smaller increase in cost to build a system for a similar increase in resolution performance in a specific region of the FOV might be an acceptable trade-off.

In this work, we seek to extend the mixed resolution concept into a fully 3D framework where high resolution and standard resolution detectors occupy different neighboring rings along the axial direction of a scanner. This reduces the nonuniformity in any specific slice as compared to Liu *et al.* and puts the high resolution region at the center of the transverse FOV. This is as opposed to placing the high resolution region near the side of the scanner as in Liu *et al.*, which may require mechanically rotating the high resolution detector if it is not near the anatomical region of interest. An example of the concept is depicted in Figure 3.1, where the high resolution detector modules (made up of 12×8 arrays of 2×2×10 mm^3 crystal, shown in blue) are sandwiched between two standard resolution detector module regions (made up of 6×4 arrays of 4×4×10 mm^3 crystal, shown in in yellow) along the

axial direction. Each standard or high resolution section of the scanner is composed of 12 modules oriented in a ring, and the ratio of high resolution to standard resolution detectors is one-to-two.

A PET system of this type will collect three types of coincidence events: (1) coincidence events between two high resolution detectors, (2) coincidence events between a high and standard resolution detectors, and (3) coincidences between two standard resolution detectors. Previous groups have reconstructed this kind mixed resolution data using iterative methods to account for the different geometrical blur for each types of event in the system response matrix. It is expected that the overall sensitivity of our mixed resolution system concept will be better than the smaller subsystem of only high resolution modules and also that the mixed resolution system will have improved spatial resolution performance compared to a system of the same FOV but made from only standard resolution detectors.

The system configuration presented in Figure 3.1 is only one of many potential geometries combining high and standard resolution detectors. Another potential location for the high resolution detector region is at one end of the scanner, which may be advantageous for applications like brain or prostate imaging where high resolution is desired at one end of the patient but it is still desirable to image as much or all of the rest of the patient simultaneously. The scanner presented in Figure 3.1, on the other hand, might be more appropriate for imaging tasks where higher sensitivity is required for a region of interest within the high resolution subvolume of the scanner, since it is surrounded by the standard resolution detectors on either side. Other alternative designs include alternating rings of high and standard resolution detectors or partial rings of high resolution detectors sparsely incorporated throughout the axial FOV.

In this work, which seeks to establish the feasibility of this scanner concept to improve spatial resolution performance, we consider the centrally located high resolution region concept shown above as well as the end-located high resolution region design for evaluation due

to their. Both present a region of the scanner FOV contained by the high resolution detector modules where we should clearly expect improved performance if the concept is feasible, and both suit different imaging tasks as discussed above. Compared to the previous mixed resolution systems using inserts, these geometries do not present additional complications regarding detector insert placement or decreased transverse FOV. They extend the straightforward utility of existing cylindrical PET systems but maintain the potential to similarly improve spatial resolution performance in the high resolution subvolume. Moreover, because oblique LORS will be collected between the high and standard resolution detector modules, mixed resolution data will be collected for activity distributions underneath the standard resolution modules of the detector, indicating that these systems are likely to improve resolution performance in these areas of the FOV as well.

Though we are motivated by the clinical applications of increasing high resolution performance in clinical systems, in this work we study our mixed resolution concept by examining systems designed for small animal imaging. Such preclinical systems are where much of the prototyping work for high resolution detector research happens already, and developments from such systems are frequently scaled up to larger systems. A preclinical system then provides a good test base for evaluation of the basic feasibility of the concept, and it can be more readily translated into future work building an evaluation system and validating the results presented here with real data. The mixed resolution concept, if so validated, can then be translated to clinical systems as well.

3.2 Mixed Resolution System Implementation

3.2.1 Validation System

To validate the system design tools outlined above, we perform an initial study of a single mixed resolution system with a 4.8×4.8×7.2 cm^3 field of view (FOV). The scanner is a 12-

sided ring in shape and consists of three axial sections. The central 4.8×4.8×2.4 cm^3 of the FOV is surrounded by high resolution detector modules with individual 2×2×10 mm^3 LSO scintillation crystals coupled one-to-one to photodetectors in a 8×12 array with 2 mm pitch. On each end of the high resolution regions are 4.8×4.8×2.4 cm^3 regions enclosed by standard resolution detector modules consisting of individual 4×4×10 mm^3 LSO crystals coupled one-to-one to photodetectors in a 4×6 array with 4 mm pitch. Of note, one-to-one coupling is not necessary for systems to achieve 4 mm spatial resolution. In fact, clinical systems (as described in Section 2.5) achieve 4 mm resolution using block detectors that are less expensive. We assume one-to-one coupling in this work to simplify our simulations and because the dominating factor affecting spatial resolution is detector size and not the effects of block detector readout.

3.2.2 Simulation Methods

There are a variety of simulation tools incorporating Monte Carlo methods that are used to study PET systems, including Geant4 [2], EGS-PET [18], Penelope [98], MCNP [38], and SimSET [41]. Because of its standardized code base, flexibility in physics modeling, and ease-of-use, the Geant4 Application for Tomographic Emission (GATE) [52] is perhaps the most popular and well-validated open-source Monte Carlo software environment used in emission tomography research, and for this reason it is what has been utilized in this work.

The GATE environment allows the simulation of detector systems with detector elements of different sizes and orientations, as well as all physical materials and processes making up the imaging system. Each simulation is determined by a series of macro files that determine the detector geometry and materials, source and phantom geometry and materials, and physics processes, including attenuation and scattering in phantoms, interactions of the photons with the detector modules, and photons generated by bremsstrahlung and ^{176}Lu decay within LSO crystal elements. The data acquisition electronics characteristics like

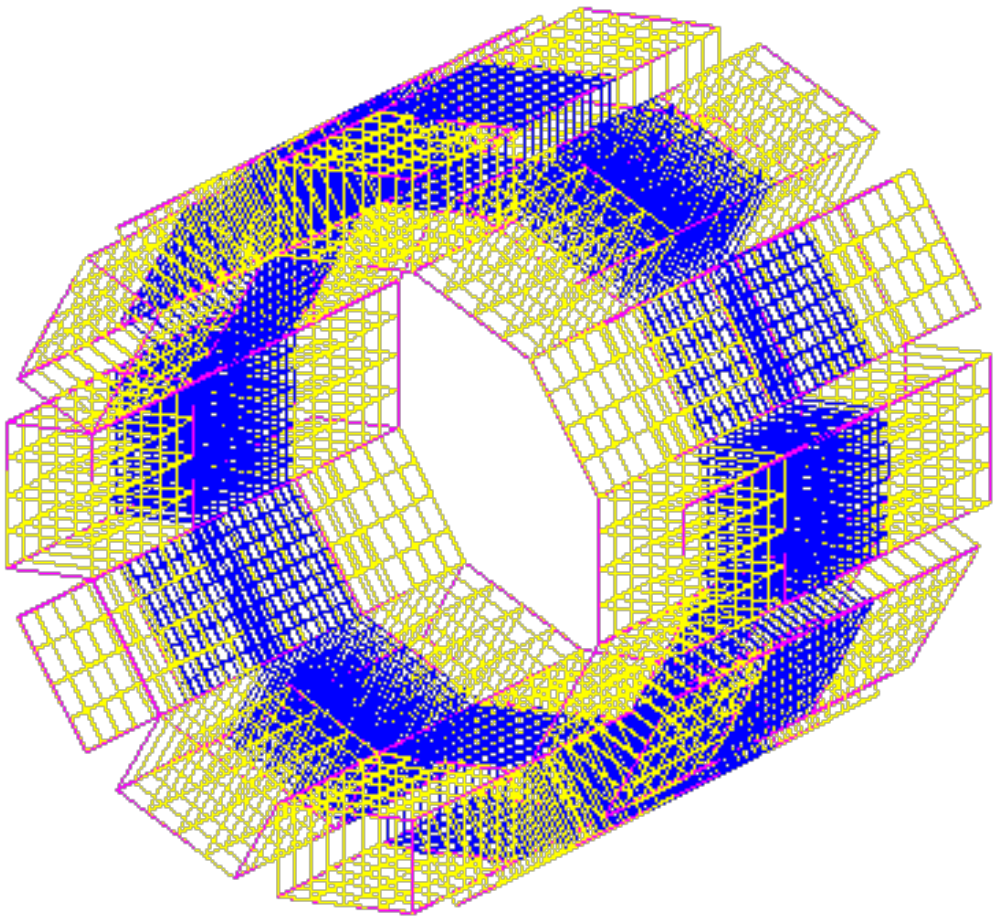

Figure 3.2: Simulated mixed spatial resolution PET system used for validation studies. The field of view is 4.8×4.8×7.2 cm^3. The high resolution detector modules (in blue) enclose the center 4.8×4.8×2.4 cm^3 region of the scanner, each in an array of 8×12 detector elements with 2 mm pitch. The standard resolution detectors (in yellow) enclose the 4.8×4.8×2.4 cm^3 region on each end of the detector head in an array of 4×6 detectors with 4 mm pitch. Crystals are 1 cm thick LSO. Photodetectors are assumed coupled one-to-one with scintillating crystal elements.

energy resolution, energy window, and coincidence window were also simulated. In this work, detections were stored as both singles and coincidence event-lists, and each event possessed an energy, time, detected position, and flags indicating if the event was scatter, bremsstrahlung or an ^{176}Lu decay. Coincidences were identified as true, scatter or random,

and also identified as associated with bremsstrahlung photons or Lu-176 decays. Time of flight (TOF) information was not recorded since TOF reconstruction methods are beyond the scope of this work. Moreover, TOF-capability for current state of the art detector technology is rarely useful for the small-animal imaging cases considered in this work since their TOF resolution is too poor. To reduce the simulation time, GATE version 7.1 and Geant4 version 10.01 were used since they contain straightforward tools for performing parallel computations on a computational research cluster. An example set of GATE macros can be found in Appendix A.

3.2.3 Sources and Phantoms

Numerical phantoms for use in validation of the system design tools and for determining image quality performance were implemented for use with GATE. Simple point, line, and cylinder sources were useful for validation of system design tools, basic measurements of system resolution, sensitivity, and uniformity. Several more complex phantoms were utilized for more involved assessments of image quality. This included a digital version of the contrast recovery region of the preclinical National Electrical Manufacturers Association (NEMA) phantom [76] in order to characterize resolution and noise performance.

3.3 Image Reconstruction Methods

3.3.1 Maximum-Likelihood Expectation-Maximization Algorithm

A maximum likelihood expectation maximization (MLEM)-based iterative reconstruction method was developed for the mixed resolution geometries considered in this work. MLEM is widely used in emission tomography, and it's convergence properties are well-established [32, 99, 66]. MLEM enjoys improved resolution and noise properties compared to forward backprojection (FBP), which is based on direct inversion of the Radon transform [88], be-

cause of MLEM's incorporation of the statistical nature of the data. However, iterative algorithms like MLEM are considerably more computationally intensive than single step algorithms like FBP.

An alternative reason for choosing an iterative reconstruction method like MLEM is that it can more readily incorporate the varying resolution and noise properties of the data compared to FBP. For the case where there are two types of detectors with different resolution properties, there are three different types of desirable coincidence events: (I) events where both annihilation photons are detected within a high resolution detector element, designated H for *High*, (II) events where one photon is detected in a high resolution detector element and the other is detected in a standard resolution detector element, designated M for *Mixed*, and (III) events where both photons are detected in a standard resolution detector element, designated S for *Standard*. Straightforward ways to combine these data for FBP to generate a single estimate of the image results in inadequate image quality [25]. An approach taken by previous groups [25, 78] has adapted the basic MLEM method described in Equations 2.21-2.23 and estimated the image using

$$\hat{\mathbf{f}} = \underset{\mathbf{f}}{\operatorname{argmax}} \left[\log P\left(g_H : \mathbf{f}\right) + \log P\left(g_M : \mathbf{f}\right) + \log P\left(g_S : \mathbf{f}\right) \right], \tag{3.1}$$

in which $\mathbf{f}$ is the image, and g_H, g_M, and g_S are the data corresponding to the coincidence types H, M, and S, respectively. The log likelihoods of the data can be added in this way since the data is independent. The update step to estimate the image f can then be written as

$$f_j^{n+1} = \frac{f_j^n}{\Sigma_k \Sigma_i h_{kij}} \left[\sum_k \sum_i h_{kij} \frac{g_{ki}}{\Sigma_j h_{kij} f_j^n} \right], \tag{3.2}$$

where j indexes image voxels, i indexes lines of response between detector pairs, k indexes the type of coincidence event (H, M, or S), h_{kji} is the system matrix, f_i^n is the image estimate at the nth iteration, and g_{ki} is the data.

Though we make use of the flexibility of MLEM reconstruction techniques, our method differs somewhat from this previous work, modeling resolution in the image domain rather than the projection space. This change is motivated by the difficulty involved in measuring or calculating elements of the system matrix in the projection domain as compared to the image domain, especially for longer bore scanners performing 3D image reconstruction. Such systems have a significantly larger number of lines of response relative to the number of voxels in the reconstructed images such that deriving, storing, and applying one or several corrections for each line of response can require substantial validation of each step and add more computation time during reconstruction. An image space solution is straightforward to apply, and its difficulty in implementation is primarily dependent on the size of the image space, which as noted is smaller than the projection space. This consideration applies to both small animal systems, which increasingly have a longer axial FOV and large numbers of high resolution detectors due to the desire to increase resolution and sensitivity. It also applies to proposed high sensitivity clinical systems like the Explorer total body PET system, which has an unprecedented number of lines of response for a PET system. Our image-space based approach is discussed in more detail in the following sections.

3.3.2 Ray Tracing Projection Method

Image reconstruction methods utilize a system response model h_{ij}, more generally known as a system matrix, in order to determine the contribution of each line of response i to a specific voxel j in the image. For a system matrix in a typical PET iterative image reconstruction context, each value in the system matrix can be related to the probability that a detected event coming from a specific voxel is measured by a specific pair of detectors. System matrices are computed analytically or via simulations. For analytical methods, these weights are often calculated using spatially variant solid angle computations [20, 75, 85] or via "ray-tracing" methods computing the intersection of lines of response (LORs) with pixels [100, 54, 99].

A method for flexibly describing the system matrix of the proposed mixed resolution geometry was developed by adapting the popular ray-tracing method of Siddon [100]. The Siddon method considers the image data as consisting of the intersection volumes of three orthogonal sets of equally spaced, parallel planes. Determining the intersections of a given ray with these planes is straightforward, and because the planes are equally spaced, after calculating the first intersection, the rest are generated by recursion. One can then use the intersections to calculate the path length of the ray in each voxel and therefore that voxel's contribution to the corresponding detectors when performing forward projection or the ray's contribution to the voxel value when performing back projection. Siddon's method is an approximation which can be further refined by additional corrections, for instance considering tubes of intersection with the voxel planes, but regardless the system matrix it calculates will not be completely accurate since it only approximates geometrical factors and does not otherwise model resolution effects. Resulting images will therefore incorporate distortions due to these effects. Despite its approximate nature, the Siddon's method is widely used because it is easy to implement and relatively fast to calculate on the fly.

System matrices for a variety of detector orientations and sizes can be modeled by simply changing parameters in the method accounting for the endpoints of the rays while the number and size of voxels in the image space can be changed by the number and pitch of the intersecting planes. This method was implemented for 3D reconstruction of our simulated mixed resolution scanner. For this purpose, a thread pool was created at the start of the reconstruction program. LORs were divided into groups and the ray-tracing operation for LORs in any given group were distributed to a single CPU thread as it became available such that all threads could be utilized simultaneously. Usually, CPU threads are dynamically created for specific tasks and closed when the tasks are finished. However, thread creation is itself an expensive process and with this dynamic allocation the computation time may in fact increase instead of decreasing as expected when using multiple threads. By creating a

thread pool at the beginning, we avoid this issue. In order to identify the optimal number of groups in which to divide the data to get the greatest potential speed-up, we examined how CPU time for forward and back projection changed when increasing the number of groups and varying the number of available threads (Figure 3.3). The speed-up in CPU time was observed to plateau after the number of LOR groups exceeded the number of available threads on the CPU. For the number of CPU threads available in the computers used in this work (typically 4-6), the speed-up observed varied between 2-3 times.

The algorithm was implemented in QT5 (The QT Company, Esproo, Finland) and Microsoft Visual C++ (Microsoft, Redmond, Washington). Separate classes were created for the projection, reconstruction, and threadpooling methods, as well as for each separate scanner utilized in this work. This allowed for easy application of our methods to multiple scanner configurations necessary for study in this work as well as scanners configurations that may be considered in future research.

We implement the multithreaded Siddon algorithm assuming PET systems consisting of detectors having the same resolution throughout their FOV. To accommodate the mixed resolution nature of the data, we calculated LORs for smaller uniform detector sizes. We upsampled the number of rays per line of response by a factor of 16 for high resolution LORs, by a factor of 48 for mixed resolution LORs, and by a factor of 256 for standard resolution LORs. We then recombined the calculated projections according to the actual resolution of the detectors.

3.3.3 Normalization Method

In PET, the detection efficiency for any given pair of detectors varies substantially across the entire system and depends on factors like the efficiency of the crystal material and the geometric efficiency of the crystal pair. It is necessary, especially to achieve quantitative results, to account for these non-uniformities by correcting the data. There are two primary

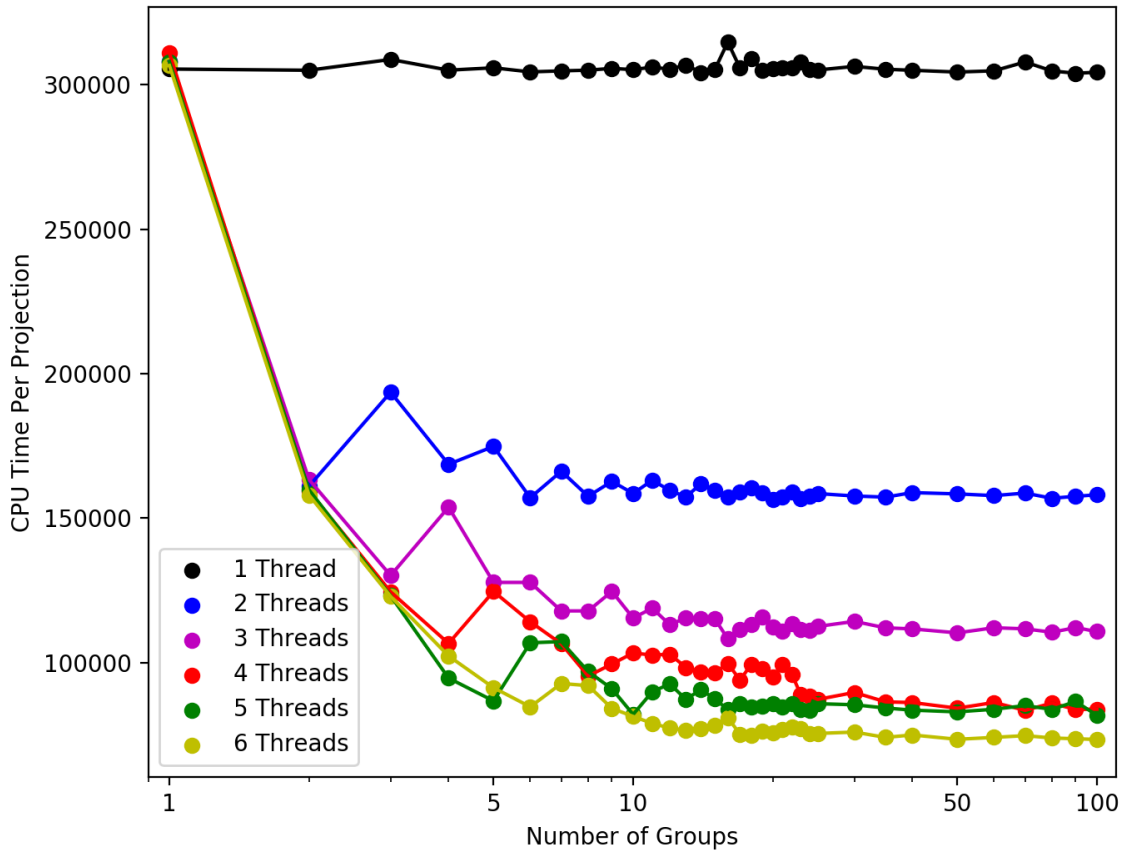

Figure 3.3: Required CPU time per forward projection versus the number of groups that projection data is split into for varying numbers of available CPU threads. The speed-up achieved by parallelization plateaus when the number of groups exceeds the number of available CPU threads. Back projection demonstrated the same trend.

ways to approach data correction. The first is the direct approach, which involves directly measuring the nonuniformities, and the second is the component-based approach, which involves modeling the different factors contributing to variation in efficiency. The direct approach can be challenging in physical systems since acquiring enough events for each detector pair to achieve statistical accuracy can be impractically time-consuming, especially since it can be limited by detector dead-time [108]. Moreover, error in the measurement process regarding source placement and distribution can contribute substantially to errors

in the resulting correction. However, because acquisition time (now computational time) and exact knowledge of the source distribution measured are not problems for these *in situ* studies, we adopted the direct approach. Normalization was necessary in our simulation studies since our Monte Carlo simulations included all the physics determining variations in crystal efficiency but our ray-tracing projection method assumes ideal detection efficiency. That is to say in our ray-tracing projection, detection probability is completely determined by a geometric proportionality to the detector area exposed to a given source pixel. In actuality (and in our simulations) the efficiency is also determined by the volume of of the detecting crystal that the LOR sees since that impacts whether an interaction will occur inside the crystal. In ray-tracing, these efficiency factors are all considered to be the same.

A voxelized cylindrical source with diameter equal to the transverse width of the image space (46.5 mm) and a length equal to the axial extent of the image space (69.5 mm) was generated. This voxelized source was forward projected using the ray-tracing algorithm to generate model data. It was also used as the basis of data simulated using GATE, from which 100 million coincidence events were collected. The data generated in GATE was taken as the "measured" data, since the simulation takes into account physical factors for which the ray-tracing forward projection did not. Differences aside from a scaling factor are considered to result from the physical factors to be corrected. To apply the correction operation e_i for LOR i, the data for each LOR to be reconstructed was multiplied by the corresponding ratio of the model data to the "measured" data from GATE. The corrected data was then used in the MLEM update step in reconstruction. The modified MLEM update step is

$$f_j^{n+1} = \frac{f_j^n}{\Sigma_i p_{ij}} \left[\sum_i p_{ij} \frac{e_i^{-1} g_i}{\Sigma_j p_{ij} f_j^n} \right], \tag{3.3}$$

where e_i^{-1} applies the normalization to data g_i.

3.3.4 Image Space Resolution Model

As previously discussed above, resolution effects in principle are best modeled in the system matrix so that they are subsequently removed from the resulting image. However, in practice this is difficult to achieve, and several groups have instead proposed to model the resolution effects in the image space using a stationary model of resolution, with successful results reported [91, 105]. These methods have several advantages, including straightforward implementation, faster computation time (because it operates in the smaller image space), and flexibility of the method with regard to forward and back projection. The parameters used in these models have been derived from analytical methods [96], experiment [79, 89, 91, 54], or Monte Carlo simulations [4, 84, 85].

In general, resolution modeling methods (in both the image and projection space) are associated with ringing artifacts that can appear near sharp intensity variations [101]. Inappropriate resolution kernels can generate these ringing artifacts [96]. Reader *et al.* [91] found that for image space resolution modeling, these artifacts were accentuated by over-modeling the resolution effects (using a resolution kernel that is too broad) but that they still appeared even when the resolution kernel was exactly matched to the data. Despite this potential for artifacts, the image-space resolution modeling remains a popular approach for the reasons mentioned above, and we therefore chose to adopt it in our development of the mixed resolution system.

$$\mathbf{g} = \mathbf{EHf} \approx \mathbf{EPf}, \tag{3.4}$$

In this approximate method, we assume that

$$\mathbf{g} = \mathbf{EPBf}, \tag{3.5}$$

where $\mathbf{P}$ is the ray-tracing-based projection matrix and $\mathbf{B}$ is a non-stationary blurring matrix.

We therefore assume the approximation $\mathbf{H} = \mathbf{PB}$, and the effects of the finite resolution of our system is modeled in the image space before projection. While $\mathbf{B}$ is chosen to be stationary in previous works using this method [91], it is also allowed to be non-stationary. In fact in our case, $\mathbf{B}$ must be non-stationary because we expect blurring to vary across the FOV, with different blurring in the volume encompassed by the high resolution detectors compared to the blurring in the volume encompassed in the standard resolution detectors.

Incorporating this model, our final MLEM update step, including normalization, becomes

$$f_j^{n+1} = \frac{f_j^n}{\Sigma_{j'} b_{jj'} \Sigma_i p_{ij'}} \left[\sum_{j'} b_{jj'} \sum_i p_{ij'} \frac{e_i^{-1} g_i}{\Sigma_j p_{ij} \Sigma_{j'} b_{jj'} f_{j'}^n} \right], \tag{3.6}$$

where $b_{jj'}$ applies the resolution model to the image data $f_{j'}$. The resolution model is applied twice per iteration, once prior to each forward projection and once following each back projection.

There are several approaches to implement $\mathbf{B}$, but generally they involve measuring (either with real or simulated data) the resolution for some set of point sources that are reconstructed using the chosen projection method $\mathbf{P}$ (in our case, Siddon's ray-tracing) and constructing $\mathbf{B}$ from the measured FWHM values. Reader *et al.* [91] proposes a shift-invariant approximation whereby the resolution throughout the FOV is modeled by a single resolution measurement. This approximation can be made more robust by measuring the reconstructed point response functions at other radial and axial positions to better model the resolution variance across the FOV.

In this work, we measured from reconstructed GATE point source data the point response function at the center of each transverse slice of the image domain along the axial FOV for each mixed resolution scanner studied in this work. For each measurement, simulated data with 1 million events were acquired. A 3-dimensional Gaussian function was fit to the point source to measure the FWHM, and the values are shown for each axial location in Figure

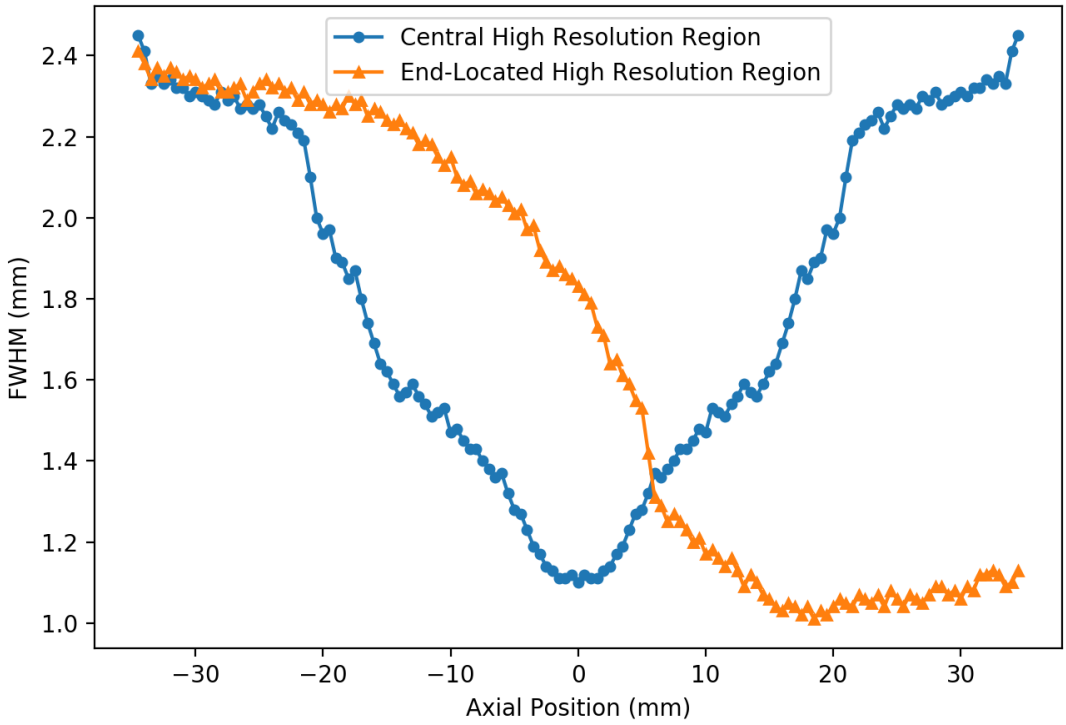

Figure 3.4: FWHM of 3D Gaussian function derived from Monte Carlo measurement and used in resolution module for each axial slice. Model is shown for a mixed resolution system with a centrally located high resolution region (studied in further depth in Chapter 4) and a system with a high resolution region located at one end (studied in further depth in Chapter 5).

3.4 for both the mixed resolution system with a high resolution region (studied further in Chapter 4) and the system with a high resolution region at one axial end of the scanner (studied further in Chapter 5). From these measurements and assuming a ground truth Gaussian point source distribution, we derived a slice-specific resolution model comprised of 3D Gaussian functions. Since the model uses measurements at the center of the FOV, it does not account for in-plane non-stationarity in the image. This non-stationarity will exist in our data due to depth-of-interaction (DOI) blurring effects that are included in our Monte Carlo simulations. We can therefore expect some DOI blurring effects in our reconstructed image.

3.4 Validation Studies

3.4.1 Reconstruction of Model Data

Studies to validate our simulation and reconstruction methods were first performed using data generated from our system model. From a truth image, the ray-tracing projector ($\mathbf{P}$) was applied to forward project the image. Data generated this way is henceforth referred to as *model data*. The model data was utilized to examine the algorithm's ability to exactly recover the truth image and ensure self-consistency. Model data was generated for a point source at the center of the FOV, for a point source at +24 mm in the axial direction, and for a phantom made up of four line sources extending through the entire axial FOV of the scanner. Each line source was square in shape with a width of 2.5 mm, and they were placed on the x or y axis centered a distance 12.5 mm from the CFOV. A 93×93×139 voxel grid with 0.5 mm^3 cubic voxels was used in reconstruction, and the MLEM algorithm using the ray-tracing system matrix ($\mathbf{H} = \mathbf{P}$) was run to 20 iterations. Example images for the point source at +24 mm and the four line source phantom at iterations 1, 5, and 20 are shown in Figure 3.5.

The normalized root mean square error (NRMSE) was calculated at each iteration between the reconstructed and truth images using

$$NRMSE = \sqrt{\frac{\Sigma_{j=1}^{N} \left(f_{True,j} - f_{Recon,j}\right)^2}{N}}, \tag{3.7}$$

where $f_{True,j}$ and $f_{Recon,j}$ are the jth voxel of the truth image and reconstructed image, respectively, and N is the total number of voxels. Images were normalized to their total intensity prior to NRMSE calculation.

NRMSE per iteration for the three sources are plotted in Figure 3.6. For the two point sources, the NRMSE approaches zero after only a few iterations, indicating fast and accurate

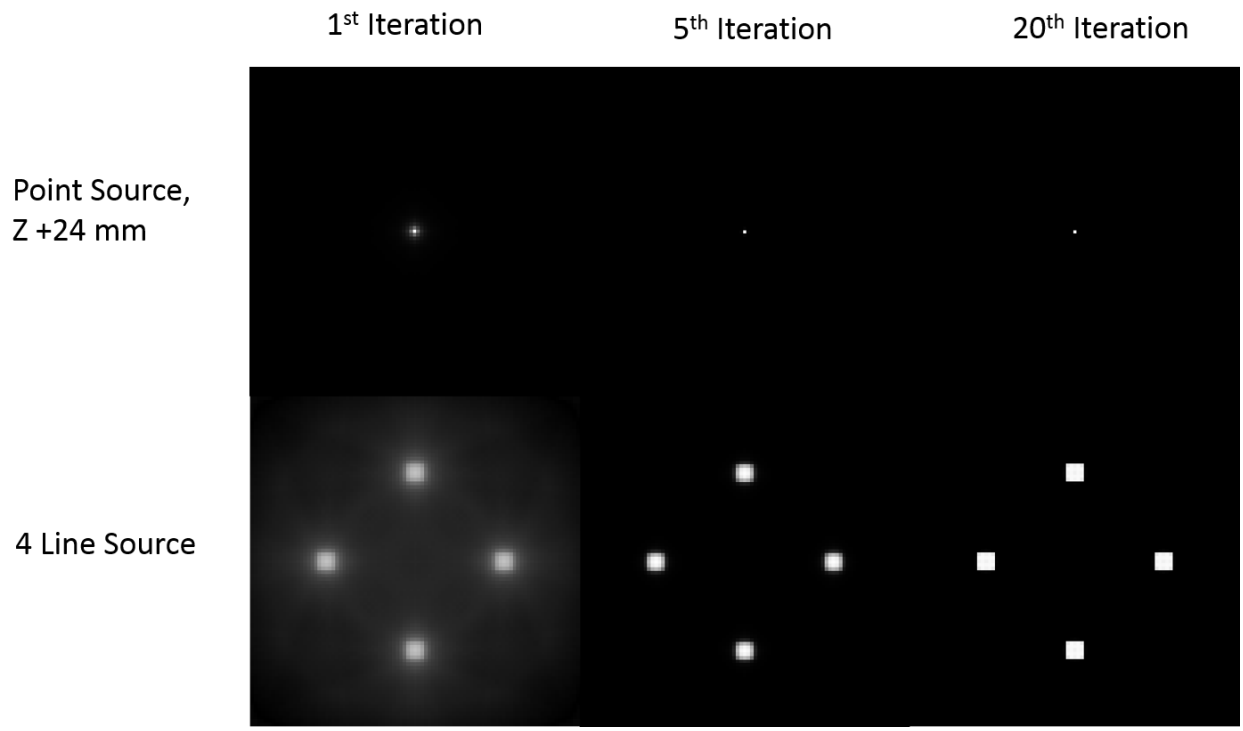

Figure 3.5: Axial slices reconstructed from model data for a point source at +24 mm in the axial direction and for a phantom comprised of four line sources for iterations 1, 5, and 20. The four line source is shown at the central slice.

recovery of the truth image. For the 4 line source image, since the truth distribution is more complicated, it is expected that the NRMSE would take more iterations to approach zero, and in fact it does, approaching zero at around the 20th iteration. These images and error calculations gave us confidence in our ray tracing model's self-consistency for use in further evaluating our algorithm on the data generated using Monte Carlo simulation in GATE.

3.4.2 Reconstructions of Monte Carlo Simulated Data

In order to better understand our algorithm's performance on data better resembling that acquired from a real PET scanner, we generated Monte Carlo simulations using GATE, which more accurately models the physical detection processes of PET. A voxelized source matching the truth image was implemented from interfile format images in all cases for precise comparison between the truth image and results generated from the model data.

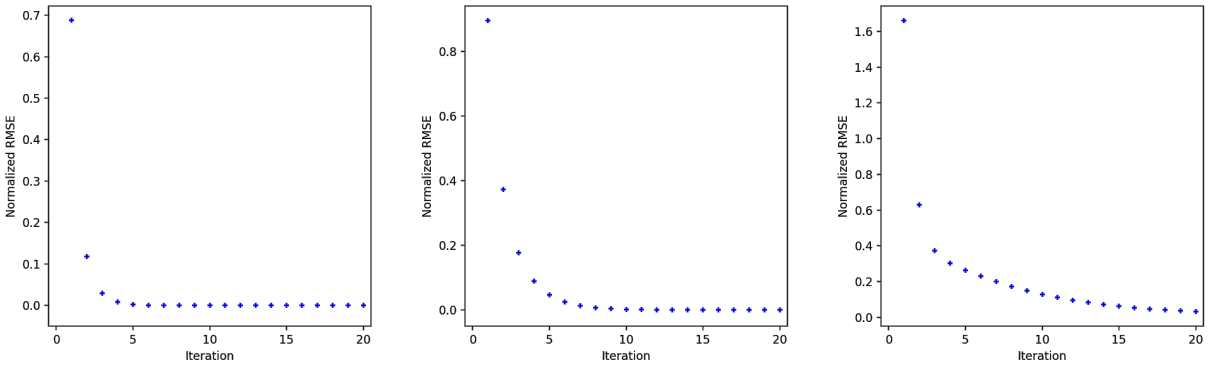

Figure 3.6: The NRMSE per iteration for a point source at center (left), at +24 mm in the axial direction (center) and for a phantom of 4 line sources extending throughout the axial FOV (right).

The validation PET system was implemented in GATE as described in Section 3.1. For the simulated digital readout from the detectors, the energy resolution was 15%, the energy window was 150-750 keV, and the coincidence window was 10 ns.

Singles and coincidence events were output from GATE in ROOT data format [14], and simulated coincidence events were converted from the GATE list mode format into a lexicographic histogram format for reconstruction. During conversion to the reconstruction format, scatter and random coincidences were removed using specific flags for these physical processes. A 93×93×139 voxel grid with 0.5 mm^3 cubic voxels was used in reconstruction. MLEM reconstructions of this Monte Carlo simulated data were performed using both ray-tracing projection alone ($\mathbf{H} = \mathbf{P}$) as well as ray-tracing incorporating the image space resolution model ($\mathbf{H} = \mathbf{PB}$).

By comparing these two methods, we sought to examine how the addition of the resolution model affected our reconstructed images. Initially we looked at a simple point source, implemented as a single voxel in the image domain (size 0.5×0.5×0.5 mm^3), at several locations: at the center of the field of view (CFOV), at CFOV plus 5 mm in the x-direction, at CFOV plus 5 mm in both the x- and y-directions, and at CFOV plus 24 mm in the z-direction. For the Monte Carlo simulated data in GATE, a 100 kBq point source was

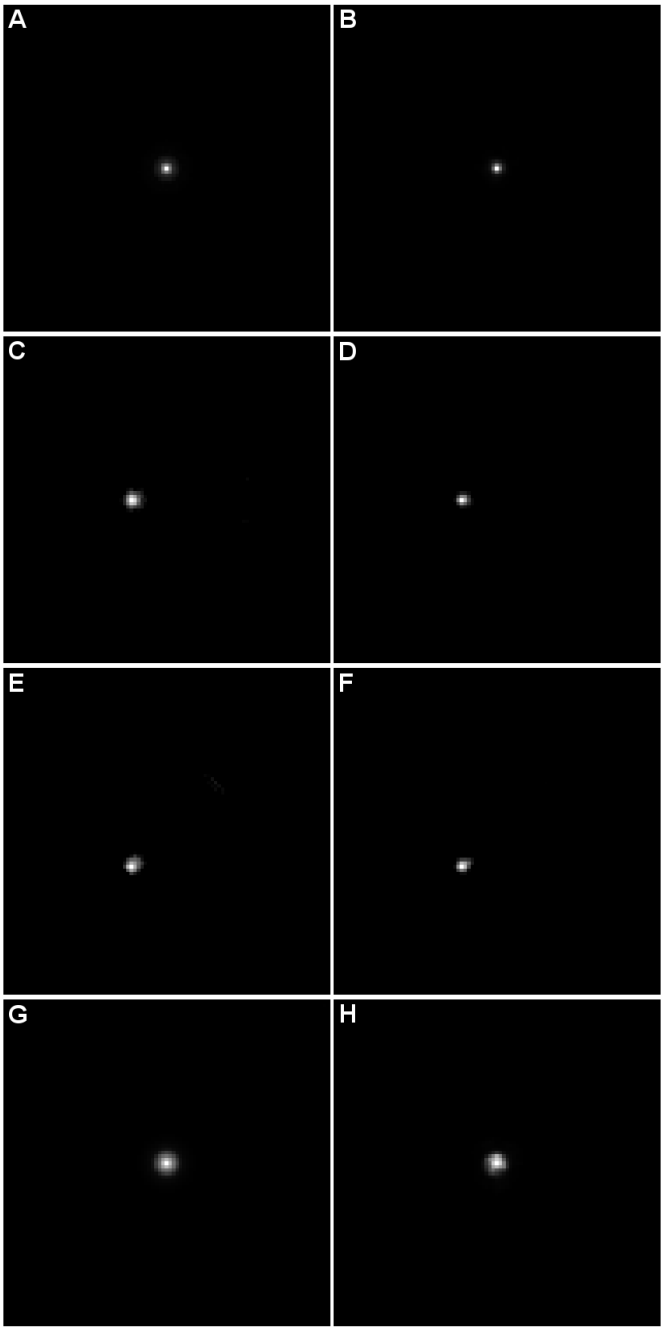

Figure 3.7: Reconstructions of point sources located at (A-B) center of the field of view (CFOV), (C-D) CFOV plus 5 mm in the x-direction, (E-F) CFOV plus 5 mm in the x- and y-directions, (G-H) CFOV plus 24 mm in the z-direction. The images in the left column (A, C, E, G) are reconstructed with the ray-tracing system model (**P**) alone while the reconstructed images in the right column (B, D, F, H) also incorporate normalization and the image space resolution model.

Spatial Resolution in FWHM (mm) for Different System Models at 4 Locations in FOV		
Resolution Direction, Source Location	Ray-Tracing	Resolution Model
X-Resolution, CFOV	1.00	0.89
Y-Resolution, CFOV	1.02	0.89
Z-Resolution, CFOV	1.26	0.75
X-Resolution, CFOV X+5mm	1.66	1.36
Y-Resolution, CFOV X+5mm	1.76	1.20
Z-Resolution, CFOV X+5mm	1.70	1.26
X-Resolution, CFOV X+5mm, Y+5mm	1.71	1.50
Y-Resolution, CFOV X+5mm, Y+5mm	1.75	1.40
Z-Resolution, CFOV X+5mm, Y+5mm	1.71	1.14
X-Resolution, CFOV Z+24mm	2.02	1.89
Y-Resolution, CFOV Z+24mm	2.01	1.95
Z-Resolution, CFOV Z+24mm	2.38	2.27

Table 3.1: Spatial resolution performance (in mm) for different system models used in reconstructions for point sources located at various locations in the field of view. Measurements at center, X+5mm, both X+5mm and Y+5mm, and Z+24mm using the ray tracing system model alone and also incorporating image space resolution modeling .

simulated at each location using the parameters and methods described above, and 1 million coincidence events were acquired. During reconstruction, projection data for a low-activity cylinder of known uniform background and equivalent in size to the normalization phantom was added to the simulated data. Following Qi *et al.* [85], this background was included in order to more accurately measure the resolution obtainable by MLEM reconstruction since the non-negativity constraint can otherwise lead to measuring an arbitrarily small resolu-

tion. Following Liu *et al.* [70] and Li *et al.* [68], we used a ratio of 200-to-1 between point source and background activity. Unless otherwise specified, the MLEM algorithm was run to 20 iterations, with each iteration taking approximately 26 minutes. Images for these point sources reconstructed with the ray tracing model ($\mathbf{H} = \mathbf{P}$) and with the system model incorporating the resolution model ($\mathbf{H} = \mathbf{PB}$) are shown in Figure 3.7.

We examined how spatial resolution performance changed after incorporating normalization and resolution modeling in reconstruction. The full width at half maximum (FWHM) was measured along the x, y, and z axes for all the point sources in Figure 3.7 and are compiled in Table 3.1. In all cases, modeling the additional sensitivity and resolution effects not incorporated in the ray-tracing algorithm alone resulted in improved spatial resolution performance.

The NRMSE for each iteration of the reconstructed point source images was calculated using Equation 3.7 and the values are shown in Figure 3.8. The ray-tracing only reconstructions have less initial error at earlier iteration, but the reconstructions utilizing the resolution model reach a lower NRMSE after 5-10 iterations. The difference between the NRMSE measurements appears to be more substantial for the three point sources located at the center slice (top left, bottom right, and bottom left in Figure 3.8) compared to the point source located at +24 mm in the axial direction (top right), an axial position underneath the standard resolution detectors of the mixed resolution system. This may imply that our resolution model provides less improvement farther from the axial center for the mixed resolution system used in these validation studies, which has a higher resolution detector region at its axial center. However, resolution performance still showed improvement with the resolution model for this location compared to without.

In order to validate our reconstruction algorithm's performance on a more extended object, the voxelized four line source used in the model data section above was simulated and used to study the error introduced in reconstruction. In brief, the source was made up

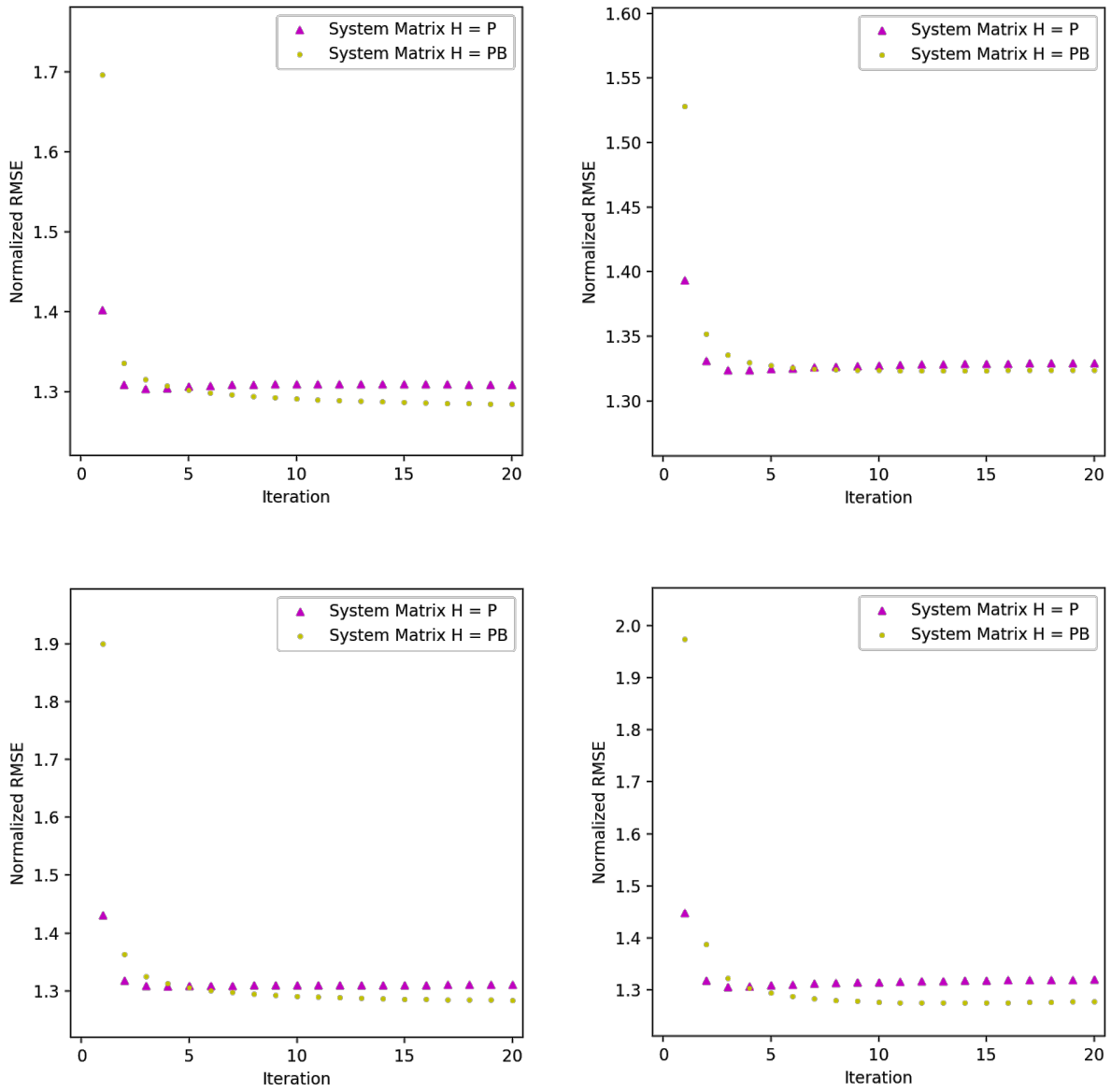

Figure 3.8: The NRMSE per iteration for a point source at center (top left), at +24 mm in the axial direction (top right), at +5 mm in the x-direction (bottom left), at +5 mm in the x- and y-directions (bottom right)

of four line sources in a diamond pattern extending axially throughout the entire FOV was also generated. One hundred million counts were acquired using GATE. Reconstructions utilizing system models with ray-tracing alone ($\mathbf{H} = \mathbf{P}$) and with ray-tracing and resolution modeling ($\mathbf{H} = \mathbf{PB}$) were performed. A central transverse slice and saggital slice through

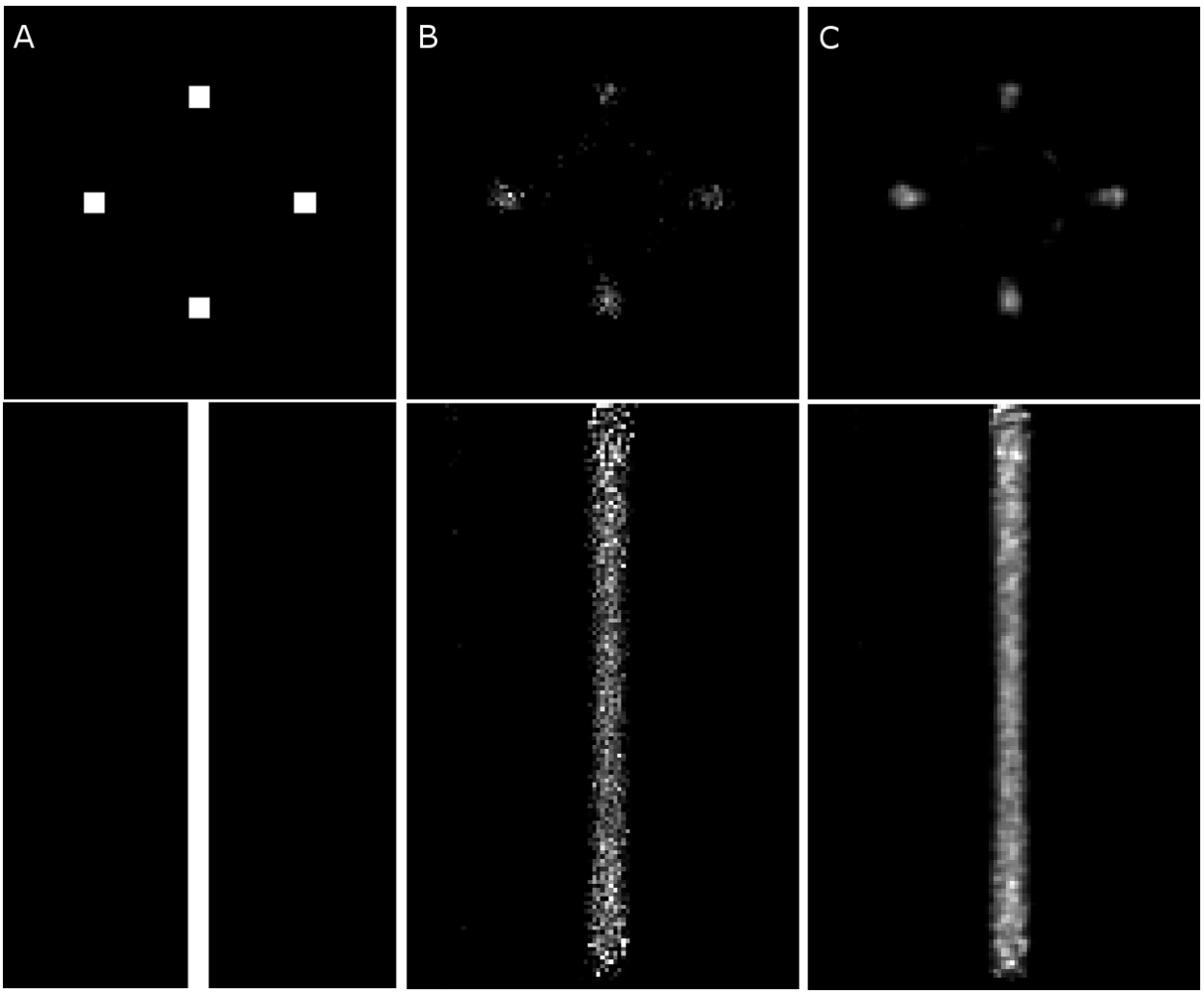

Figure 3.9: Reconstructed images of of a voxelized activity distribution comprised of 4 line sources simulated using Monte Carlo in GATE. Images were reconstructed applying system models using A) ray-tracing alone ($\mathbf{H} = \mathbf{P}$), B) ray-tracing ($\mathbf{H} = \mathbf{P}$) with normalization , and C) ray-tracing with normalization and resolution modeling ($\mathbf{H} = \mathbf{PB}$).

one of the line sources is shown for each reconstruction method in Figure 3.9.

We expect incorporation of the resolution model to lead to reduced noise and improved spatial resolution in resulting images, and qualitatively, the line source reconstruction incorporating normalization and the resolution model appears more uniform. Moreover, spatial resolution at the CFOV is improved, with 0.75 mm better tangential resolution compared to ray-tracing alone (3.28 mm FWHM for the ray-tracing system model and 2.53 mm FWHM for the system model incorporating normalization and resolution modeling). Whereas the

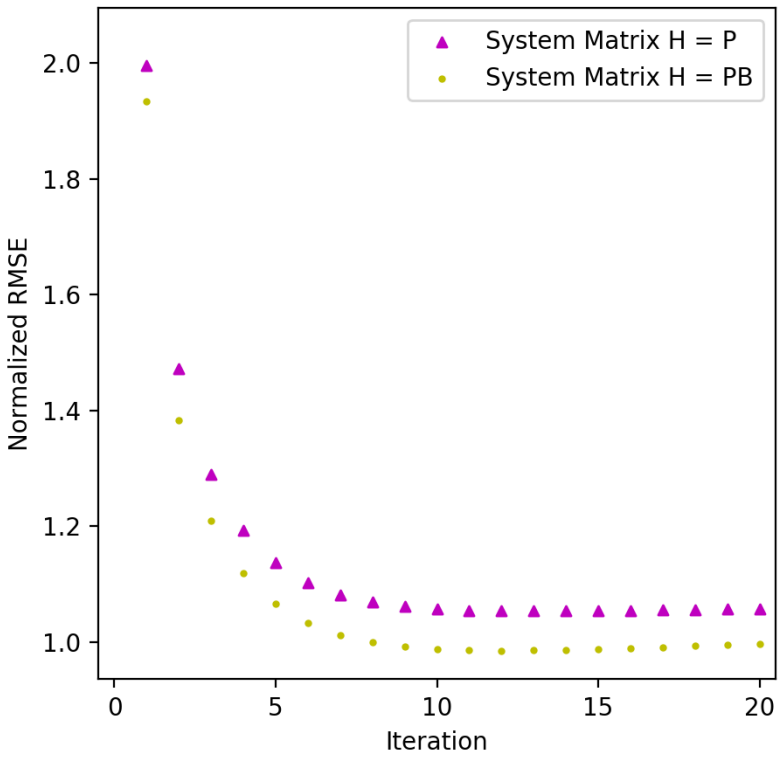

Figure 3.10: The NRMSE per iteration for a phantom comprised of 4 line sources in a diamond pattern and extending throughout the axial FOV.

spatial resolution performance at a slice 24 mm in the axial direction, where high resolution detector lines of response contribute little, is similar between the models (3.36 mm FWHM for the ray tracing system model and 3.31 mm FWHM for the system model incorporating normalization and resolution modeling). In the radial direction, depth-of-interaction (DOI) blurring is apparent in the image. The line sources appear more rectangular or oval than square, with the longer dimension in the radial direction. However, at the CFOV, the reconstruction incorporating the resolution model demonstrates better spatial resolution (4.18 mm FWHM) than the reconstruction with ray-tracing alone (4.57 mm FWHM).

The NRMSE of these reconstructions were calculated and are shown through 20 iterations in Figure 3.10. The reconstructions incorporating both the normalization and resolu-

tion model terms showed lower NRMSE compared to ray-tracing alone, demonstrating the resolution model's benefit in reducing error for larger extended sources.

Altogether, the reconstructions of Monte Carlo simulated data using the resolution model showed image quality improvement over the reconstructions using ray-tracing alone. Better resolution performance and recovery of the truth image as calculated by NRMSE were shown. We do note that the resolution model does not completely eliminate resolution non-uniformities that remain in some of the images, included DOI blurring and worse resolution performance away from the center of the axial FOV. With this understanding of the capabilities and limits of the algorithm, it can be used to examine the potential performance of mixed resolution systems and compare them to systems using detectors with a single characteristic resolution.

3.5 Summary

In this chapter, we have developed and validated tools to study the performance of mixed spatial resolution PET imaging systems. The performance of these initial simulations and reconstructions for an example system demonstrated the robustness of the system design tools for use in further evaluation of our design concept.

In the next chapters, we apply these methods to understand the image quality performance capability of several mixed resolution PET systems in terms of metrics of image quality, especially sensitivity and spatial resolution.

CHAPTER 4

EVALUATING PERFORMANCE OF MIXED RESOLUTION PET SYSTEM WITH CENTRAL HIGH RESOLUTION REGION

In the previous chapter, we validated our simulation and reconstruction methods used to study mixed resolution PET system designs. Simulation protocols were developed in the GATE Monte Carlo environment for a twelve-module ring-based system design incorporating high and standard resolution detectors. A 3D MLEM image reconstruction algorithm was devised based on Siddon's ray-tracing algorithm [100]. An image space resolution model was developed in order to better recover spatial resolution performance in the high resolution region of the PET system, and the algorithm was sped up using CPU multithreading.

A primary motivation for studying mixed resolution PET systems is incorporating higher resolution detectors in modern clinical PET systems. As described in Section 2.5, clinical PET systems' spatial resolution have seen only marginal improvements in the last decade, especially when compared to what has been shown to be technically possible in research systems. A major factor is overall system cost, which leads to limitations on the performance of a system's detector modules or alternatively limitations on the number of detector modules incorporated, sacrificing the scanner's field of view (FOV) and sensitivity. Moreover, high resolution performance is not generally necessary throughout the entire FOV, so building an entire scanner with high resolution detector modules can result in wasted resolution capability. We propose to solve this conundrum by boosting the spatial resolution performance in a sub-volume of the scanner, incorporating higher resolution detector modules around that region and retaining the standard resolution detectors in the rest of the scanner. This preserves the scanner's sensitivity and FOV while saving on the cost of high resolution detector modules.

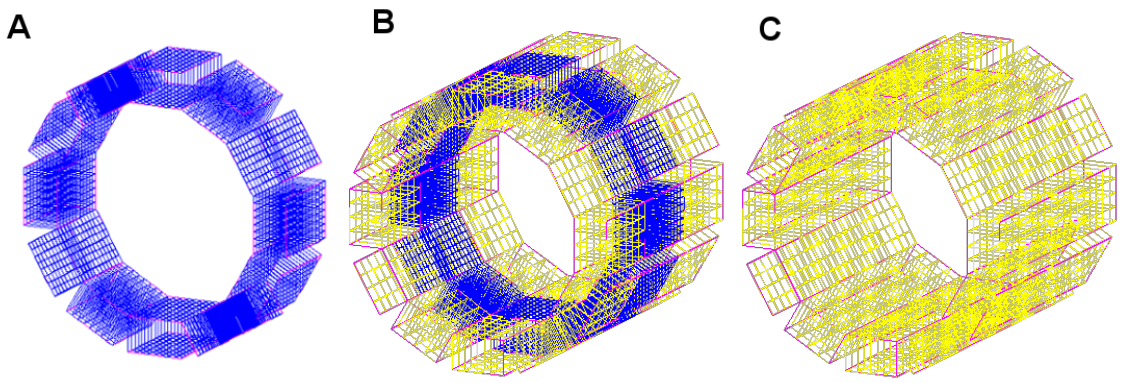

Figure 4.1: Visualizations of the three scanner configurations as simulated in GATE: A) the high resolution scanner, B) mixed resolution scanner, containing a central high resolution detector region (in blue) between two standard resolution detector regions (in yellow) , and C) the standard resolution scanner.

In this chapter, the system evaluation tools developed in Chapter 3 are used to study the performance of a mixed resolution PET system concept with a single central high resolution detector region. This location for the high resolution detectors means the regions of peak sensitivity and highest potential spatial resolution performance overlap at the center of the scanner. This configuration is compared to a scanner composed of just the high resolution region of detectors, in order to examine what is added by the increased sensitivity, and a scanner with the same overall dimensions as the mixed resolution scanner but composed of only standard resolution detectors, in order to examine the improvement in resolution performance. The design parameters of the scanners can be found in Table 4.1 and the scanner designs are shown in Figure 4.1.

In Section 4.1, we compare the sensitivity performance of the three PET systems. As expected, the longer FOV of the mixed and standard resolution scanners provide superior sensitivity throughout the equivalent FOV of the high resolution scanner. Spatial resolution performance is evaluated in Section 4.2 by adapting the NEMA NU 4-2008 protocol for pre-clinical PET scanners [76]. In Section 4.3, we compare the scanners' capabilities recovering regions of the NEMA image quality phantom given different noise conditions.

System Parameter	High Resolution	Mixed Resolution		Standard Resolution
		High Resolution Module	Standard Resolution Modules	
Ring Diameter (mm)	60	60	60	60
Crystal Pitch (mm)	2.0	2.0	4.0	4.0
Crystal Size (mm^3)	2×2×10	2×2×10	4×4×10	4×4×10
Detectors Per Module	8×12	8×12	4×6	4×18
Detectors Per Ring	96	96	48	48
Field of View (mm^3)	48×48×24	48×48×72		48×48×72

Table 4.1: Parameters describing the scanner configurations for the high, mixed and standard resolution systems studied in Chapter 4. Details for both the high and standard resolution regions of the mixed resolution scanner are provided.

4.1 Sensitivity Performance

As discussed in Section 2.2, the primary factors affecting overall system sensitivity are the size and material of the crystal scintillator used in the detectors as well as the detectors' solid angle coverage of the scanner's FOV. The mean distance traveled for a gamma ray in LSO, the scintillator material used in this research, is 11.6 mm, so crystals thicker than this are typically desirable. However, depth-of-interaction (DOI) effects can cause loss of resolution for thicker crystals. To avoid this effect, and the need for detectors with DOI measurement capabilities in preclinical imaging systems, crystals are typically 10 mm thick.

4.1.1 Methods

The axial sensitivity profile of the three proposed scanners were measured from GATE data by simulating a 100 kBq point source at the transverse center of the FOV and stepping it axially in 1 mm intervals through the FOV. Data was acquired for 100 seconds, and

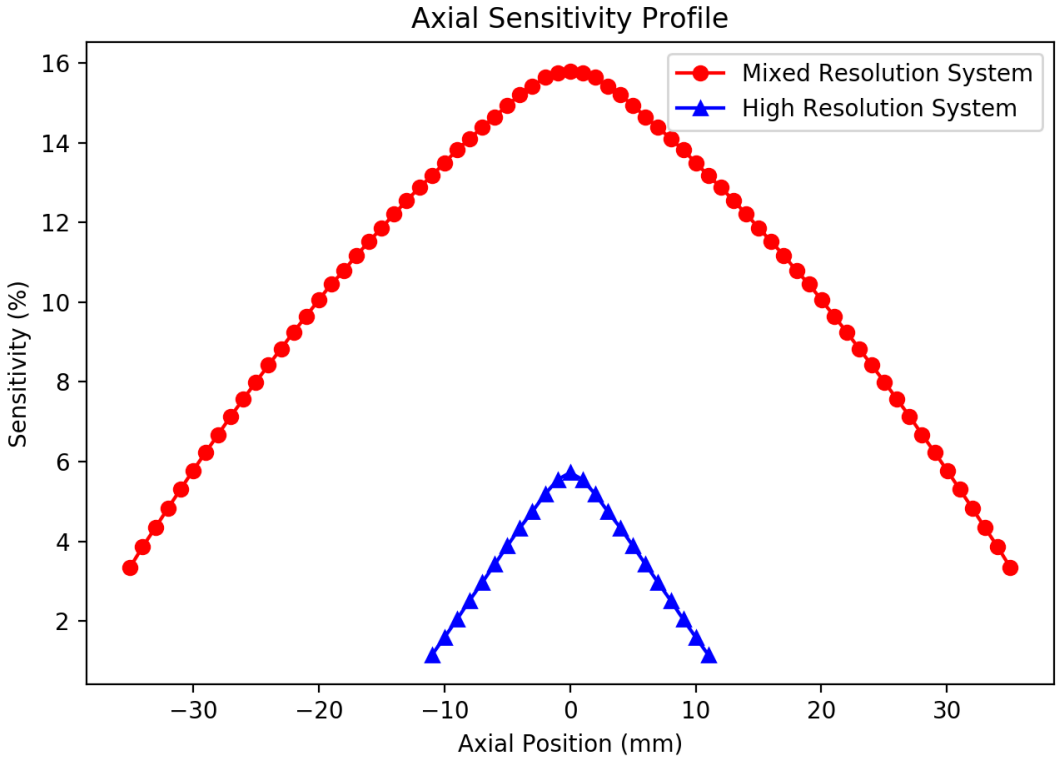

Figure 4.2: The axial sensitivity profile of mixed and high resolution scanners measured using GATE simulation of point sources stepped axially along the center of the scanner. The standard resolution system has equivalent sensitivity to the mixed resolution system and is therefore not shown.

the number of true coincidence events was recorded by removing scatter and randoms using specific event flags from GATE. The absolute sensitivity of the detectors for each point source location was recorded as a percentage of the total events emitted. Because the mixed and standard resolution scanners have exactly the same solid angle coverage, crystal thickness, and no gaps between crystals, it can be assumed their sensitivities are nearly identical, and only the mixed resolution case is reported.

4.1.2 Results and Discussion

The axial sensitivity profiles are shown in Figure 4.2. The peak sensitivity at the central slice for the mixed and standard resolution systems was 15.79% and 5.73% for the high resolution system. At the edge of the high resolution system's FOV, its sensitivity is just 1.15% (averaged from measurements at each end of the FOV) compared to 13.18% for the mixed and standard resolution systems at that axial location. The sensitivities of the longer systems only become lower than the high resolution peak sensitivity beyond 30 mm from the central slice. At the edge of the mixed and standard resolution system FOV, the sensitivity is 3.36%.

4.2 Spatial Resolution Performance

Spatial resolution performance is affected by a host of factors as described in Section 2.3, but it is frequently dominated by blurring due to the physical size of the detector elements. In our mixed resolution detector concept with a central high resolution region, activity in the region under the high resolution detectors provides event data to the reconstruction algorithm characterized by the high resolution detectors' size, but it also provides data characterized by standard resolution detectors as well as by data with mixed resolution performance. This intrinsically lower resolution data, when combined with the high resolution data during image reconstruction, are likely to result in degraded spatial resolution performance for the mixed resolution system compared to the high resolution alone system. To attempt to recover the high resolution information for the mixed resolution system, the reconstruction algorithm developed in Chapter 3 utilizes an image-space resolution model [91, 105] to account for variation in resolution performance throughout the FOV. Using our algorithm, we examined the feasibility of the mixed resolution system to achieve the resolution performance of the high resolution system.

4.2.1 Methods

For each scanner configuration, point sources with 100 kBq activity were simulated via Monte Carlo methods in GATE. Sources were placed on the central axial slice, at 1/4 the axial length of the high resolution detector (6 mm in the z-direction), and at 1/4 the axial length of the mixed and standard resolution scanners (18 mm in the z-direction). Four locations per slice were studied: at center and at 5, 10, and 15 mm in the positive x-direction. Data was acquired for 100 seconds and the first million events were extracted and converted to histogram format for reconstruction. Reconstructions were performed for 20 iterations on a 93×93×139 voxel grid for the mixed and standard resolution scanners and a 93×93×45 voxel grid for the high resolution scanner, with a 0.5×0.5×0.5 mm^3 voxel size. A low-activity cylinder of known uniform background and with diameter and length equal to the FOV was incorporated with the simulation. Following Qi *et al.* [85], this background was included in order to more accurately measure the resolution obtainable by MLEM reconstruction since the non-negativity constraint can otherwise lead to measuring an arbitrarily small resolution. Following Liu *et al.* [70] and Li *et al.* [68], we used a ratio of 200-to-1 between point source and background activity.

FWHM values were measured for each point source using the linear interpolation described in NEMA NU-4 2008 [76]. In brief, a line profile through the source location was collected in the radial, tangential, and axial directions, and the maximum values for each line were identified. The points along the line profile nearest the half-maximum value on each side of the peak were identified, and linear interpolation was used to calculate the locations of the half-maximums. The distance between these two points was the FWHM in that direction.

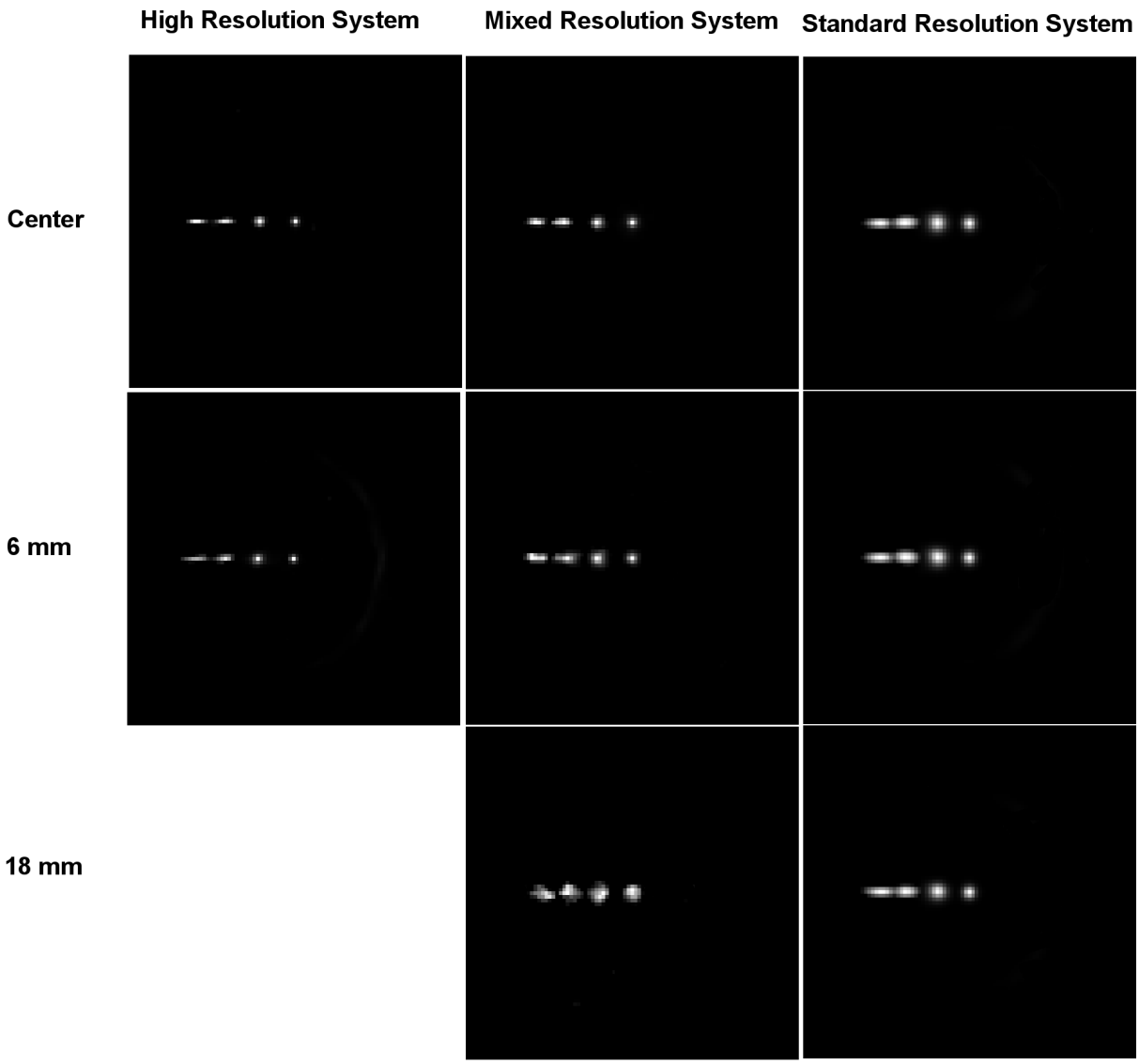

Figure 4.3: Overlayed transverse slice images of single point source reconstructions for point sources located at transverse center as well as 5, 10, and 15 mm from center. Three different axial locations (center and 6 mm from center for all three scanners and 18 mm from center for the mixed and standard resolution systems) are shown (arranged by row) for the different scanner configurations (arranged by column). The images demonstrate the radial and tangential resolution performance of the three scanner configurations. Each point source is shown in the image scaled to it's own maximum.

4.2.2 Results and Discussion

The FWHM values are reported for the three scanner configurations at the central slice in Table 4.2 and for the slice at 1/4 the high resolution scanner axial FOV (6 mm in the

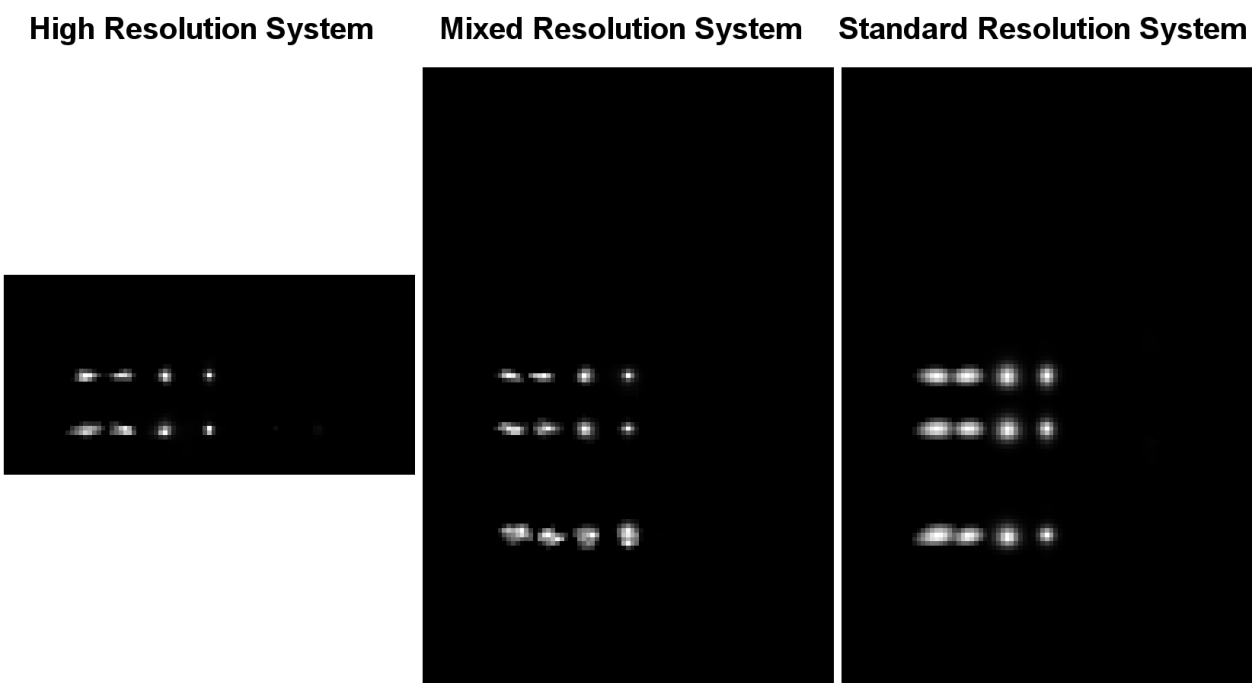

Figure 4.4: Overlayed coronal slice images of single point source reconstructions for point sources located at transverse center as well as 5, 10, and 15 mm from center. Three different axial locations (center as well as 6 and 18 mm from center) are shown (stratified vertically in each coronal image) for all three scanner configurations (arranged by column). Each point source is shown in the image scaled to it's own maximum.

z-direction) in Table 4.3. The FWHM values for the mixed and standard resolution at 1/4 their axial FOV (18 mm in the z-direction) are reported in Table 4.4. Transverse and coronal images showing the point source reconstructions for the high, mixed and standard resolution scanners can be found in Figures 4.3 and 4.4, , respectively.

The mixed resolution FWHM measurements for point sources lying within the high resolution region generally show improved spatial resolution performance compared to the standard resolution case, with FWHM values sometimes approaching the high resolution case. This trend is apparent in Figure 4.5, which shows how radial, tangential, and axial resolution changes with distance from the center of the FOV. For all three scanner configurations, there is clear evidence of radial resolution elongation due to depth-of-interaction blurring effect for point sources at 10 and 15 mm from the center of the transverse FOV.

Spatial Resolution in FWHM (mm), Center of Axial FOV			
Source Location	High Resolution	Mixed Resolution	Standard Resolution
Radial, center	0.71	0.90	1.43
Tangential, center	0.69	0.88	1.42
Axial, center	0.71	0.75	1.64
Radial, 5mm	1.06	1.36	1.76
Tangential, 5mm	1.01	1.20	1.76
Axial, 5mm	1.11	1.26	1.84
Radial, 10mm	2.68	3.10	3.64
Tangential, 10mm	0.81	1.31	1.65
Axial, 10mm	1.15	1.07	1.83
Radial, 15mm	4.12	2.29	3.73
Tangential, 15mm	0.73	1.07	1.55
Axial, 15mm	1.41	0.98	2.11

Table 4.2: Spatial resolution performance (in mm) at the center slice for the high, mixed, and standard resolution systems. Measurements at center and at 5, 10, and 15 from the center voxel are derived from MLEM reconstructions (see Section 3.2) of Monte Carlo simulations conducted in GATE.

For the mixed resolution case, the reconstructions of point sources farther from the center of the scanner, whether at 15 mm in the transverse plane or 18 mm in the axial direction, demonstrate irregular shape compared to the generally elliptical pattern demonstrated by both the high and standard resolution scanners that do not use mixed resolution data. This may be the result of imprecision in the resolution model used for reconstruction in these studies. In their discussion of image-space resolution models, Reader *et al.* [91] note that

Spatial Resolution in FWHM (mm), 1/4 of Axial FOV of High Resolution System			
Parameter	High Resolution	Mixed Resolution	Standard Resolution
Radial, center	0.68	1.07	1.39
Tangential, center	0.67	1.04	1.40
Axial, center	0.93	0.83	1.56
Radial, 5mm	0.99	1.39	1.88
Tangential, 5mm	0.99	1.29	1.73
Axial, 5mm	0.88	1.37	1.86
Radial, 10mm	2.28	2.60	3.58
Tangential, 10mm	0.91	0.99	1.80
Axial, 10mm	1.07	0.87	1.89
Radial, 15mm	3.34	3.17	4.06
Tangential, 15mm	0.86	1.24	1.58
Axial, 15mm	1.40	1.12	2.17

Table 4.3: Spatial resolution performance (in mm) at one-fourth of the axial FOV of the high resolution scanner (+6 mm from the center slice) for the high, mixed, and standard resolution systems. Measurements are derived from MLEM reconstructions (see Section 3.2) of Monte Carlo simulations conducted in GATE.

if resolution is over-modeled (for example, the blurring kernel is not appropriately matched to the actual system resolution), distortions can occur. In these cases, the reconstruction algorithm may attempt to incorrectly reduce an object's size, and points or edges that are not actually present in the data can manifest. This likely contributes to the larger FWHM measurements for the mixed resolution scanner compared to the standard resolution scanner

Spatial Resolution in FWHM (mm), 1/4 of Axial FOV of Mixed Resolution System		
Parameter	Mixed Resolution	Standard Resolution
Radial, center	2.18	1.36
Tangential, center	2.17	1.35
Axial, center	2.60	1.34
Radial, 5mm	2.37	1.80
Tangential, 5mm	1.97	1.62
Axial, 5mm	1.83	1.78
Radial, 10mm	3.18	3.49
Tangential, 10mm	1.74	1.61
Axial, 10mm	2.04	1.97
Radial, 15mm	3.61	4.46
Tangential, 15mm	2.04	1.56
Axial, 15mm	2.26	2.16

Table 4.4: Spatial resolution performance (in mm) at one-fourth of the axial FOV of the mixed and standard resolution scanners (18.0 mm from the center slice). Measurements are derived from MLEM reconstructions (see Section 3.2) of Monte Carlo simulations conducted in GATE.

for the slice at plus 18 mm in the axial direction, especially since the spatial resolution of objects in this slice have significant contributions from both mixed and standard resolution data.

In this work, a uniform blurring function per each axial slice was used to model the resolution. The blur used to characterize each slice was measured at the transverse center of

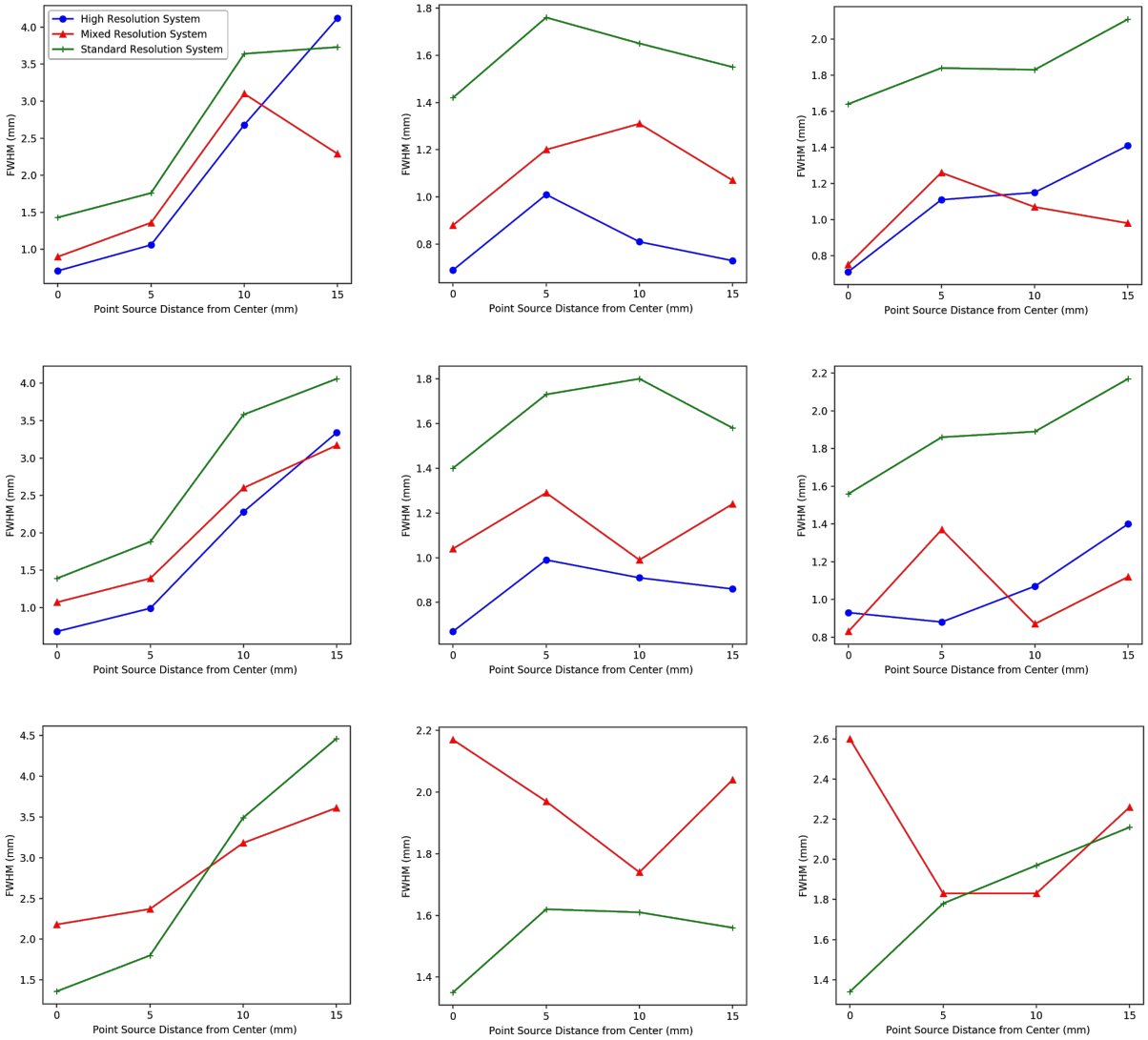

Figure 4.5: Plots showing the change in radial (left), tangential (center), and axial (right) resolution performance for a point source with distance from the center of the FOV for the high (blue), mixed (red), and standard (green) resolution systems. The central slice is shown in the top row, 6 mm from axial center in the middle row, and 18 mm from axial center in the bottom row.

the slice, meaning there was a possibility that it would not adequately characterize off-axis resolution, especially given the non-uniformities in resolution introduced by using mixed resolution data. However, the uniform blur per slice assumption does appear to hold well for the point sources at center and at 5 mm off-axis in the high resolution region. While dis-

tortions do start to appear at off-axis positions, mixed resolution performance still appears to generally outperform the standard resolution case and sometimes approach the high resolution case. Refinements to the resolution model to avoid over-modeling could potentially lead to improvements in resolution performance at these other locations and a reduction in any potential resulting image distortions.

4.3 Contrast Recovery

One of the central advantages of the mixed resolution scanner in this study compared to the high resolution scanner is its substantially higher sensitivity (as discussed in Section 4.1). The benefits of this increased sensitivity include a higher count rate that, for an image acquired for the same amount of time, could lead to less image noise and higher object detectability compared to the high resolution scanner.

Moreover, the higher resolution performance of the mixed resolution scanner compared to the standard resolution scanner means that it may yield images with better contrast. Specifically in PET, the partial volume effect, wherein the activity within a small object appears lower than its actual value, is a major factor in reduced contrast that can be diminished with improved spatial resolution. Additionally, if a small region of interest has a low uptake ratio compared to its surrounding tissue, better spatial resolution performance can increase the detectability of that region [7]. For these reasons, we looked at the potential of our mixed resolution concept to improve the contrast recovery and reduce noise.

4.3.1 Methods

Data acquisition of the uniform and contrast recovery regions of the NEMA NU 4-2008 [76] preclinical image quality phantom, placed at the center of the FOV, were simulated in GATE for the high, mixed, and standard resolution scanners. The activity per volume was the same for all regions of the phantom. The uniform region of the phantom was 30 mm

in diameter and 30 mm in axial extent, and it was oriented towards one of the standard resolution detector regions. The contrast recovery region of the phantom was made up of 5 rod sources 20 mm in length and of varying diameters. The standard diameter range of this phantom varies from 1 to 5 mm, but to better test the resolution and sensitivity performance of our systems, the diameters were scaled down to vary from 0.6 to 3 mm. For the same acquisition time, the high resolution scanner acquired 17 million events while the mixed and standard resolution scanners acquired 88 million events. Data was converted to histogram format and reconstructed for 20 iterations using the MLEM algorithm described in Chapter 3.

We followed the NEMA protocol for measuring the recovery coefficient of the 5 "hot" rod regions as well as the mean and standard deviation of the uniform region. In brief, we first found the mean and standard deviation in the uniform region of the phantom using a 22.5 mm diameter and 4 mm long volume of interest. Typically a 10 mm long volume is used, but the 4 mm length was chosen here because only 4 mm of the uniform region of the phantom was contained by the high resolution FOV, and we wished to utilize the same volume for all three uniformity calculations. Then, in the contrast recovery section of the phantom, the central 10 mm length of each rod was averaged to a single slice with less noise. A circular ROI was drawn around each rod such that it's diameter was twice that of the rod, and the location with the maximum value in the ROI was identified. These locations were used to generate line profiles axially along the rods, which were divided by the mean value of the uniform region to calculate the recovery coefficients at each voxel along the line and from which the mean and standard deviation of the recovery coefficient were derived. Per the NEMA protocol, the percent standard deviation was calculated as

$$\%STD_{RC} = 100\sqrt{\left(\frac{STD_{LineProfile}}{Mean_{LineProfile}}\right)^2 + \left(\frac{STD_{background}}{Mean_{background}}\right)^2}. \tag{4.1}$$

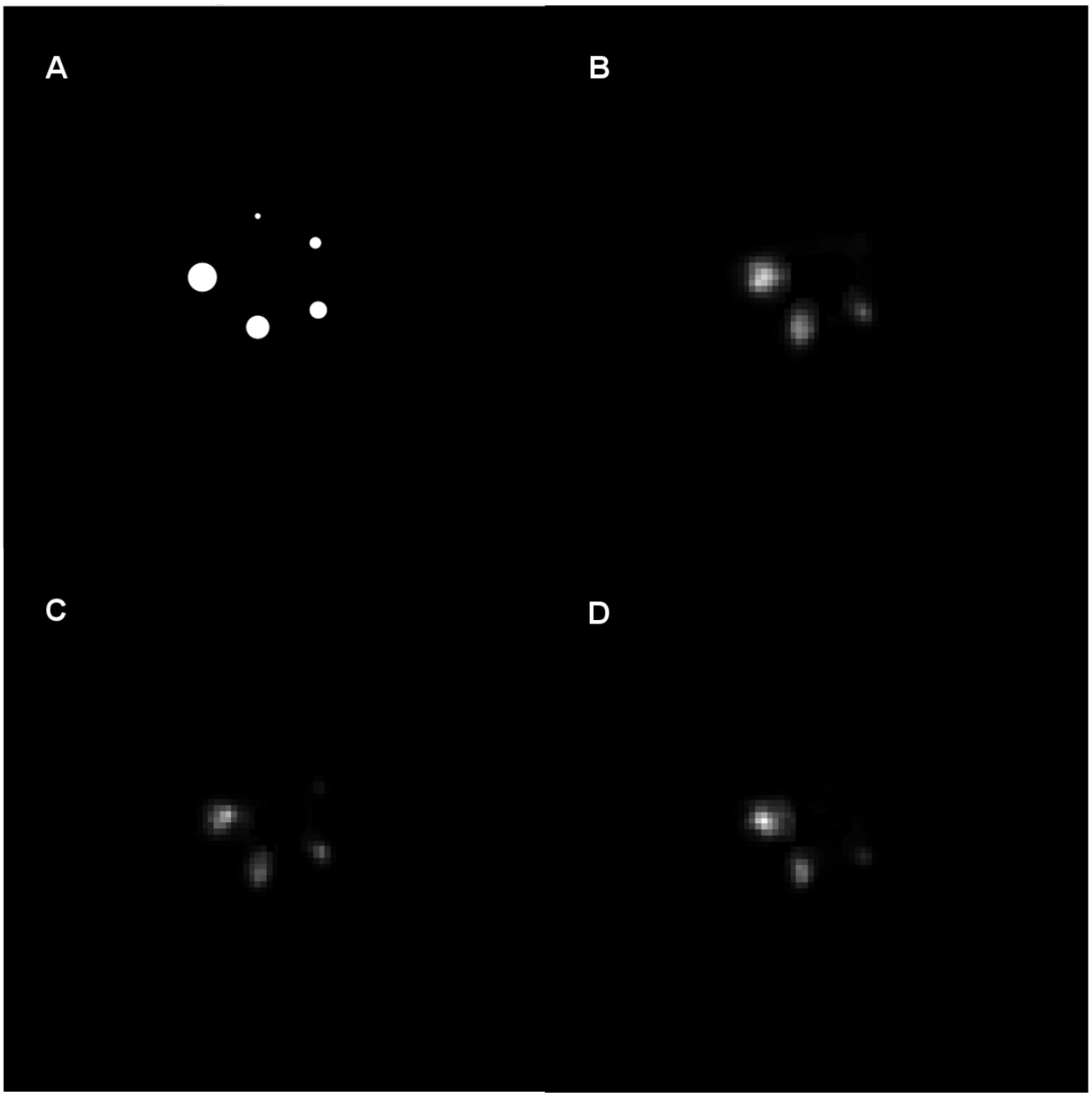

Figure 4.6: (A) The contrast recovery section of the NEMA preclinical image quality phantom. Reconstructed images from data simulated via Monte Carlo in GATE are shown for the B) mixed resolution, C) high resolution, and D) standard resolution scanners, respectively. Three rods are clearly visible for all three systems, while the fourth rod, 1.2 mm in diameter, can just be seen in the reconstructed image for the high resolution system.

4.3.2 Results and Discussion

Reconstructed images of the contrast recovery region of the NEMA image quality phantom are shown in Figure 4.6. The contrast recovery performance of the three scanners is shown

in Figure 4.7, which plots the recovery coefficient for the 5 rods. The first three rods are recovered adequately by all three systems, with the mixed resolution system performing in between the standard and high resolution systems. The 1.2 mm rod was adequately recovered by the high resolution, but not as well-recovered by the mixed resolution system, with the recovery coefficient approaching that of the standard resolution system. The 0.6 mm rod was not well-recovered by any of the three systems.

The $\%STD_{RC}$ of the five rods for all three scanner configurations is shown in Figure 4.8. The high resolution scanner had a higher $\%STD_{RC}$ for all of the rods, and there is a comparatively better noise performance for the mixed and standard resolution scanners, which have higher sensitivity. This sensitivity is accounted for in the data by the larger number of events used to reconstruct the mixed and standard resolution images, which were assumed to be collected using the same acquisition parameters for all three systems. This better $\%STD_{RC}$ for the mixed resolution system compared to the high resolution system likely plays a role in the mixed resolution system's contrast recovery performance approaching that of the high resolution system. Additional improvements of the spatial resolution performance of the mixed resolution system through further optimization of the image reconstruction methods could lead to even further improvements in contrast recovery.

4.4 Summary

In this chapter, we compared a mixed spatial resolution PET scanner concept with a centrally-located high resolution region to two other scanners in order to study its performance capabilities. For comparison, the high resolution region of the mixed resolution system was tested as a stand-alone system, and a system using standard resolution detectors with otherwise the same geometry as the mixed resolution scanner was tested. These scanners were studied in terms of their sensitivity, spatial resolution and contrast recovery performance. In all three studies, the mixed resolution system showed performance advan-

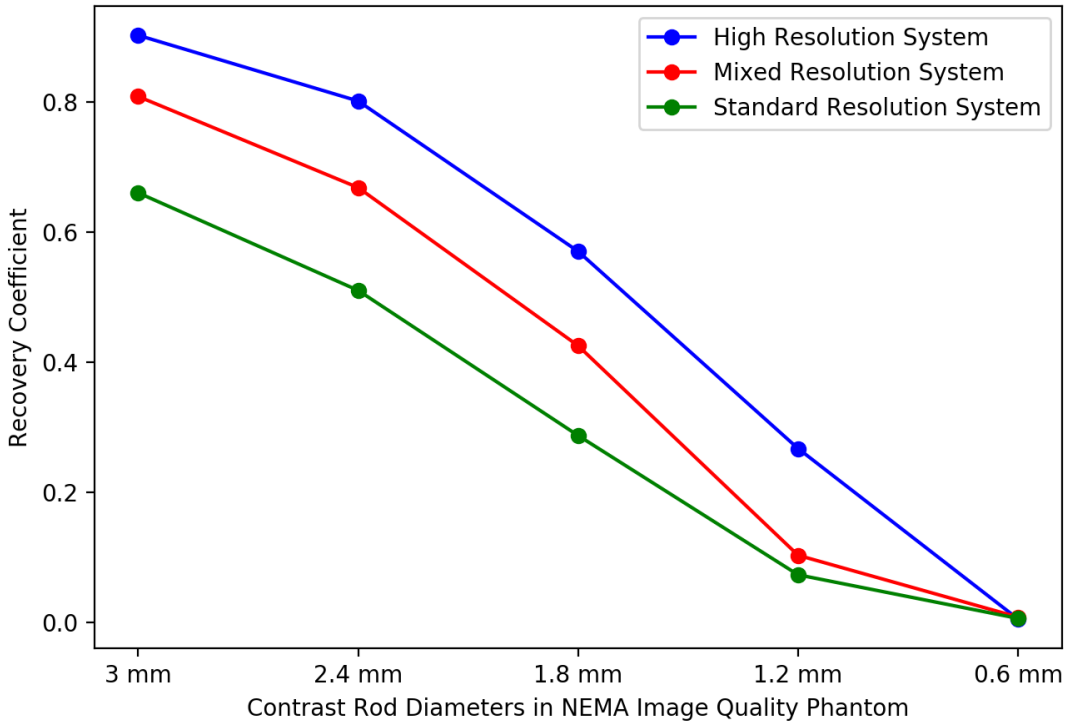

Figure 4.7: The recovery coefficients for each of the 5 rods for the 3 scanner configurations. Only the three largest diameter rods were visible in the reconstructions.

tages. The mixed resolution case demonstrated substantially better system sensitivity than the high resolution system while outperforming the standard resolution system in terms of spatial resolution within the region of the scanner covered by the high resolution detectors. The mixed resolution scanner also showed better spatial resolution compared to the standard resolution system as well as a lower noise level due to its higher sensitivity compared to the high resolution system.

These studies also demonstrated the limits of the uniform-per-axial-slice resolution model utilized in image reconstruction for these studies. The over-modeling of the resolution closer to the edge of the transverse FOV and at large distances from the axial center can be improved with more more location-specific refinement of the the blurring function used to model the resolution. The most straightforward approach would be to sample the system response

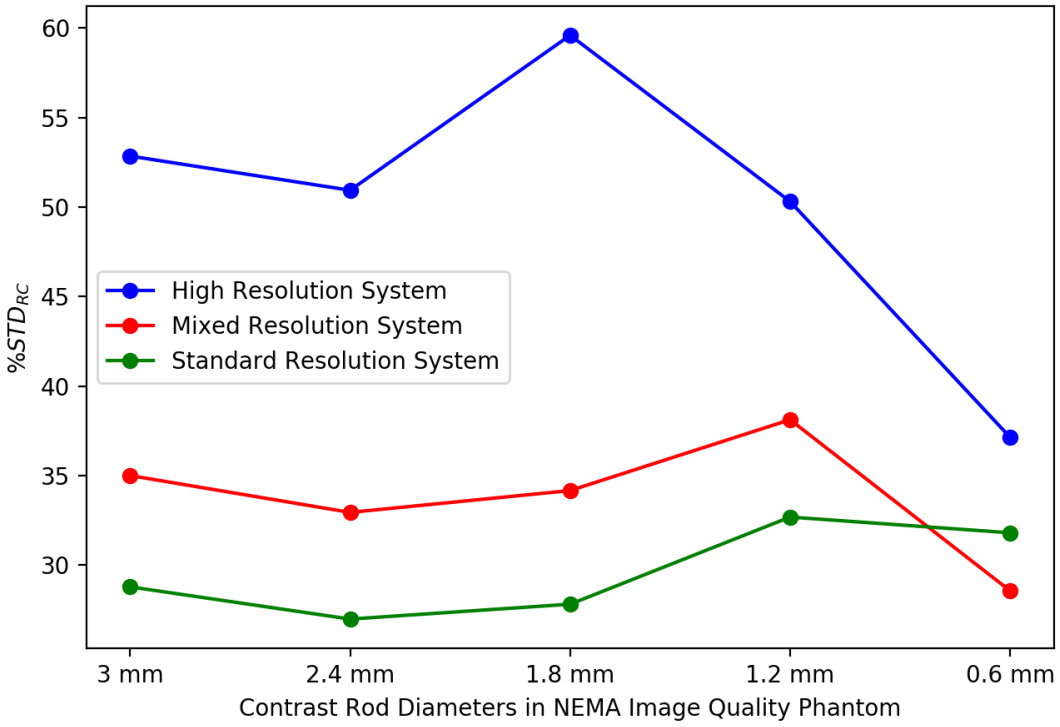

Figure 4.8: The $\%STD_{RC}$ for each of the 3 scanner configurations. Only the values for the three largest diameter rods are shown since the others were not recovered in the reconstructions.

function function to point sources at a higher density than the single point source response per slice used in this work. However, even with the straightforward per-slice approach used here, the trend of improved resolution for the mixed resolution detector case is apparent.

CHAPTER 5

EVALUATING PERFORMANCE OF MIXED RESOLUTION PET SYSTEM WITH END-LOCATED HIGH RESOLUTION REGION

In the previous chapter, using the simulation and reconstruction tools we developed in Chapter 3, we studied the feasibility of a specific mixed resolution PET scanner design with a centrally located high resolution detector region to achieve comparable or improved image quality when examined against systems with high resolution and standard resolution detectors alone. We now turn to another mixed resolution scanner concept incorporating the high resolution detector region at one axial end of the scanner.

The motivation for this scanner configuration includes the desire to image in high resolution regions of interest in an object not necessarily at the object's center. For example, in the case of brain imaging, where one may not need as high resolution in the rest of the body but still want to have an image of that region, this orientation could potentially provide high resolution images of the brain and standard resolution images of the rest of the body.

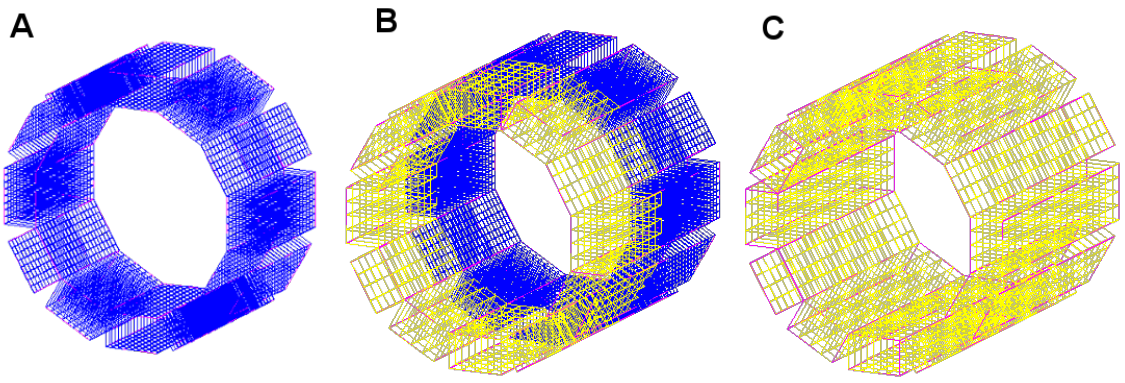

Figure 5.1: Visualizations of the three scanner configurations as simulated in GATE: A) the high resolution scanner, B) mixed resolution scanner, half high resolution detectors (in blue) and half standard resolution detectors (in yellow), and C) the standard resolution scanner.

System Parameter	High Resolution	Mixed Resolution		Standard Resolution
		High Resolution Module	Standard Resolution Modules	
Ring Diameter (mm)	60	60	60	60
Crystal Pitch (mm)	2.0	2.0	4.0	4.0
Crystal Size (mm^3)	2×2×10	2×2×10	4×4×10	4×4×10
Detectors Per Module	8×18	8×18	4×9	4×18
Detectors Per Ring	96	96	48	48
Field of View (mm^3)	48×48×36	48×48×72		48×48×72

Table 5.1: Parameters describing the scanner configurations for the high, mixed and standard resolution systems studied in Chapter 5. Details for both the high and standard resolution regions of the mixed resolution scanner are provided.

This configuration also moves the regions of the scanner that utilize mixed resolution data compared to the scanner studied in the previous chapters. That scanner combined high, mixed, and standard resolution data in the central region of the scanner encompassed by the high resolution detectors. Objects more axially distant from the center of the field of view (FOV) provided less high and mixed resolution data for reconstruction. In the scanner studied in this chapter, the scanner can be roughly divided into three regions in terms of the resolution properties of the collected data: the high resolution detector region at one end, the standard resolution detector region at the other end, and a central region that transitions from high to standard resolution. At one end of this transition region is primarily high resolution data, but as one moves closer to the axial center more mixed resolution data is also provided. After crossing the the central slice of the scanner, mixed and standard resolution data are generated, eventually transitioning to the region dominated by standard resolution data.

In order to assess the feasibility of this alternative mixed resolution scanner geometry, we compare its performance to a high resolution scanner, equivalent in geometry to the high resolution region of the mixed resolution scanner, and a standard resolution scanner. Details of the three scanners' parameters are found in Table 5.1, and the scanners are shown in Figure 5.1.

We first compare the sensitivity of the scanners in Section 5.1, demonstrating the superior performance of the mixed and standard resolution scanners. This is followed by an examination of spatial resolution capabilities for the three scanners in Section 5.2, and then an examination of their contrast recovery performance in Section 5.3.

5.1 Sensitivity Performance

PET scanner sensitivity, discussed in more depth in Section 2.2, is primarily determined by both the detectors' solid angle coverage of the FOV of the scanner and the material and size of the crystal scintillators used in the detector modules. In this work, we use LSO crystals, due to this materials common use in most current scanner designs, and each crystal is 10 mm in thickness, which is a compromise between sensitivity and and an attempt to reduce loss of resolution effects from depth-of-interaction blurring.

5.1.1 Methodology

GATE was used to simulate point sources at the center of the transverse FOV at 1 mm intervals along the axial direction. The point source was specefied as 100 kBq and data was collected for 100 seconds. The absolute sensitivity of the scanner for each point source location was recorded as a percentage of the known total events emitted. The mixed and standard resolution scanners, which have exactly the same solid angle coverage and crystal volume, were assumed to have identical sensitivities, and so only the mixed resolution case is reported.

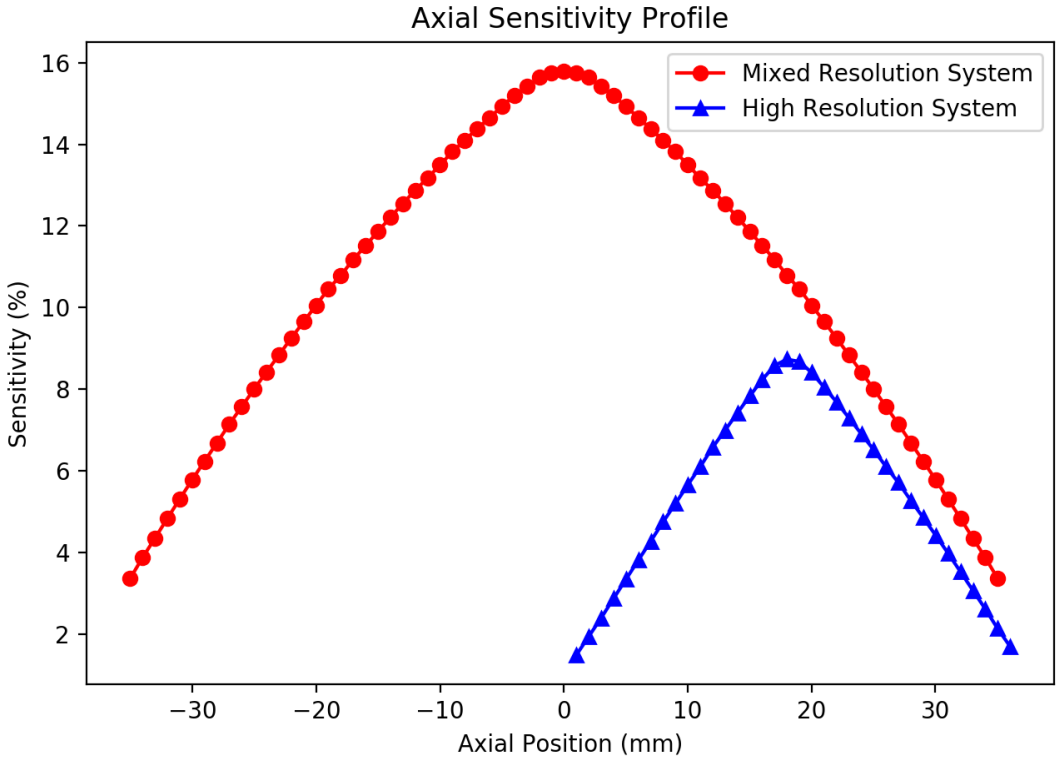

Figure 5.2: The axial sensitivity profile of mixed and high resolution scanners measured using GATE simulation of point sources stepped axially along the center of the scanner. The standard resolution system has equivalent sensitivity to the mixed resolution system and is therefore not shown. The high resolution scanner is offset from center to align with the region of the mixed resolution scanner that also contains high resolution detector modules.

5.1.2 Results and Discussion

Axial sensitivity profiles for the mixed and high resolution scanners are shown in figure 5.2. The high resolution scanner is offset from center to align with the high resolution detector region of the mixed resolution scanner. The peak sensitivity at center for the mixed and standard resolution scanners is 15.79%. For the high resolution system, the peak sensitivity is 8.74%. The sensitivity of the mixed resolution scanner at 18 mm from the central slice, corresponding to the same location as the peak location of the high resolution scanner, has a sensitivity of 10.79%. At the edge of the high resolution scanner's axial FOV, the sensitivity is 1.48%, whereas the mixed and standard resolution scanners have a 3.36% sensitivity at

the edge of the axial FOV. This higher sensitivity for the larger-FOV mixed and standard resolution scanners demonstrates the benefit of extending the axial FOV, even if the extension uses more affordable, lower spatial resolution performance detectors in order to reduce cost.

5.2 Spatial Resolution Performance

The primary determinant of spatial resolution performance for most PET imaging systems is the physical size of the individual detectors of which it is made up. The mixed resolution scanner concept we are studying here employs detectors with high and standard resolution capabilities, with their size ($2\times2\times10$ mm^3 and $4\times4\times10$ mm^3, respectively) being a surrogate for this performance capability. The high resolution detectors at one end of the scanner and the standard resolution detectors at the other combine for objects in the axial middle of the scanner to generate mixed resolution data, which essentially averages the resolution performance of the two detectors. In this central region, high resolution data, standard resolution data and mixed resolution data contribute to the image quality, with the lower resolution data from the mixed and standard resolution lines of response potentially contributing to blurring of the high resolution data if unaccounted for. In Chapter 3, we developed an image space resolution model for our MLEM reconstruction algorithm to account for this blur and potentially recover some or all of the resolution capability of the high resolution data. We used this technique to examine the potential of the mixed resolution system to achieve the high spatial resolution performance of the high resolution scanner system and to outperform the standard resolution scanner.

5.2.1 Methods

For each scanner configuration, point sources with 100 kBq activity were simulated via Monte Carlo methods in GATE. Sources were placed on the central axial slice, at 1/4 the axial length of the high resolution detector (9 mm in the z-direction), and at 1/4 the axial length

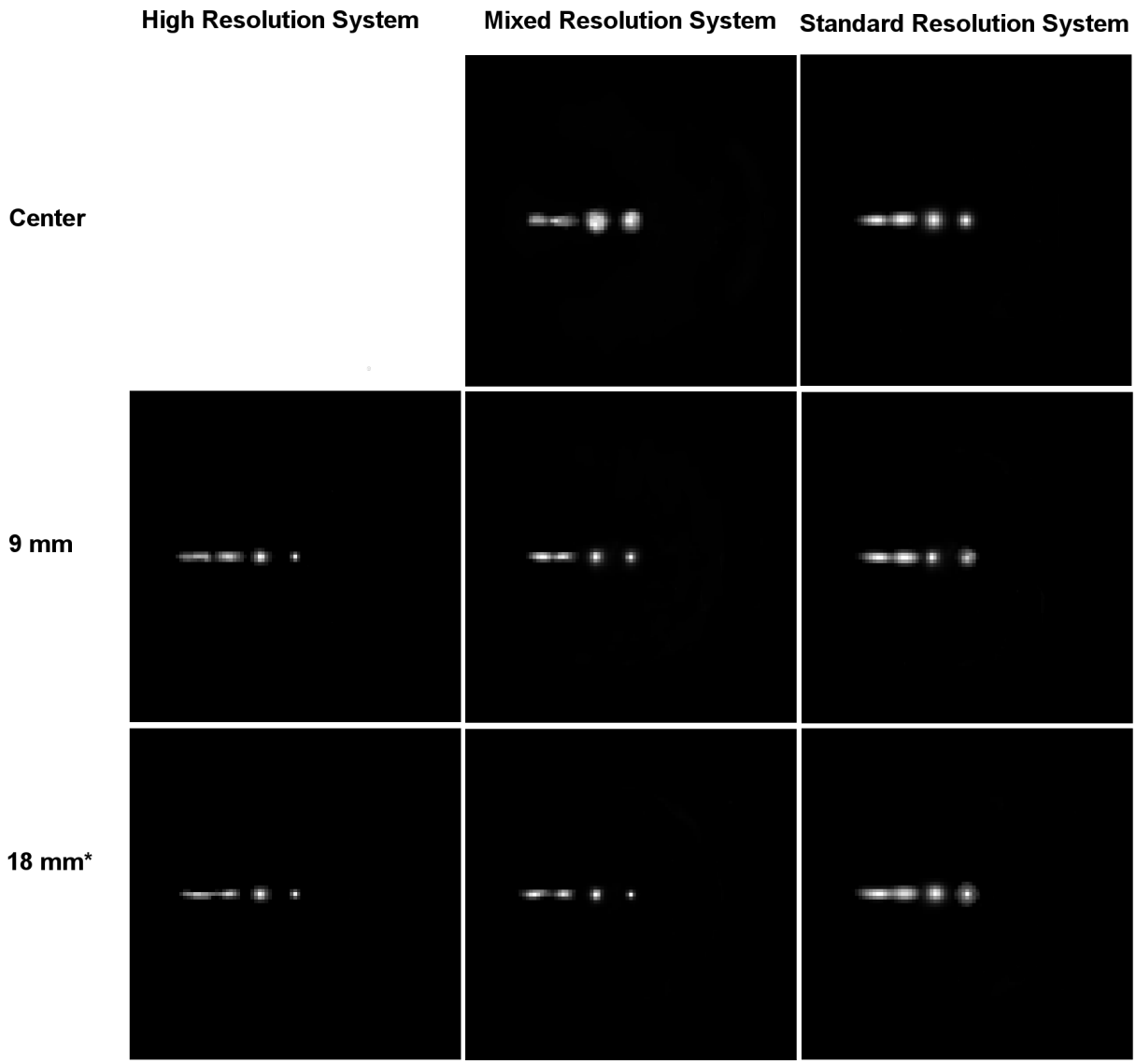

Figure 5.3: Overlayed transverse slice images of single point source reconstructions for point sources located at transverse center as well as 5, 10, and 15 mm from center. Three different axial locations (center and 6 mm from center for all three scanners and 18 mm from center for the mixed and standard resolution systems) are shown (arranged by row) for the different scanner configurations (arranged by column). The images demonstrate the radial and tangential resolution performance of the three scanner configurations. Each point source is shown in the image scaled to it's own maximum.

of the mixed and standard resolution scanners (18 mm in the z-direction). Four locations per slice were studied: at center and at 5, 10, and 15 mm in the positive x-direction. Data was acquired for 100 seconds and the first million events were extracted and converted to

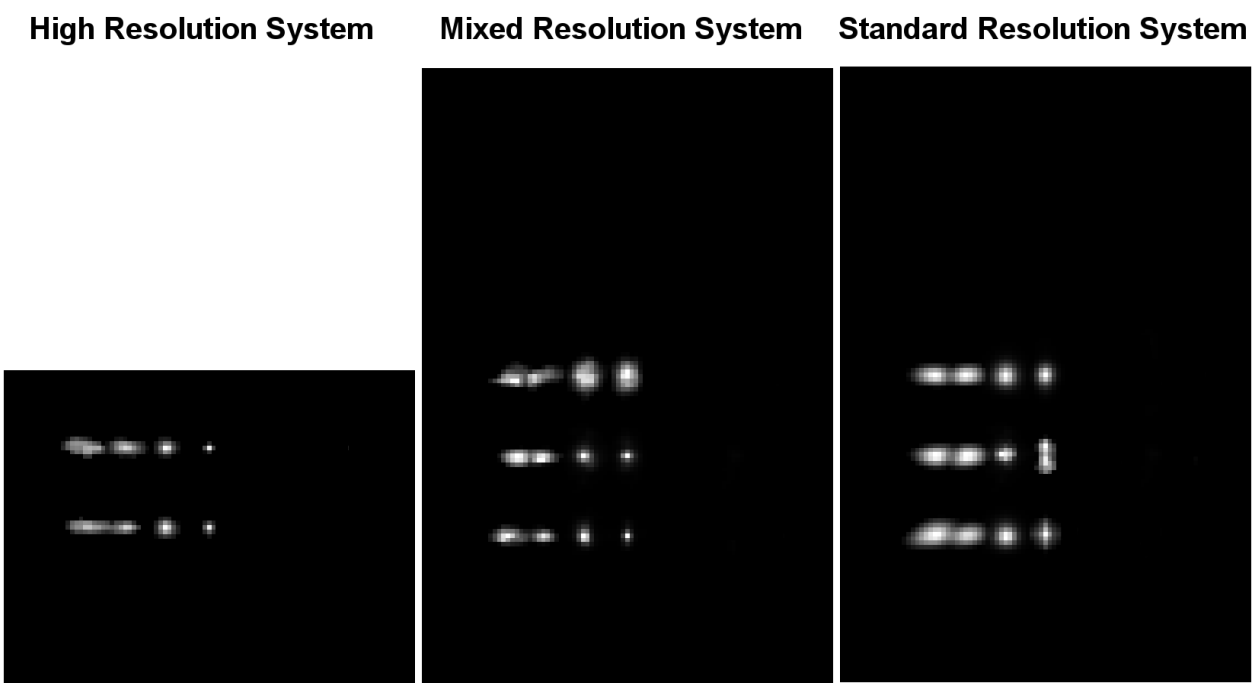

Figure 5.4: Overlayed coronal slice images of single point source reconstructions for point sources located at transverse center as well as 5, 10, and 15 mm from center. Three different axial locations (center as well as 6 and 18 mm from center) are shown (stratified vertically in each coronal image) for all three scanner configurations (arranged by column). Each point source is shown in the image scaled to it's own maximum.

histogram format for reconstruction. Reconstructions were performed through 20 iterations on a 93×93×139 voxel grid for the mixed and standard resolution scanners and a 93×93×71 voxel grid for the high resolution scanner, with a 0.5×0.5×0.5 mm^3 voxel size. A low-activity cylinder of known uniform background and with diameter and length equal to the FOV was incorporated with the simulation to avoid arbitrarily small resolution as desribed in Qi *et al.* [85]. Following Liu *et al.* [70] and Li *et al.* [68], we used a ratio of 200-to-1 between point source and background activity.

FWHM values were measured for each point source using the linear interpolation described in NEMA NU-4 2008 [76]. In brief, a line profile through the source location was collected in the radial, tangential and axial directions and the maximum values for each line were identified. The points along the line profile nearest the half-maximum value on each side

Spatial Resolution in FWHM (mm), 1/4 of Axial FOV of Mixed Resolution System, Center of Axial FOV of High Resolution System			
Source Location	High Resolution	Mixed Resolution	Standard Resolution
Radial, center	0.84	0.66	1.36
Tangential, center	0.81	0.67	1.35
Axial, center	0.85	0.79	1.34
Radial, 5mm	1.43	1.11	1.80
Tangential, 5mm	1.23	1.13	1.62
Axial, 5mm	1.37	1.24	1.78
Radial, 10mm	3.4	1.92	3.49
Tangential, 10mm	1.24	1.02	1.61
Axial, 10mm	1.54	1.12	1.97
Radial, 15mm	4.17	2.33	4.46
Tangential, 15mm	1.6	0.93	1.56
Axial, 15mm	2.38	1.22	2.16

Table 5.2: Spatial resolution performance (in mm) at at one-fourth of the axial FOV of the mixed and standard resolution scanner (18.0 mm from their center slice), which is also the center slice for the high resolution scanner. Measurements at center, 5, 10, and 15 mm from the center voxel are derived from MLEM reconstructions (see Section 3.2) of Monte Carlo simulations conducted in GATE.

of the peak were identified, and linear interpolation was used to calculate the locations of the half-maximums. The distance between these two points was the FWHM in that direction.

Spatial Resolution in FWHM (mm), 1/4 of Axial FOV of High Resolution System			
Parameter	High Resolution	Mixed Resolution	Standard Resolution
Radial, center	0.82	0.97	1.85
Tangential, center	0.78	0.96	1.80
Axial, center	0.66	0.78	3.92
Radial, 5mm	1.36	1.22	1.73
Tangential, 5mm	1.31	1.33	1.58
Axial, 5mm	1.13	1.01	1.93
Radial, 10mm	3.20	2.76	3.73
Tangential, 10mm	1.30	1.08	1.61
Axial, 10mm	1.44	1.32	2.13
Radial, 15mm	4.84	2.87	3.82
Tangential, 15mm	1.50	1.53	1.66
Axial, 15mm	2.58	2.01	2.12

Table 5.3: Spatial resolution performance (in mm) at 1/4 of the axial FOV of the high resolution scanner (+9 mm from its center slice) which is 1/8 of the axial FOV of the mixed and standard resolution systems. Measurements are derived from MLEM reconstructions (see Section 3.2) of Monte Carlo simulations conducted in GATE.

5.2.2 Results and Discussion

Table 5.2 -5.4 show the FWHM measurements at different axial slices for the three scanner configurations, and images of the reconstructed point sources are shown for the high, mixed and standard resolution scanners in Figures 5.3 and 5.4. The change in resolution performance with distance from the center of the FOV is plotted for each scanner configuration in

Spatial Resolution in FWHM (mm), Center of Axial FOV of Mixed Resolution System		
Parameter	Mixed Resolution	Standard Resolution
Radial, center	2.14	1.43
Tangential, center	2.11	1.42
Axial, center	2.63	1.64
Radial, 5mm	2.29	1.76
Tangential, 5mm	2.51	1.76
Axial, 5mm	2.08	1.84
Radial, 10mm	2.97	3.64
Tangential, 10mm	1.44	1.65
Axial, 10mm	1.55	1.83
Radial, 15mm	4.2	3.73
Tangential, 15mm	1.57	1.55
Axial, 15mm	1.64	2.11

Table 5.4: Spatial resolution performance (in mm) at the center of the axial FOV of the mixed and standard resolution scanners. Measurements are derived from MLEM reconstructions (see Section 3.2) of Monte Carlo simulations conducted in GATE.

Figure 5.5.

Table 5.2 compares the resolution performance at the center of the high resolution scanner to resolution performance at the same location of the high resolution region of the mixed resolution scanner as well as at that axial location for the standard resolution scanner. At this slice, the mixed resolution system demonstrates substantially improved spatial resolution

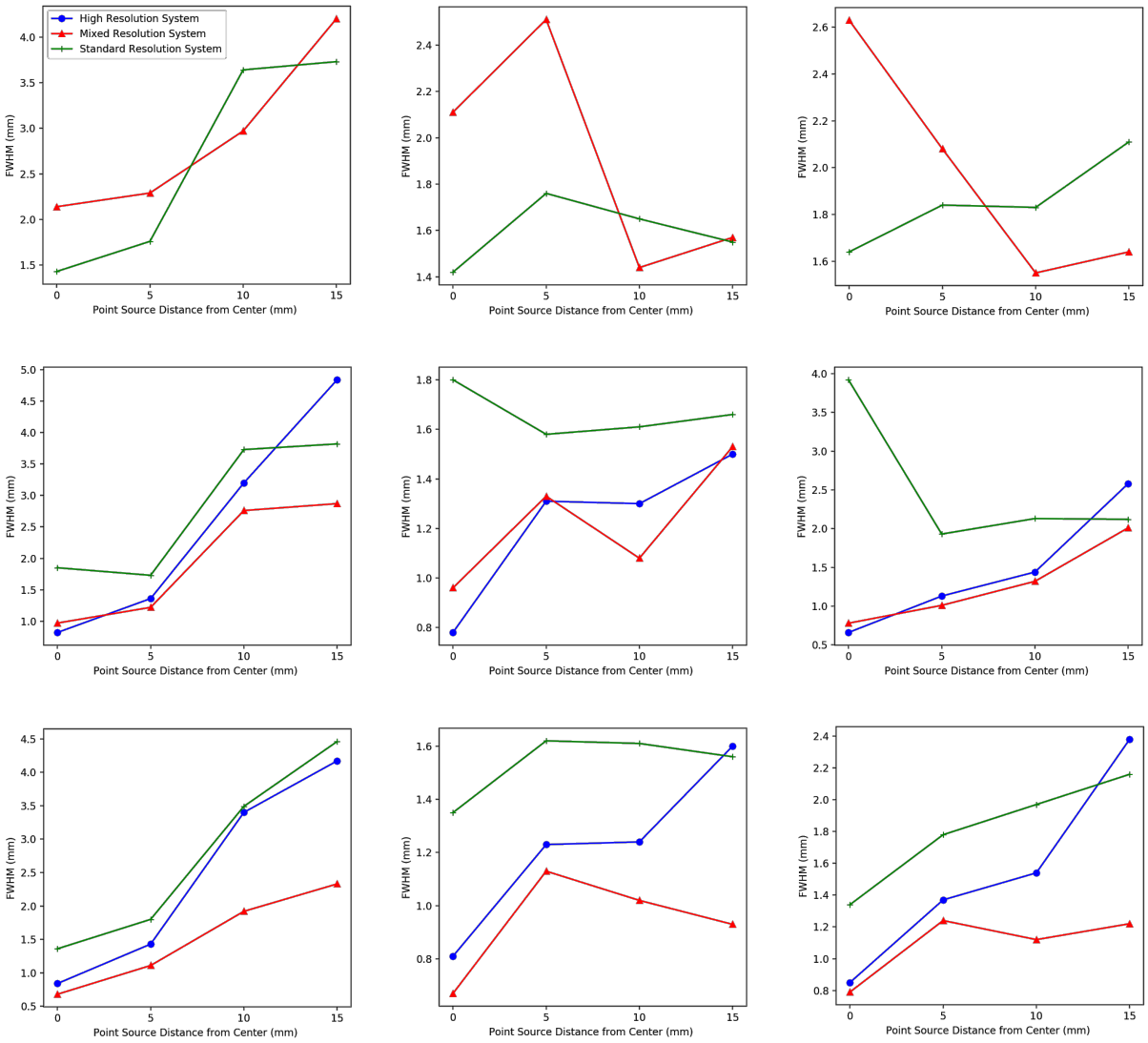

Figure 5.5: Plots showing the change in radial (left), tangential (center), and axial (right) resolution performance for a point source with distance from the center of the FOV for the high (blue), mixed (red), and standard (green) resolution systems. The central slice of the mixed and standard resolution systems is shown in the top row. For all three scanners, point sources located at 9 mm from axial center are shown in the middle row, and point sources located at 18 mm from axial center (the center of the high resolution system FOV) are shown in the bottom row.

compared to the standard resolution system and has comparable performance to the high resolution scanner. Because these measurements are performed in the middle of the high resolution region, where most data is determined by the high spatial resolution detectors, one

would expect roughly equivalent performance between mixed and high resolution scanners.

For the measurements taken at 1/4 the axial FOV of the high resolution scanner (9 mm from the central slice), the mixed resolution case once again performs very well compared to the high resolution scanner and demonstrates much higher spatial resolution compared to the standard resolution scanner. For the mixed resolution scanner, this location is also encapsulated by high resolution detectors, though some mixed resolution data is expected to contribute. However, this data does not appear to degrade the spatial resolution performance.

Finally, for the measurements taken at the axial center of the mixed and standard resolution scanners (reported in Table 5.4), the mixed resolution scanner demonstrates larger FWHM values than the standard resolution scanner for some measurements. Because this location is at the center of the region most affected by mixed resolution data, the measured spatial resolution performance is the most to likely to demonstrate any inaccuracies in the resolution model used in reconstruction. Our implementation of the resolution model utilized a single blurring function matched to the resolution at the center of the transverse field of view, which may be inadequate for the most challenging regions of the FOV where spatial resolution performance is less uniform. Moreover, as reported by Reader *et al.* [91], while a resolution model implemented accurately can contract the signal at the location of event to match their true resolution, if implemented inaccurately, modeling the system response function can result in incorrectly reducing regions of the image, causing ringing and other structures that are not present in the true signal distribution. Inaccuracies in the model might further explain the worse spatial resolution performance at this location. Future improvements to the resolution model, such as more widely and frequently sampling the system response function across the FOV, could confirm if this is the case.

5.3 Contrast Recovery

A motivating factor for evaluating the feasibility of the mixed resolution scanner concept is to identify a method of incorporating better performing spatial resolution detectors in PET systems without reducing the FOV due to cost constraints. Such a reduction in FOV leads also to a loss of sensitivity, as demonstrated by the difference in measured sensitivity in Section 5.1. The benefits of higher sensitivity include a higher count rate, leading to either faster imaging times or more counts for the same scan time, potentially reducing noise and increasing object detectability. Incorporating higher resolution detectors in your scanner also contributes substantially to improving object detection, by reducing the impact of the partial volume effect. For these reasons, we sought to evaluate the ability of the mixed resolution scanner with regard to contrast recovery and compare it to the performance of the high and standard resolution scanners.

5.3.1 Methodology

For the three scanners studied, we acquired data from GATE simulations of the uniform and contrast recovery regions of the NEMA NU 4-2008 [76] preclinical image quality phantom, placed at the center of the high resolution region of the mixed and high resolution scanners (centered at plus 18 mm from the mixed and standard resolution central slice). The activity per volume was the same for all regions of the phantom. The uniform region of the phantom was 30 mm in diameter and 30 mm in axial extent, and it was oriented towards the center of the axial FOV of the mixed and high resolution systems. The contrast recovery region of the phantom was made up of 5 rod sources 20 mm in length and of varying diameters. The standard diameter range of this phantom varies from 1 to 5 mm, but to better test the resolution and sensitivity performance of our systems, the diameters were scaled down to vary from 0.6 to 3 mm. For the same acquisition time, the high resolution scanner acquired 45 million events while the mixed and standard resolution scanners acquired 149 million

events. Data was converted to histogram format and reconstructed for 20 iterations using the MLEM algorithm described in Chapter 3.

We followed the NEMA protocol for measuring the recovery coefficient of the 5 "hot" rod regions as well as the mean and standard deviation of the uniform region. In brief, we first found the mean and standard deviation in the uniform region of the phantom using a 22.5 mm diameter and 8 mm long volume of interest. Then, in the contrast recovery section of the phantom, the central 10 mm length of each rod was averaged to a single slice with less noise. A circular ROI was drawn around each rod such that its diameter was twice that of the rod's expected diameter, and the location with the maximum value in the ROI was identified. These locations were used to generate line profiles axially along the rods, which were divided by the mean value of the uniform region to calculate the recovery coefficients at each voxel along the line and from which the mean and standard deviation of the recovery coefficient were derived. The percent standard deviation ($\%STD_{RC}$) was calculated as per the NEMA protocol described in Equation 4.1.

5.3.2 Results and Discussion

Figure 5.6 shows reconstructed transverse slices through the center of the contrast recovery region of the NEMA image quality phantom. The recovery coefficients for all three scanners are shown in Figure 5.7. The three largest rods were recovered well by all three systems, while the 1.2 mm rod was not well-recovered by the standard resolution system. The 0.6 mm rod was not well-recovered by any of the three systems. The mixed resolution system contrast recovery performance approaches that of the high resolution system, matching it for the 1.2 mm diameter rod, the smallest diameter rod one expects to recover well given the spatial resolution performance of the two systems. Moreover, the mixed resolution system outperforms the standard resolution system for the three largest rods and is able to recover the 1.2 mm rod with which the standard resolution system has difficulty due to its worse

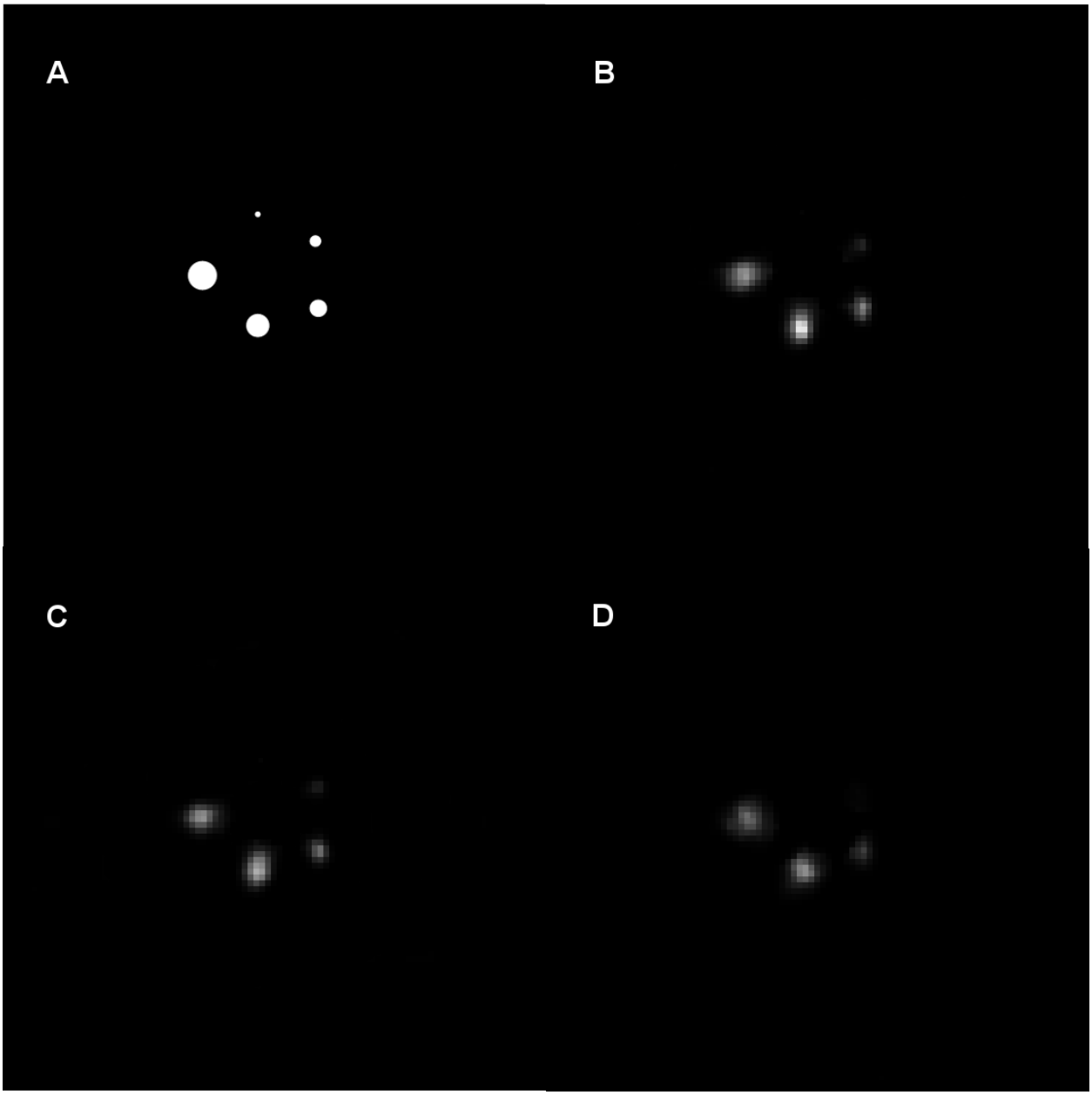

Figure 5.6: (A) The contrast recovery section of the NEMA preclinical image quality phantom. Reconstructed images from data simulated via Monte Carlo in GATE are shown for the B) mixed resolution, C) high resolution, and D) standard resolution scanners, respectively. Four rods are visible for the high and mixed resolution systems, while only three can be seen clearly in the reconstruction for the standard resolution system.

spatial resolution performance.

Figure 5.8 shows the $\%STD_{RC}$ value for each of the 5 rods, which provides some mea-

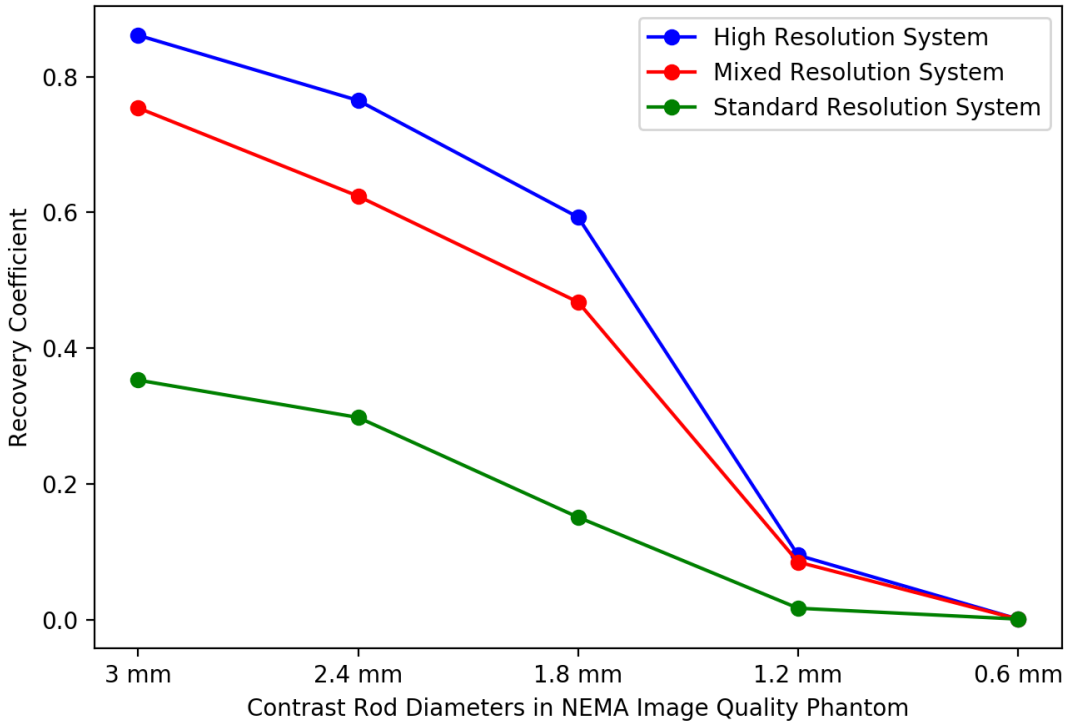

Figure 5.7: The recovery coefficients for each of the 5 rods for the 3 scanner configurations. The mixed resolution consistently outperforms the standard resolution system except at the smallest diameter rod.

sure of the role of noise in contrast recovery for each system. The three systems have similar $\%STD_{RC}$ values for the three largest diameter rods, which were clearly recovered by all three systems. However, for the two smallest rods which are more challenging to recover, the mixed and standard resolution systems have lower $\%STD_{RC}$, an indication of the benefit of the additional sensitivity of these two scanners to reduce noise. These mixed and standard resolution scanners collected over three times more events using the same acquisition parameters. This added sensitivity paired with the higher resolution performance in the mixed resolution system lead to a clear advantage over the standard resolution system and with further optimization of reconstruction tools developed in Chapter 3, the potential to match or even outperform the high resolution system in terms of contrast recovery.

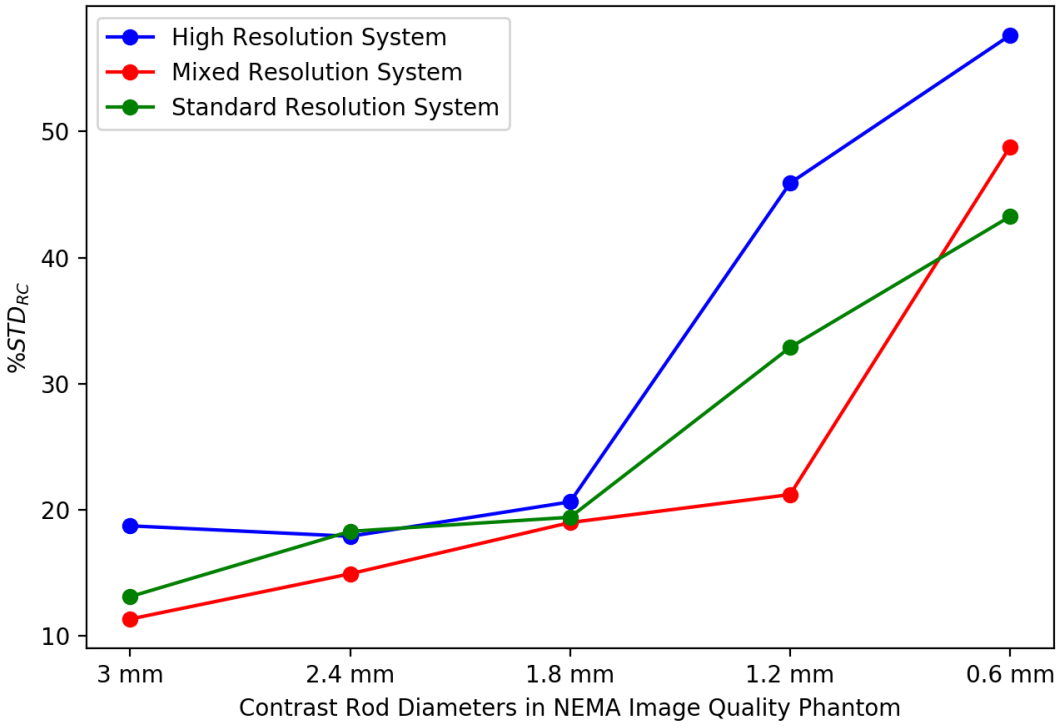

Figure 5.8: The $\%STD_{RC}$ for each of the 5 rods for the the 3 scanner configurations. $\%STD_{RC}$ increases for smaller diameter rods for all thee systems, with the largest increase for the high resolution system.

5.4 Summary

In this chapter, we studied the performance of a potential mixed spatial resolution PET system with its high resolution region located at one end of its axial extent. We compared this system to two other related PET systems: a high resolution system equivalent to the high resolution detector region of the mixed resolution scanner, and a standard resolution scanner with the same size but utilizing larger individual detector elements. We examined how the mixed resolution system navigated the tradeoffs between sensitivity and spatial resolution by attempting to sacrifice neither in order to retain overall image quality. In all three studies, the mixed resolution system showed advantages over at least one of the other two systems considered. The mixed resolution scanner had substantially better sensitivity

compared to the high resolution system, and it showed improved spatial resolution performance compared to the standard resolution system at most locations tested. The mixed resolution system showed improved ability to recover regions of the NEMA image quality phantom compared to the standard resolution system and approached the performance of the high resolution system. Altogether, we showed that the mixed resolution concept with an end-located high resolution region is a potentially feasible method of incorporating high resolution performance in a region of a larger scanner.

While the mixed resolution system did show potential advantages, further improvements to the image-space modeling in reconstruction could likely further improve the overall performance of such a system. Moreover, further studies examining the contrast recovery and lesion detectability performance of the mixed resolution system could provide a more concrete sense of the potential improvements one might see by adopting such a system.

CHAPTER 6
INITIAL DEVELOPMENT OF AN EVALUATION MIXED RESOLUTION SYSTEM USING A TRANSFORMABLE GANTRY

In the previous chapters of this work, we have utilized realistic simulations of mixed spatial resolution PET systems using Monte Carlo methods implemented in the Geant4 Application for Tomographic Emission (GATE). These studies have shown the benefits in terms sensitivity, spatial resolution, and contrast recovery performance of incorporating high resolution detectors enclosing a subvolume of the axial FOV. The simulations used in these studies incorporated the physical effects involved in detection such as scintillation crystal efficiency, crystal penetration, and energy resolution, as well as a model of a simple digital readout electronics. However, even the best results achieved *in situ* require real-world validation. Therefore, in order to further validate the mixed resolution PET system concept experimentally, we have initiated the development of an evaluation mixed resolution PET system. The system configuration, as well as some initial results using only the high resolution detector modules, are presented in the following sections.

6.1 System Configuration

While the previous chapters evaluated systems using a twelve-detector-module, cylindrical geometry, for the evaluation system under development, a box-like geometry was chosen. A mock-up of the system generated using GATE is shown in Figure 6.1. Four detector heads, each consisting of a high resolution detector module sandwiched between two lower resolution detector modules, are placed in two opposed pairs. Apart from differences between box-like cylindrical detector orientations, this is a similar approach compared to the system evaluated in Chapter 4. The total length of the system is 10 cm, with a transverse FOV of 5×5 cm^2.

The high resolution region comprises the central 5 cm of the system in the axial direction, with the lower resolution modules each adding 2.5 cm to the axial FOV on each end. This geometry is motivated in part by the availability of modular detectors which are designed to be easily configurable for incorporation into a variety of different potential PET systems. Moreover, the system is implemented on a transformable gantry, which can mechanically change the location of the detector modules to make the most use of the flexible modular detector design for different imaging tasks. While we evaluate the geometry described above for our mixed resolution concept, the system allows other potential geometries to be explored. We now go on to describe further details of these detector modules, the data acquisition software, and the system gantry.

6.1.1 Detector Modules

As mentioned above, the system under development would utilize modular detectors designed for easy adaptation to different PET systems. This type of module aspires to the "plug-and-play" input/output simplicity of modern consumer electronics. Such modules function with a single connector for power and data readout occurring over a gigabit Ethernet cable, which is significantly fewer connectors than is typically required for PET detector readout.

The detector modules used as the high resolution modules were the PSPMT-based basic detector modules (BDM) introduced in [123] and used in the Trans-PET BioCaliburn LH system manufactured by Raycan Technology Co., Ltd. [116]. Each BDM consists of four LSO crystal arrays, arranged 2×2, with 13×13 crystals that are 1.89×1.89×13.00 mm^3 in size with a 2.03×2.03 mm^3 pitch. The total sensitive area of each BDM is approximately 5×5 cm^2. Each detector uses an onboard digital readout system using the multi-voltage threshold (MVT) method, which has been shown to accurately characterize the PET signal waveform by sampling with respect to a user-defined set of reference amplitudes [123]. The BDMs have a theoretical intrinsic resolution of 1.0 mm, which is just above half the crystal

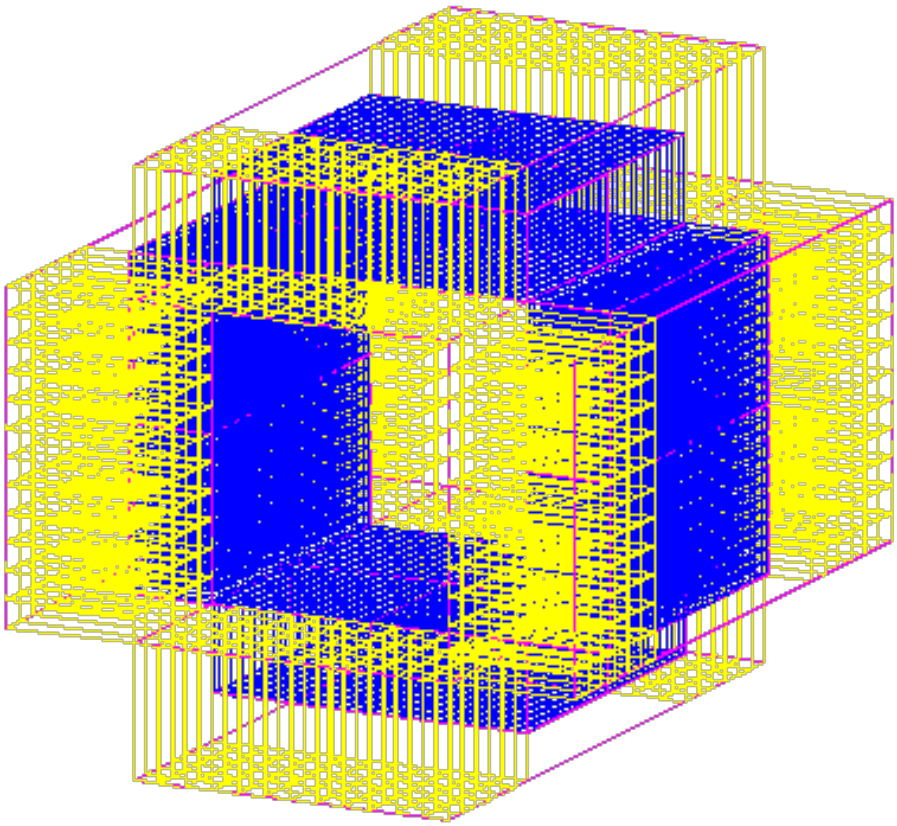

Figure 6.1: Proposed geometry of the mixed resolution validation system presently under development. High resolution detector modules are depicted in blue and standard resolution modules are depicted in yellow.

pitch. The previously reported energy resolution and timing resolution are 13% and 1.5 ns, respectively. An example module is shown in Figure 6.2A.

The detector modules utilized for the standard resolution regions of the system are based on the silicon photomultiplier (SiPM) detector modules reported in Xi *et al.* [121] and now produced by Raycan Technology Co., Ltd. These detectors are composed of LSO crystal arrays, with 6×6 crystals coupled one-to-one with SensL FM30035 SiPM. In the array, each SiPM pixel has a 3.0×3.0 mm^2 active area with a 4.2×4.2 mm^2 pitch. The LYSO matrix consists of 3.95×3.95×20 mm^3 crystals with a 0.3 mm gap. Each detector has a sensitive area of 2.5×2.5 cm^2. The onboard digital readout, which is based on field programmable

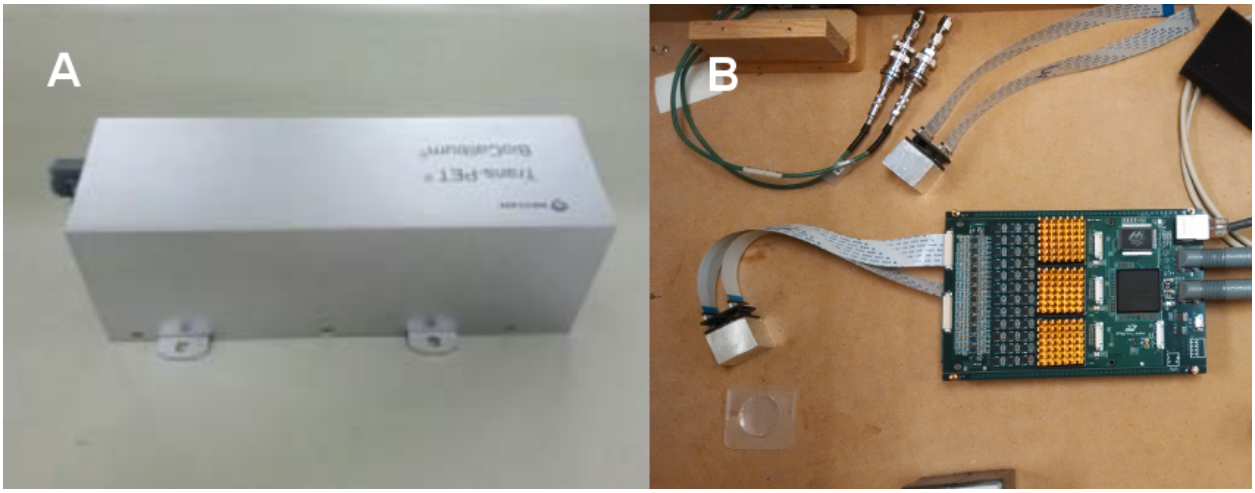

Figure 6.2: (A) The high resolution detector modules utilizing PSPMTs with 1.0 mm intrinsic resolution. (B) Detector technology used in the standard resolution detector modules. A 6×6 array of 2 cm thick LSO crystal is coupled one-to-one to an array of SiPMs and connected via a ribbon cable to the readout board. The readout board's digital processing unit utilizing several FPGA chips samples the waveform and generates singles event data which is read out via a gigabit Ethernet cable.

gate array (FPGA) technology to keep the system compact, also uses the MVT method as described above. Reported energy and timing resolution are 15.1% and 684 ps, respectively. An image of the interior electronics and detectors for a module using this technology is shown in Figure 6.2B.

For both the high and standard resolution detectors, events are initially processed online using the FPGAs mentioned to yield a a sparse timing and energy sampling of the waveform for each detected event. This singles event data is read out over a gigabit Ethernet cable for further processing and coincidence detection performed offline. All that is required for acquiring data from the full set of detector modules is a gigabit Ethernet switch, a piece of hardware to synchronize the clocks of each detector module to enable later coincidence sorting, and a computer with a gigabit Ethernet port.

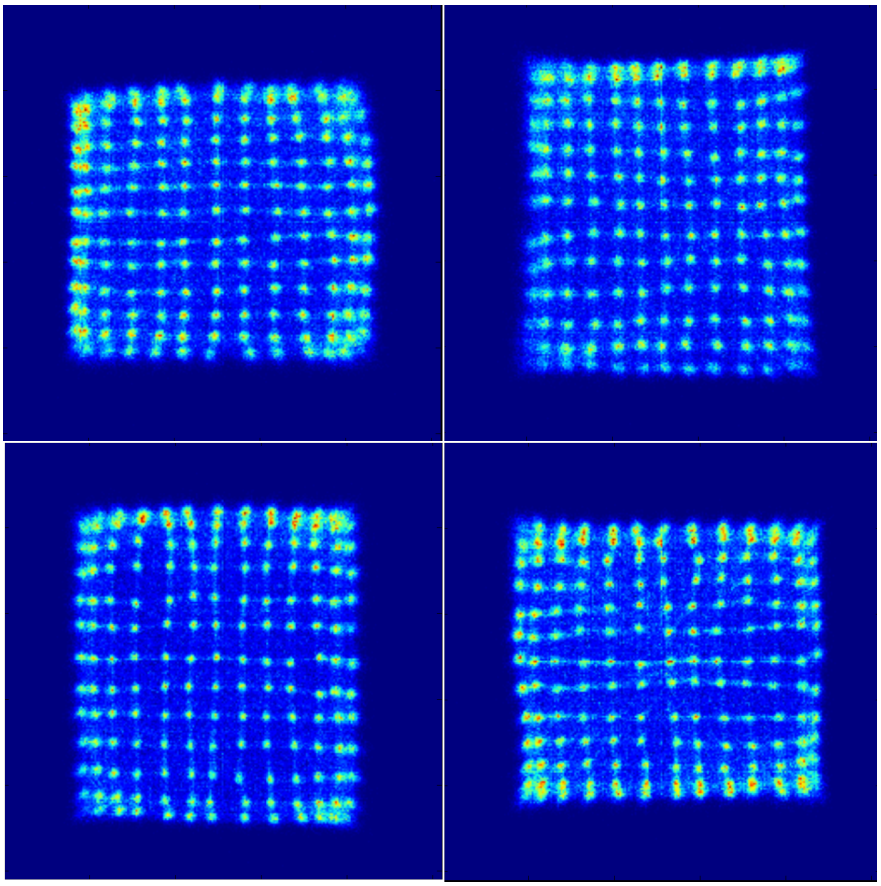

Figure 6.3: Flood images acquired by the four PSPMTs of a single high resolution detector and used to generate a look-up table for crystal identification during coincidence processing.

6.1.2 Data Acquisition Software

A data acquisition software program was developed utilizing the Scientific Python Development Environment (Spyder), an open source cross-platform integrated development environment. The software included a methods for simultaneously reading in the data from multiple detector modules over a single gigabit Ethernet input. The stream of singles data from each detector module was collected in this manner and stored in separate list mode files for each module for later processing. Because the high resolution modules use PSPMTs, event locations read out by the module's digital processing unit must be associated to a specific crystal after readout. Manual and automatic segmentation methods for acquiring and storing this position calibration, as well as an energy calibration for each module, were

developed. This method was made easy for the end-user because correct crystal identification plays a significant role in the system's performance and can potentially drift from previous calibrations with temperature shifts and frequent use of the system. An example flood image used to generate the crystal identifications for one of the high resolution modules is shown in Figure 6.3. At the edges, and especially at the corners, of each PSPMT, identifying the crystal location is challenging and mis-identification for these crystals is likely to lead to some loss of resolution performance. This crystal identification look-up-table was then used in the coincidence sorting algorithm.

Because of the memory requirement for processing the singles list-mode data, which could be on the order of several gigabytes per detector for typical small animal scanning parameters, the coincidence sorting method utilized an event buffer in order to avoid keeping all the event data in memory at the same time. The method initially scans for the location of the latest "first" event according to the synchronized detector clock among the different detector modules. Events from all modules occurring after this point are then read into the buffer in time order until it is full, at which point the event list is examined for potential coincidence events utilizing user-defined energy and coincidence windows. The first event in the list is then removed, a new event is added to the end, and the new first event is again evaluated against the rest of the buffer for coincidence events. This process occurs until all the data enters the buffer. Buffer size must be chosen such that enough events are available for comparison that no coincidence events are ignored, but not so large as to cause memory usage issues for the computer on which the data acquisition software is used.

A graphical user interface (GUI) was developed to allow for straightforward manipulation of the methods described above and for user monitoring of the data acquisition process, which is shown in Figure 6.4. The GUI provides a series of form fill and drop-down menus for users to enter important acquisition parameters like subject and study name, radioisotope, and activity to be associated with the acquired data. Different preset energy windows are

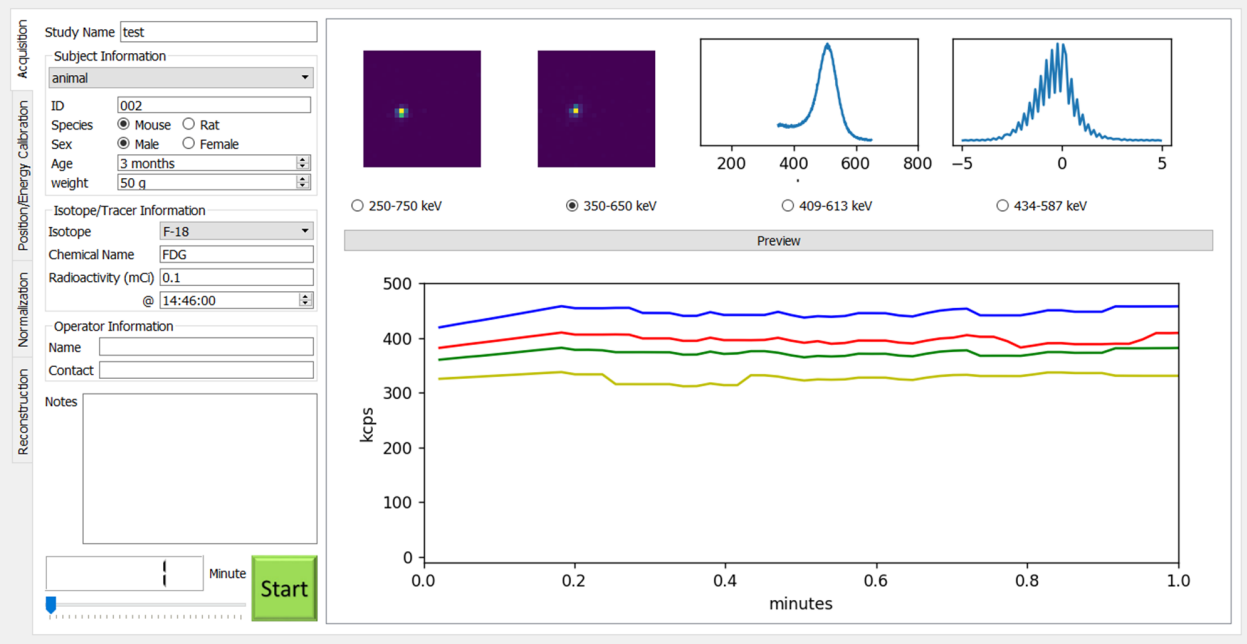

Figure 6.4: The graphical user interface (GUI) developed for data acquisition of the evaluation system. The GUI provides users with straightforward tools to calibrate and acquire data from the evaluation system, as well as useful visualization methods from which to judge performance, including a 2D scout image of the activity distribution and count rate performance curves for each detector module updated in real time.

provided as options. The option of acquiring a two-dimensional scout image generated from a 10 second acquisition by projecting coincidence events between opposing detectors onto a centrally-located plane between them is offered to the user to ensure source placement is appropriate before beginning a longer acquisition. Energy and timing resolution performance are also shown for the scout image data to ensure functionality. After setting the acquisition time and selecting the start button, the count rate performance curve for each detector module is presented and updated in real time to ensure continuing performance during an acquisition.

Another tab available in the GUI allows the user to perform the calibrations of the crystal location and energy mentioned previously or to select saved calibrations acquired previously. Tabs for normalization and image reconstruction are also implemented. However, the underlying methods remain under development.

Figure 6.5: The transformable gantry utilized for the mixed resolution evaluation system. Four locations that can provide detector modules with independent motion are found on the accordion-like structures between the two large ring-shaped support structures. Detector modules can be moved radially and axially and can be rotated to form box-like geometries with detectors at 90 degree angles, geometries of two opposed banks of detector modules, or geometries using intermediate angles.

6.1.3 Transformable Gantry

To make use of the flexibility offered by the modular detector design utilized for this evaluation system, a transformable gantry was developed in conjunction with collaborators at the Huazhong University of Science and Technology in order to enable the reorientation of the detector modules for different imaging tasks. The idea of a flexible gantry has been been shown previously to have potential for making PET imaging more adaptable [122, 115, 128], which matched well with our desire to study different mixed resolution geometries.

The gantry, which is shown in Figure 6.5, consists of two large ring support structures which are capable of motion in the axial direction, increasing or decreasing the axial FOV.

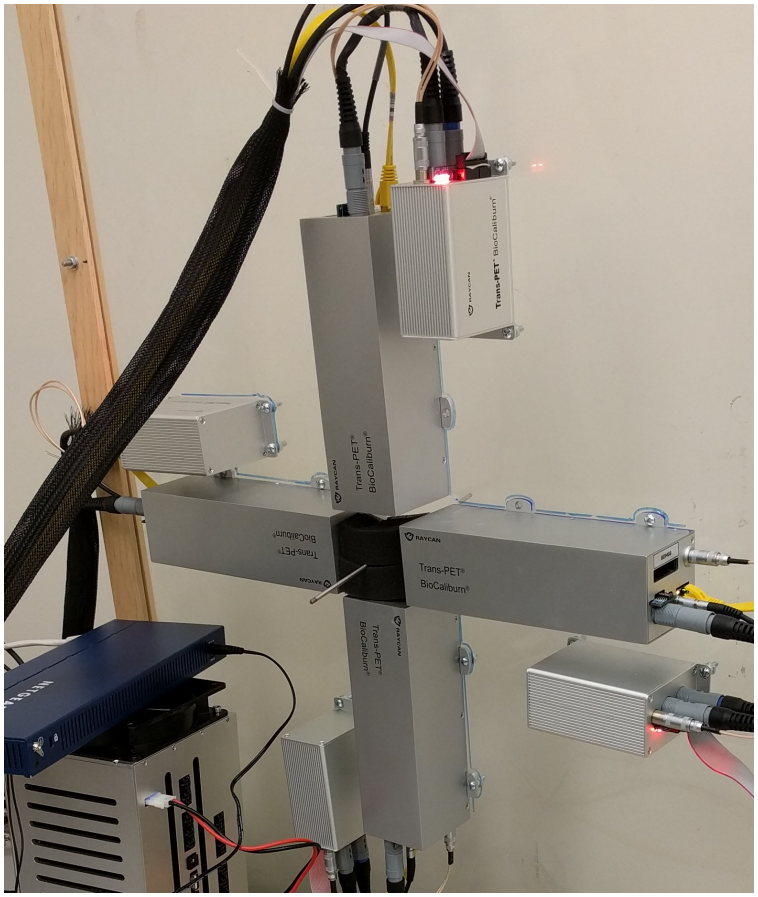

Figure 6.6: The initial improvised gantry used for characterization studies of the data acquisition software and high resolution detector modules.

Two different support structures between these two rings hold the detector modules and allow for four independent, movable locations (two per support structure) upon which to attach detectors. These structures can move radially inward and outward to increase or decrease the imaging FOV. The two detector locations on each structure can also fold such that attached detectors can be oriented at a 90 degree angle from each other, operate side-by-side as a single panel, or orientated at any intermediate angle. A movable platform allows for translation of the imaging subject axially and vertically within the FOV. The motion capability is controlled by a computer tablet or via software on the data acquisition computer.

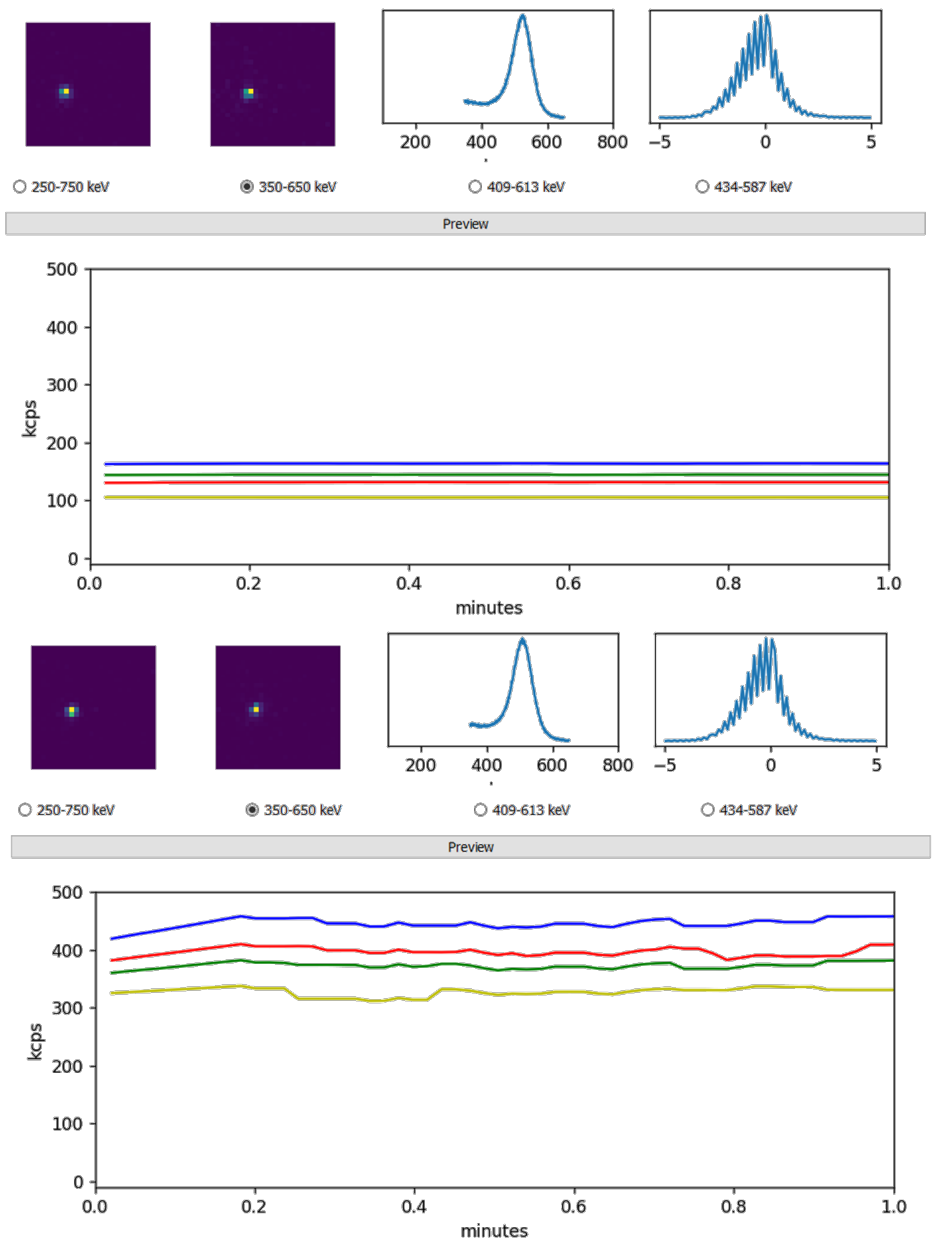

Figure 6.7: Two-dimensional scout images and count rate performance curves for two point source acquisitions testing the data acquisition software, using a 30 μCi (top) and 100 μCi (bottom) point source, respectively.

6.2 Initial Characterization of High Resolution Modules

Prior to acquisition of the transformable gantry and standard resolution detectors, initial tests of the high resolution modules in the proposed box-like geometry were conducted using

an improvised gantry constructed from plastic materials to which the detector modules were attached (Figure 6.6). Initial studies acquiring data from a ^{22}Na point source were performed to test the data acquisition software and examine module performance.

Figure 6.7 shows the 2D projections and count rate performance curves for two point source acquisitions, one for a 30 μCi and one for a 100 μCi ^{22}Na point source using a one minute acquisition time. The point source is clearly visualized in the 2D projection images for both acquisitions. While the count rate is relatively steady for the 30 μCi point source, there are wobbles in the 100 μCi curve. These wobbles are believed to be the result of memory usage issues on the data acquisition computer as the data is acquired from the Ethernet connection and indicate an upper range of activity usable for the current data acquisition implementation for a point source.

The modules were then mounted on the transformable gantry, and initial studies imaging mice using an ^{18}F-based radiotracer were performed in order to test the detector modules and data acquisition software on the gantry. Because image reconstruction methods were not yet implemented for this system, a preliminary qualitative characterization of the potential image performance of the system using the 2D projection images was also performed.

The 2D projection images and detector count rate performance curves for several mouse studies are shown in Figure 6.8. All acquisitions were performed following protocols approved by a Institutional Animal Care and Use Committee (IACUC). The first acquisition (top in the figure) was performed for a mouse receiving an intraperitoneal injection of 30 μCi and imaged for 30 minutes immediately post-injection. The projection image on the left shows a horizontal image of the mouse with its head oriented to the left, and a region of high activity, believed to be the site of the injection in its lower abdomen. The projection on the right shows a top-down view of the mouse. The count rate performance curves for this acquisition were relatively smooth with some minor dips which are believed to be related to computer memory usage issues as touched upon previously. Current solutions to this problem include

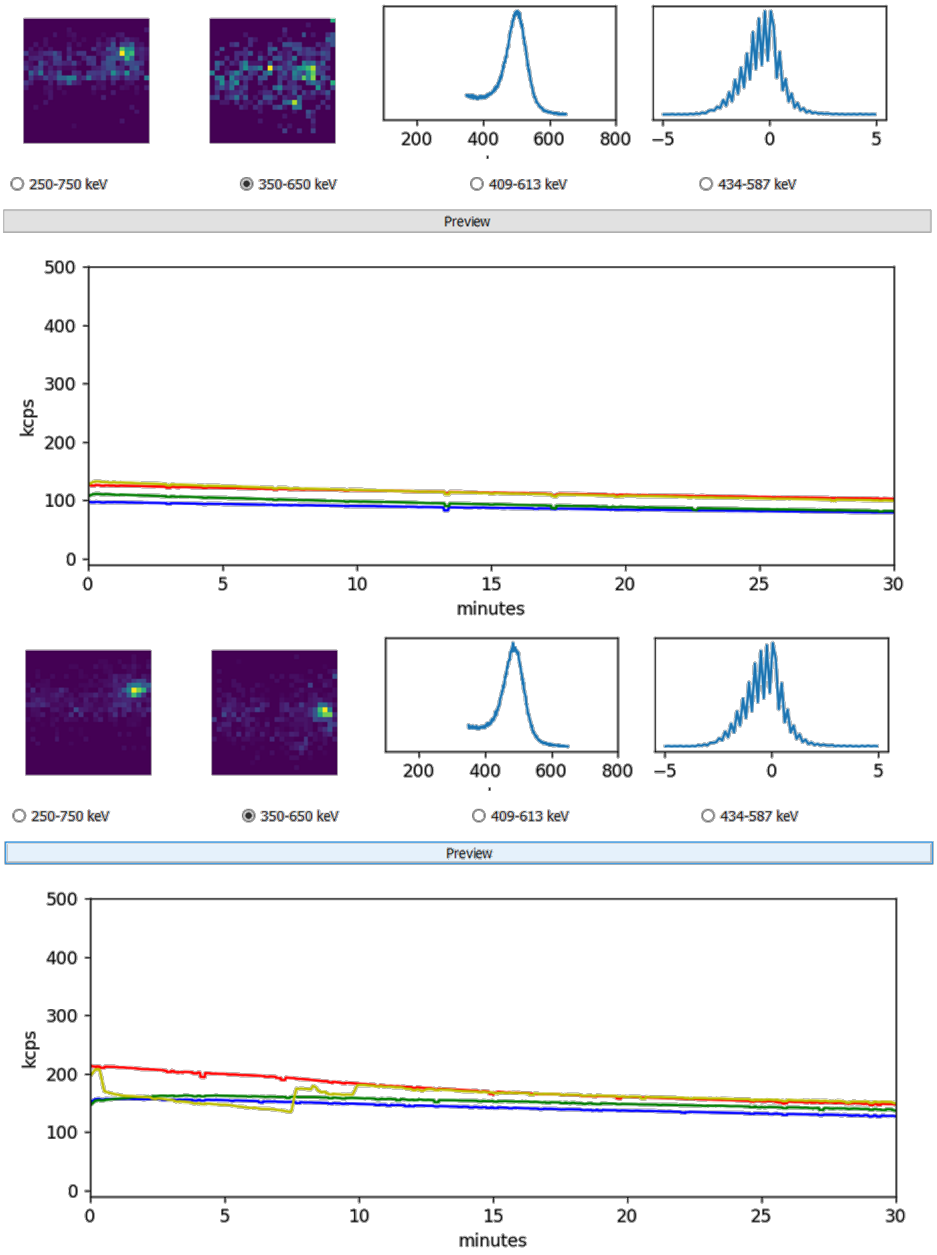

Figure 6.8: Two-dimensional scout images and count rate performance curves for two consecutive 30-minute acquisitions of an ^{18}F-based radiotracer performed on a mouse injected with 30 μCi. The initial study is shown at top and the second study performed immediately after is shown at bottom. Two-dimensional scout projection images are shown from 10 second acquisitions at the beginning of each 30 minute study. Energy and timing resolution performance are shown immediately to the right of the projections, respectively. Detector module count-rate performance is shown at bottom for each acquisition.

turning off all extraneous background software on the data acquisition computer. However, other solutions to improve the software and avoid these problems are under investigation.

The second acquisition was performed using the same mouse and acquired immediately after the first acquisition was completed. One notices the expected reduction in intensity in the projection images as compared to the first acquisition. A sudden drop is also noticed in the count rate of one of the detector modules. The loss of performance was the result of heating in the detector when a heat lamp used to warm the mouse during the acquisition was moved too close to the scanner, demonstrating that performance loss due to detector temperature sensitivity may require attention in the continued evaluation of the system.

Projection images generated over the first thirty minute acquisition are shown in Figure 6.9 superimposed over a maximum intensity projection of a corresponding CT image of the mouse. Projections of data from minutes 0-10, 10-20, 20-30 and for the entire 30 minute acquisition show the progression of the radiotracer after initial injection, further characterized in the time-activity-curve, which shows intensity values for regions of interest in projections reconstructed from data in 1 minute frames. These initial results demonstrate the functionality of the acquisition software and scanner configuration.

Altogether these studies show that the detector modules are working as expected and that the data acquisition software performs adequately when utilized in the preclinical setting, though care should be taken regarding detector heating to avoid performance effects. Initial projection images reconstructed from the data show the potential image performance of the system. More work must be performed to remove computer memory usage effects from reducing count rate performance.

6.3 Summary

Initial characterizations of the high resolution detector region of a mixed resolution PET system built on a transformable gantry have been completed. This work also involved the

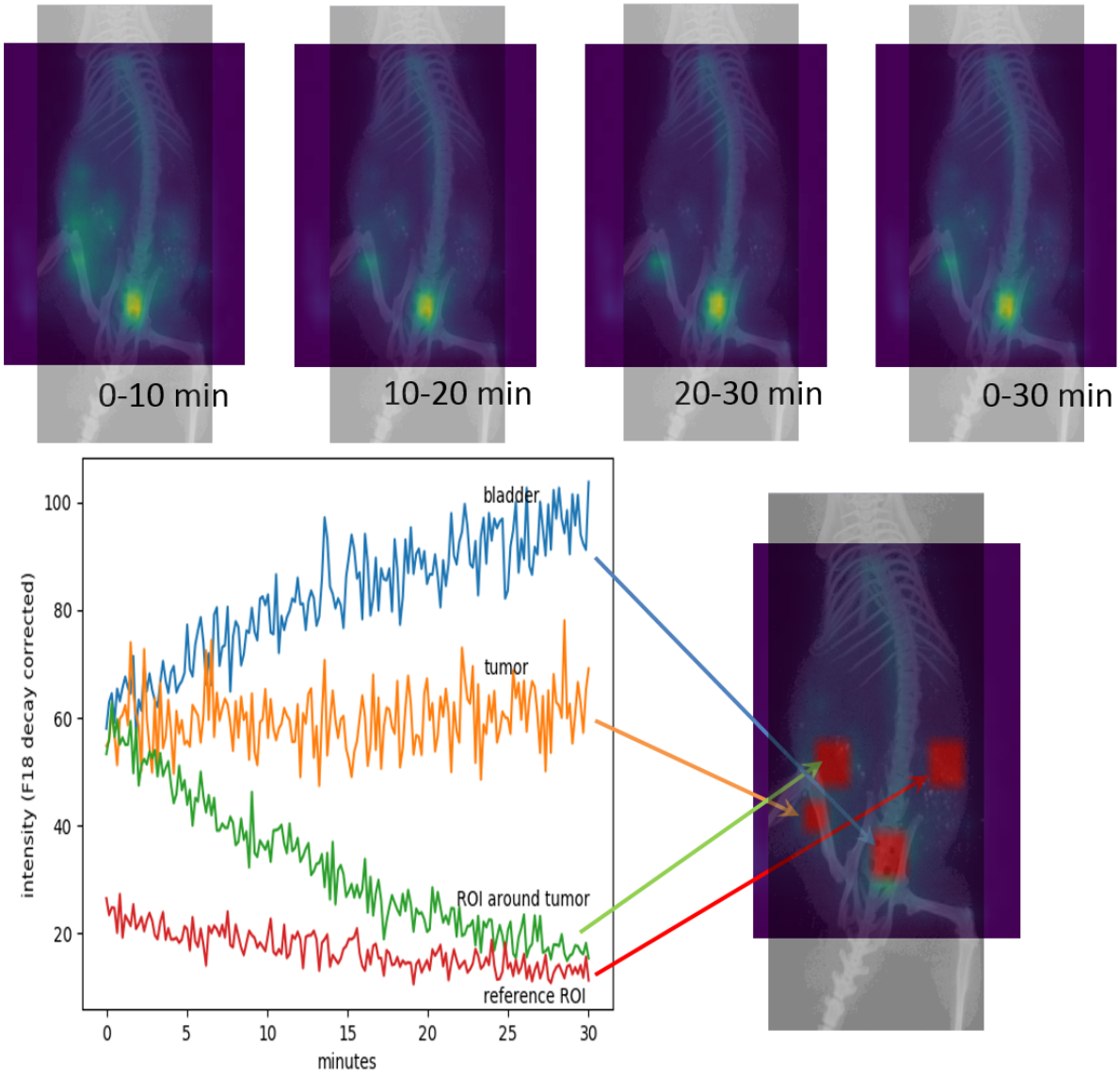

Figure 6.9: Projection images of PET data acquired from an ^{18}F acquisition of a mouse overlayed atop a maximum intensity projection of a corresonding CT. Projections are shown for 10 minute increments of the 30 minute scan as well as the complete 30 minute acquisition. Time activity curves generated using 1 minute frames of the acquisition are shown for several regions of interest, including a tumor and the bladder.

development and characterization of data acquisition software tools. The modules showed the expected time and energy resolution performance, and initial projection image results for point sources and ^{18}F mouse studies were promising. Improvements to the data acquisition software to avoid memory usage issues during acquisition may be needed for future use. The

detector modules were found to be sensitive to heating from lamps used in the preclinical imaging setting, which reduced the count rate of affected detector modules. The development of image reconstruction tools is ongoing, as are further comprehensive validation studies of the high resolution system's performance. Further evaluation of the transformable gantry motion capabilities and inclusion of the standard resolution detector modules in order to fully evaluate the mixed resolution concept are also left for future work.

CHAPTER 7

CONCLUSIONS

7.1 Summary

In this dissertation work, we have studied the feasibility of the development of mixed spatial resolution PET systems that incorporate detectors of different intrinsic spatial resolution performance at different axial locations of what is otherwise a typical cylindrical PET system. Improving spatial resolution performance is a major challenge in current PET research due to both fundamental and engineering-derived limitations. The general approach has been to try to develop modules with increasingly smaller individual detector elements and improved timing performance, which are more expensive to build. Meanwhile, clinical PET systems have seen only incremental improvement in the last decade, primarily due to engineering and financial constraints just mentioned. The cost of taking an existing scanner geometry and replacing all of its detector modules with higher spatial resolution detectors is considerable. This is due to the significant increase in the total number of detector elements and the hardware required to read out data accurately and in a reasonable time without losing events to system dead time.

As discussed in Chapter 2, a compromise investigated by other groups has been to incorporate high resolution detector module inserts within an existing standard resolution detector system, creating a sub-volume of high resolution performance within the larger FOV. This approach has shown some promise improving spatial resolution performance and does not sacrifice sensitivity in order to incorporate higher resolution performance. However, it has drawbacks regarding the reduction in size of the axial FOV caused by introducing an insert detector module and also potential pitfalls in combining a detector insert readout electronics with those of an existing scanner and optimizing the location of the insert for each imaging task or study. The purpose of proposing our scanner geometry followed a similar desire to

incorporate higher spatial resolution performance in a sub-volume of a larger FOV. However, our configuration does so without an insert device or reduction of the transverse FOV. Instead, the high resolution modules replace standard resolution modules in the existing scanner geometry.

In order to examine the feasibility of our concept scanner to improve spatial resolution and other image quality performance metrics, system design and evaluation tools had to be developed. System simulations were performed using the GATE Monte Carlo software environment, which accurately modeled the physical processes of PET detection. A ray-tracing projection method [100] was chosen due to its flexibility in the face of the varying scanner configurations utilized in this study. This approach was paired with a direct normalization method, with normalization factors measured using simulated data from GATE. An image-space resolution model was utilized to account for the varying intrinsic resolution properties of the mixed resolution data. A simple uniform-per-slice Gaussian blur derived from measurement of the point spread function of reconstructed data at each slice was used in the model. While not a completely accurate model of resolution over the entire FOV, as described in Chapter 3, the complete reconstruction algorithm showed improved handling of the mixed resolution data compared to the algorithm employing only ray-tracing and was deemed adequate for use in further evaluation of the feasibility of mixed resolution systems.

Two different mixed resolution scanner configurations were evaluated in this work for their ability to provide improved image quality performance compared to equivalent systems with lower intrinsic resolution. The first, incorporating a high resolution detector region axially in-between two standard resolution regions, was examined in Chapter 4. The second, incorporating the high resolution detector region at one axial end of the scanner, was examined in Chapter 5. These systems were compared to a standard resolution system with what was otherwise exactly the same geometry except the larger detector elements. They were also compared to a high resolution system with dimensions equivalent to the high reso-

lution region of each respective mixed resolution scanner in order to to examine the benefits of higher sensitivity for the mixed resolution system. For both cases, the mixed resolution scanners demonstrated superior sensitivity compared to the high resolution scanners over their entire FOV. This result emphasized the benefit of not sacrificing axial FOV in the interest of incorporating higher resolution detector modules in ones scanner.

Both mixed resolution scanners showed spatial resolution performance within the high resolution detector regions that was superior to the standard resolution scanner and approaching that of the high resolution scanner. Other locations in the FOV demonstrated less benefit from the mixed resolution data, which can be explained by potential inadequacies of our per-slice resolution modeling method. However, there was still a general trend of the mixed resolution scanners providing a resolution performance advantage. Studies of contrast recovery and noise performance also showed the mixed resolution system had advantages over standard resolution systems. Altogether, these studies demonstrated that mixed resolution systems have potential in providing improved spatial resolution performance compared to standard resolution systems.

Initial work was conducted in the development of a mixed resolution evaluation system on a transformable gantry. Data acquisition software was developed, and the basic performance of the high resolution detector modules was demonstrated on a rough initial gantry and on the transformable gantry. However, significant work remains before real data validation of the mixed resolution concept can be performed with this system.

In summary, the major contributions of this work are as follows:

(1) We have developed and validated iterative 3D reconstruction methods to account for the mixed resolution data for our newly proposed mixed resolution scanner configurations. Though others have proposed methods for mixed resolution reconstruction, they were envisioned for use with high resolution detector insert systems and modeled resolution in the projection space. The method developed here demonstrated the utility of using an image-

based spatial resolution model for this application and showed their potential use in further evaluation of variations of our proposed mixed resolution geometry.

(2) For a mixed resolution system geometry with a centrally-located high resolution region, we have shown the benefits to resolution and contrast recovery performance compared to a system with similar geometry but lower intrinsic resolution performance. We have also shown improved sensitivity and noise characteristics of this mixed resolution system compared to a high resolution system equivalent in geometry to the central high resolution region of the mixed resolution scanner.

(3) We have shown the feasibility of a mixed resolution system with a region of high resolution detector modules located at one axial end of the system. This alternative scanner arrangement demonstrated spatial resolution advantages over an equivalently sized scanner with a lower spatial resolution. It also demonstrated a higher sensitivity and improved noise performance compared to to a high resolution scanner equal in size to the high resolution detector region of the mixed resolution scanner.

(4) We have laid the groundwork for the development of an evaluation mixed resolution system, developing data acquisition software and performing tests of the high resolution detector portion of the system. This work can be developed further to create the full system for real data validation of the mixed resolution concept.

7.2 Suggestions for Future Research

In this work, we modeled the spatial resolution of our mixed resolution system using a uniform Gaussian blurring function specific to each slice and derived from the measured resolution performance at the center of that slice. This model can be further improved by modeling the resolution in all three directions separately since they are likely to vary differently across the field of view of a mixed resolution system. Moreover, a resolution model that varies in the transverse plane as well as the axial plane as currently implemented would better account

for the radial elongation seen in at larger distances from the center of each slice and improve overall resolution performance. A full voxel-by-voxel model of the point response for the entire image volume would bring the most improvement but requires a substantial time and computational resources for simulation and reconstruction to measure the point responses accurately.

The reconstruction algorithm in this work relied on a ray-tracing projection method sped up by utilizing CPU multithreading, which led to MLEM iterations that required approximately 25 to 28 minutes to run on multi-core, high performance desktop computers. Further speed-up of this algorithm by parallelization using GPUs might provide further speed up and make future evaluation of the imaging systems under consideration more feasible. Moreover, the development of an ordered-subsets expectation-maximization algorithm could provide additional speed-up to algorithm convergence for conducting studies of interest using this algorithm.

While simulations of mixed resolution systems in GATE are a good benchmark for the feasibility of such systems, it is desirable to verify our methods using an actual physical validation system. We present some of the initial studies for the high resolution section of such a system in Chapter 6, which is mounted on a transformable gantry. Further work remains in developing and validating reconstruction methods for the system and incorporating these into the data acquisition software. Studies characterizing the motion capabilities of the gantry also remain to be performed. Finally, the characterization of the standard resolution modules and their addition to the gantry and incorporation into the existing data acquisition architecture remains to be performed. These works will allow for further evaluation of our mixed resolution concept using real data.

APPENDIX A

AN EXAMPLE GATE MACRO FILE

Below is an example macro file used to generate simulations in GATE. This example is used to simulate the voxelized 4 line source phantom for the mixed resolution scanner system evaluated in Chapter 4

```
## List of materials and their properties to be used in the simulation.
/gate/geometry/setMaterialDatabase GateMaterials.db

## Parameters to define the simulation environment and PET scanner
/gate/world/geometry/setXLength 20.0 cm
/gate/world/geometry/setYLength 20.0 cm
/gate/world/geometry/setZLength 60.0 cm
/gate/world/setMaterial Air
/gate/world/vis/setVisible false

/gate/world/daughters/name PETscanner
/gate/world/daughters/insert trpd
/gate/PETscanner/placement/setTranslation 0.0 0.0 0.0 cm
/gate/PETscanner/geometry/setX1Length 10.0 cm
/gate/PETscanner/geometry/setY1Length 10.0 cm
/gate/PETscanner/geometry/setX2Length 10.0 cm
/gate/PETscanner/geometry/setY2Length 10.0 cm
/gate/PETscanner/geometry/setZLength 40.0 cm
/gate/PETscanner/geometry/setXBoxLength 4.0 cm
/gate/PETscanner/geometry/setYBoxLength 4.0 cm
```

```
/gate/PETscanner/geometry/setZBoxLength 40.0 cm
/gate/PETscanner/geometry/setXBoxPos 0.0 cm
/gate/PETscanner/geometry/setYBoxPos 0.0 cm
/gate/PETscanner/geometry/setZBoxPos 0.0 cm
/gate/PETscanner/setMaterial Air
/gate/PETscanner/vis/setColor red
/gate/PETscanner/vis/forceWireframe
/gate/PETscanner/vis/setVisible false

/gate/PETscanner/daughters/name head1
/gate/PETscanner/daughters/insert box
/gate/head1/placement/setTranslation 0. 3.4856 0.0 cm
/gate/head1/geometry/setXLength 1.6 cm
/gate/head1/geometry/setYLength 1.0 cm
/gate/head1/geometry/setZLength 7.2 cm
/gate/head1/setMaterial Water
/gate/head1/vis/setColor magenta
/gate/head1/vis/forceWireframe
/gate/head1/vis/setVisible true

/gate/head1/daughters/name module1
/gate/head1/daughters/insert box
/gate/module1/placement/setTranslation 0. 0. 1.8 cm
/gate/module1/geometry/setXLength 1.6 cm
/gate/module1/geometry/setYLength 1.0 cm
/gate/module1/geometry/setZLength 3.6 cm
```

```
/gate/module1/setMaterial Water
/gate/module1/vis/setColor magenta
/gate/module1/vis/forceWireframe
/gate/module1/vis/setVisible false

/gate/module1/daughters/name crystal1
/gate/module1/daughters/insert box
/gate/crystal1/placement/setTranslation 0. 0. 0. cm
/gate/crystal1/geometry/setXLength 0.20 cm
/gate/crystal1/geometry/setYLength 1.0 cm
/gate/crystal1/geometry/setZLength 0.20 cm
/gate/crystal1/setMaterial LSO
/gate/crystal1/vis/setColor blue
/gate/crystal1/vis/forceWireframe
/gate/crystal1/vis/setVisible true

/gate/crystal1/repeaters/insert cubicArray
/gate/crystal1/cubicArray/setRepeatNumberX 8
/gate/crystal1/cubicArray/setRepeatNumberY 1
/gate/crystal1/cubicArray/setRepeatNumberZ 18
/gate/crystal1/cubicArray/setRepeatVector 0.20 0.0 0.20 cm

/gate/module1/repeaters/insert cubicArray
/gate/module1/cubicArray/setRepeatNumberX 1
/gate/module1/cubicArray/setRepeatNumberY 1
/gate/module1/cubicArray/setRepeatNumberZ 1
```

```
/gate/module1/cubicArray/setRepeatVector 0.0 0.0 0.0 cm

/gate/head1/daughters/name module2
/gate/head1/daughters/insert box
/gate/module2/placement/setTranslation 0. 0. -1.8 cm
/gate/module2/geometry/setXLength 1.6 cm
/gate/module2/geometry/setYLength 1.0 cm
/gate/module2/geometry/setZLength 3.6 cm
/gate/module2/setMaterial Water
/gate/module2/vis/setColor magenta
/gate/module2/vis/forceWireframe
/gate/module2/vis/setVisible false

/gate/module2/daughters/name crystal2
/gate/module2/daughters/insert box
/gate/crystal2/placement/setTranslation 0. 0. 0. cm
/gate/crystal2/geometry/setXLength 0.40 cm
/gate/crystal2/geometry/setYLength 1.0 cm
/gate/crystal2/geometry/setZLength 0.40 cm
/gate/crystal2/setMaterial LSO
/gate/crystal2/vis/setColor yellow
/gate/crystal2/vis/forceWireframe
/gate/crystal2/vis/setVisible true

/gate/crystal2/repeaters/insert cubicArray
/gate/crystal2/cubicArray/setRepeatNumberX 4
```

```
/gate/crystal2/cubicArray/setRepeatNumberY 1
/gate/crystal2/cubicArray/setRepeatNumberZ 9
/gate/crystal2/cubicArray/setRepeatVector 0.4 0.0 0.4 cm

/gate/module2/repeaters/insert cubicArray
/gate/module2/cubicArray/setRepeatNumberX 1
/gate/module2/cubicArray/setRepeatNumberY 1
/gate/module2/cubicArray/setRepeatNumberZ 1
/gate/module2/cubicArray/setRepeatVector 0.0 0.0 0.0 cm

/gate/head1/repeaters/insert ring
/gate/head1/ring/setRepeatNumber   12

/gate/systems/PETscanner/level1/attach head1
/gate/systems/PETscanner/level2/attach module1
/gate/systems/PETscanner/level3/attach crystal1
/gate/systems/PETscanner/level2/attach module2
/gate/systems/PETscanner/level3/attach crystal2

/gate/crystal1/attachCrystalSD
/gate/crystal2/attachCrystalSD

/gate/systems/PETscanner/describe
/gate/geometry/rebuild
```

```
## Parameters specifying the physics to be simulated
/gate/physics/addProcess PhotoElectric
/gate/physics/processes/PhotoElectric/setModel StandardModel
/gate/physics/addProcess Compton
/gate/physics/processes/Compton/setModel StandardModel
/gate/physics/addProcess RayleighScattering
/gate/physics/processes/RayleighScattering/setModel PenelopeModel
/gate/physics/addProcess ElectronIonisation
/gate/physics/processes/ElectronIonisation/setModel StandardModel e-
/gate/physics/processes/ElectronIonisation/setModel StandardModel e+
/gate/physics/addProcess Bremsstrahlung
/gate/physics/processes/Bremsstrahlung/setModel StandardModel e-
/gate/physics/processes/Bremsstrahlung/setModel StandardModel e+
/gate/physics/addProcess PositronAnnihilation
/gate/physics/addProcess MultipleScattering e+
/gate/physics/addProcess MultipleScattering e-
/gate/physics/addProcess Decay
/gate/physics/addProcess RadioactiveDecay
/gate/physics/setEMin 0.1 keV
/gate/physics/setEMax 10 GeV
/gate/physics/setDEDXBinning 220
/gate/physics/setLambdaBinning 220


## Parameters defining the activity distribution
/gate/source/addSource dzo voxel
```

```
/gate/source/dzo/reader/insert interfile
/gate/source/dzo/interfileReader/translator/insert range
/gate/source/dzo/interfileReader/rangeTranslator/readTable
act-4LineSrc_DodecaPET_img93x93x139.txt
/gate/source/dzo/interfileReader/rangeTranslator/describe 1
/gate/source/dzo/interfileReader/readFile
4LineSrc_DodecaPET_img93x93x139.h33
/gate/source/dzo/interfileReader/verbose 1
/gate/source/dzo/setType backtoback
/gate/source/dzo/setAccolinearityFlag 0   #added from pointsrc.mac
/gate/source/dzo/setAccoValue 0.0 deg     #added from pointsrc.mac
/gate/source/dzo/gps/particle gamma
/gate/source/dzo/gps/energytype Mono
/gate/source/dzo/gps/monoenergy 0.511 MeV
/gate/source/dzo/gps/angtype iso
/gate/source/dzo/gps/confine NULL
/gate/source/dzo/setPosition  -2.4 -2.4 -3.6 cm
/gate/source/dzo/dump 1

## Parameters initializing the simulation
/gate/run/initialize
/gate/physics/processList Enabled
/gate/physics/processList Initialized

## Parameters specifying event digitization
/gate/digitizer/Singles/insert adder
```

```
/gate/digitizer/Singles/insert readout
/gate/digitizer/Singles/readout/setDepth 1
/gate/digitizer/Singles/insert blurring
/gate/digitizer/Singles/blurring/setResolution 0.15
/gate/digitizer/Singles/blurring/setEnergyOfReference 511. keV
/gate/digitizer/Singles/insert thresholder
/gate/digitizer/Singles/thresholder/setThreshold 150. keV
/gate/digitizer/Singles/insert upholder
/gate/digitizer/Singles/upholder/setUphold 750. keV
/gate/digitizer/Singles/insert timeResolution
/gate/digitizer/Singles/timeResolution/setTimeResolution 0. ps
/gate/digitizer/Coincidences/setInputName Singles
/gate/digitizer/Coincidences/setWindow 10. ns
/gate/digitizer/Coincidences/minSectorDifference 1

## Parameters specifying result output format and filename
/gate/output/root/enable
/gate/output/root/setFileName exampleMacroFilename

## Parameters specifying simulation duration and running simulation
/gate/application/setTimeSlice 1 s
/gate/application/setTimeStart  0 s
/gate/application/setTimeStop  10 s
/gate/application/startDAQ
```

REFERENCES

[1] Abstracts of the total body pet conference 2018. *EJNMMI Physics*, 5(1):19, Jun 2018.

[2] S. Agostinelli et al. GEANT4: A Simulation toolkit. *Nucl. Instrum. Meth.*, A506:250–303, 2003.

[3] Sangtae Ahn and Jeffrey A Fessler. Globally convergent image reconstruction for emission tomography using relaxed ordered subsets algorithms. *IEEE Transactions on Medical Imaging*, 22(5):613–626, 2003.

[4] A. M. Alessio, P. E. Kinahan, and T. K. Lewellen. Modeling and incorporation of system response functions in 3d whole body pet. In *IEEE Symposium Conference Record Nuclear Science 2004.*, volume 6, pages 3992–3996 Vol. 6, Oct 2004.

[5] Hal O Anger. Scintillation camera with multichannel collimators. *Journal of Nuclear Medicine*, 5(7):515–531, 1964.

[6] National Electrical Manufacturers Association. Nema standards publication nu 2-2012: performance measurements of positron emission tomographs. Technical report, National Electrical Manufacturers Association, Rosslyn, VA, 2012.

[7] A. S. Ayan, R. Accorsi, J. S. Karp, and S. D. Metzler. Geant4 evaluation of the impact of spatial resolution improvement on the contrast recovery coefficient in a small-animal pet system with collimation. In *2009 IEEE Nuclear Science Symposium Conference Record (NSS/MIC)*, pages 2882–2887, Oct 2009.

[8] Harrison H Barrett, T White, and Lucas C Parra. List-mode likelihood. *Journal of the Optical Society of America. A, Optics, image science, and vision*, 14(11):2914–23, nov 1997.

[9] Dimitri P Bertsekas, Angelia Nedi, Asuman E Ozdaglar, et al. Convex analysis and optimization. 2003.

[10] V. Bettinardi, L. Presotto, E. Rapisarda, M. Picchio, L. Gianolli, and M. C. Gilardi. Physical performance of the new hybrid pet/ct discovery690. *Medical Physics*, 38(10):5394–5411, 9 2011.

[11] Stephen Boyd and Lieven Vandenberghe. *Convex optimization*. Cambridge university press, 2004.

[12] Ronald Newbold Bracewell and AC Riddle. Inversion of fan-beam scans in radio astronomy. *The Astrophysical Journal*, 150:427, 1967.

[13] D. Brasse, P. E. Kinahan, C. Lartizien, C. Corntat, M. Casey, C. Michel, and T. Bruckbauer. Correction methods for random coincidences in 3d wholebody pet imaging. In *2001 IEEE Nuclear Science Symposium Conference Record (Cat. No.01CH37310)*, volume 4, pages 2080–2084, 2001.

[14] R. Brun and F. Rademakers. ROOT: An object oriented data analysis framework. *Nucl. Instrum. Meth.*, A389:81–86, 1997.

[15] S. E. Brunner and D. R. Schaart. BGO as a hybrid scintillator / Cherenkov radiator for cost-effective time-of-flight PET. *Physics in Medicine and Biology*, 62(11):4421–4439, 2017.

[16] Richard E Carson, Yuchen Yan, B Chodkowski, Tieng K Yap, and Margaret E Daube-Witherspoon. Precision and accuracy of regional radioactivity quantitation using the maximum likelihood em reconstruction algorithm. *IEEE transactions on medical imaging*, 13(3):526–537, 1994.

[17] Michael Casey, Ziad Burbar, Harold Rothfuss, Vladimir Panin, and Deepak Bharkhada. A next generation sipm based pet/ct system with improved time and spatial resolution. *Journal of Nuclear Medicine*, 58(supplement 1):1332–1332, 2017.

[18] I. Castiglioni, O. Cremonesi, M. C. Gilardi, V. Bettinardi, G. Rizzo, A. Savi, E. Bellotti, and F. Fazio. Scatter correction techniques in 3d pet: A monte carlo evaluation. *IEEE Transactions on Nuclear Science*, 46(6 PART 3):2053–2058, 1999.

[19] Luca Caucci, Lars R Furenlid, and Harrison H Barrett. Maximum Likelihood Event Estimation and List-mode Image Reconstruction on GPU Hardware. *IEEE Nuclear Science Symposium conference record. Nuclear Science Symposium*, 2009(1997):4072, oct 2009.

[20] C. M. Chen, S. Y. Lee, and Z. H. Cho. Parallelization of the em algorithm for 3-d pet image reconstruction. *IEEE Transactions on Medical Imaging*, 10(4):513–522, Dec 1991.

[21] Simon R Cherry, Magnus Dahlbom, and Edward J Hoffman. 3d pet using a conventional multislice tomograph without septa. *Journal of computer assisted tomography*, 15(4):655–668, 1991.

[22] Simon R Cherry, Magnus Dahlbom, and Edward J Hoffman. Evaluation of a 3d reconstruction algorithm for multi-slice pet scanners. *Physics in Medicine & Biology*, 37(3):779, 1992.

[23] Simon R Cherry, Terry Jones, Joel S Karp, Jinyi Qi, William W Moses, and Ramsey D Badawi. Total-body pet: Maximizing sensitivity to create new opportunities for clinical research and patient care. *Journal of Nuclear Medicine*, 59(1):3–12, 2018.

[24] Neal Clinthorne, Eric Cochran, Enrico Chesi, Milan Grkovski, Borut Grošičar, Klaus Honscheid, Sam S Huh, Harris Kagan, Carlos Lacasta, Karol Brzezinski, Vladimir Linhart, Marko Mikuž, D Shane Smith, Vera Stankova, Andrej Studen, Peter Weilhammer, and Dejan Žontar. A High-Resolution PET Demonstrator using a Silicon Magnifying Glass. *Physics Procedia*, 37(0):1488–1496, 2012.

[25] N.H. Clinthorne and W.L. Rogers. Multi-resolution image reconstruction for a high-resolution small animal PET device. *2003 IEEE Nuclear Science Symposium. Conference Record (IEEE Cat. No.03CH37515)*, pages 1997–2001 Vol.3, 2003.

[26] P. Colombino, B. Fiscella, and L. Trossi. Study of positronium in water and ice from 22 to -144 °c by annihilation quanta measurements. *Il Nuovo Cimento (1955-1965)*, 38(2):707–723, Jul 1965.

[27] Magnus Dahlbom, Lars Eriksson, Goran Rosenqvist, and Christian Bohm. A study of the possibility of using multi-slice pet systems for 3d imaging. *IEEE Transactions on Nuclear Science*, 36(1):1066–1071, 1989.

[28] S. DeBenedetti, C. E. Cowan, W. R. Konneker, and H. Primakoff. On the angular distribution of two-photon annihilation radiation. *Phys. Rev.*, 77:205–212, Jan 1950.

[29] M Defrise, D Townsend, and A Geissbuhler. Implementation of three-dimensional image reconstruction for multi-ring positron tomographs. *Physics in Medicine & Biology*, 35(10):1361, 1990.

[30] Michel Defrise, Paul E Kinahan, and Christian J Michel. Image reconstruction algorithms in pet. In Dale L. Bailey, David W. Townsend, Peter E. Valk, and Michael N. Maisey, editors, *Positron Emission Tomography*, chapter 4, pages 63–91. Springer-Verlag, London, 2005.

[31] Gaspar Delso, Sebastian Frst, Bjrn Jakoby, Ralf Ladebeck, Carl Ganter, Stephan G. Nekolla, Markus Schwaiger, and Sibylle I. Ziegler. Performance measurements of the siemens mmr integrated whole-body pet/mr scanner. *Journal of Nuclear Medicine*, 52(12):1914–1922, 2011.

[32] A. P. Dempster, N. M. Laird, and D. B. Rubin. Maximum Likelihood from Incomplete Data via the EM Algorithm. *Journal of the Royal Statistical Society: Series B (Methodological)*, 39(1):1–38, 1976.

[33] S. E. Derenzo, T. F. Budinger, R. H. Huesman, J. L. Cahoon, and T. Vuletich. Imaging properties of a positron tomograph with 280 bgo crystals. *IEEE Transactions on Nuclear Science*, 28(1):81–89, Feb 1981.

[34] J a Fessler and a O Hero. Penalized maximum-likelihood image reconstruction using space-alternating generalized EM algorithms. *IEEE transactions on image processing : a publication of the IEEE Signal Processing Society*, 4(10):1417–29, jan 1995.

[35] J.A. Fessler and W.L. Rogers. Spatial resolution properties of penalized-likelihood image reconstruction: space-invariant tomographs. *IEEE Transactions on Image Processing*, 5(9):1346–1358, 1996.

[36] Nikolas P Galatsanos and Aggelos K Katsaggelos. Methods for choosing the regularization parameter and estimating the noise variance in image restoration and their relation. *IEEE Transactions on image processing*, 1(3):322–336, 1992.

[37] Sanjiv Sam Gambhir. *Molecular Imaging: A Primer*. Springer, 2009.

[38] T Goorley, M James, T Booth, F Brown, J Bull, LJ Cox, J Durkee, J Elson, M Fensin, RA Forster, et al. Initial mcnp6 release overview. *Nuclear Technology*, 180(3):298–315, 2012.

[39] Alexander M. Grant, Timothy W. Deller, Mohammad Mehdi Khalighi, Sri Harsha Maramraju, Gaspar Delso, and Craig S. Levin. Nema nu 22012 performance studies for the sipmbased tofpet component of the ge signa pet/mr system. *Medical Physics*, 43(5):2334–2343, 5 2016.

[40] S Gundacker, E Auffray, N. Di Vara, B Frisch, H Hillemanns, P Jarron, B Lang, T Meyer, S. Mosquera-Vazquez, E Vauthey, and P Lecoq. SiPM time resolution: From single photon to saturation. *Nuclear Instruments and Methods in Physics Research Section A: Accelerators, Spectrometers, Detectors and Associated Equipment*, 718:569–572, aug 2013.

[41] RL Harrison, DR Haynor, SB Gillispie, SD Vannoy, MS Kaplan, and TK Lewellen. A public-domain simulation system for emission tomography-photon tracking through heterogeneous attenuation using importance sampling. In *Journal of Nuclear Medicine*, volume 34, pages P60–P60. SOC NUCLEAR MEDICINE INC 1850 SAMUEL MORSE DR, RESTON, VA 20190-5316, 1993.

[42] TJ Herbert. Statistical stopping criteria for iterative maximum likelihood reconstruction of emission images. *Physics in Medicine & Biology*, 35(9):1221, 1990.

[43] Gabor T Herman and Dewey Odhner. Performance evaluation of an iterative image reconstruction algorithm for positron emission tomography. *IEEE transactions on medical imaging*, 10(3):336–346, 1991.

[44] Hans Herzog and Christoph Lerche. Advances in Clinical PET/MRI Instrumentation. *PET Clinics*, 11(2):95–103, 2016.

[45] Kerstin Heurling, Antoine Leuzy, My Jonasson, Andreas Frick, Eduardo R. Zimmer, Agneta Nordberg, and Mark Lubberink. Quantitative positron emission tomography in brain research. *Brain Research*, 1670:220 – 234, 2017.

[46] E. J. Hoffman, T. M. Guerrero, G. Germano, W. M. Digby, and M. Dahlbom. Pet system calibrations and corrections for quantitative and spatially accurate images. *IEEE Transactions on Nuclear Science*, 36(1):1108–1112, Feb 1989.

[47] Edward J. Hoffman, Sung Cheng Huang, Michael E. Phelps, and David E. Kuhl. Quantitation in positron emission computed tomography: 4. effect of accidental coincidences. *Journal of Computer Assisted Tomography*, 5(3):391–400, 1981.

[48] David F.C. Hsu, Ezgi Ilan, William T. Peterson, Jorge Uribe, Mark Lubberink, and Craig S. Levin. Studies of a Next-Generation Silicon-PhotomultiplierBased Time-of-Flight PET/CT System. *Journal of Nuclear Medicine*, 58(9):1511–1518, 2017.

[49] H M Hudson and R S Larkin. Accelerated image reconstruction using ordered subsets of projection data. *IEEE transactions on medical imaging*, 13(4):601–9, jan 1994.

[50] Leonardo Iaccarino, Arianna Sala, Silvia Paola Caminiti, and Daniela Perani. The emerging role of pet imaging in dementia. *F1000Research*, 6, 2017.

[51] Zhang J, Miller M, and Knopp MV. Sufi55: Performance evaluation of digital pet/ct: Medical physics basis for the clinical applications. *Medical Physics*, 43(6Part8):3399–3399, 2016.

[52] S Jan, G Santin, D Strul, S Staelens, K Assié, D Autret, S Avner, R Barbier, M Bardiès, P M Bloomfield, D Brasse, V Breton, P Bruyndonckx, I Buvat, a F Chatziioannou, Y Choi, Y H Chung, C Comtat, D Donnarieix, L Ferrer, S J Glick, C J Groiselle, D Guez, P-F Honore, S Kerhoas-Cavata, a S Kirov, V Kohli, M Koole, M Krieguer, D J Van Der Laan, F Lamare, G Largeron, C Lartizien, D Lazaro, M C Maas, L Maigne, F Mayet, F Melot, C Merheb, E Pennacchio, J Perez, U Pietrzyk, F R Rannou, M Rey, D R Schaart, C R Schmidtlein, L Simon, T Y Song, J-M Vieira, D Visvikis, R Van De Walle, E Wieërs, and C Morel. GATE: a simulation toolkit for PET and SPECT. *Physics in Medicine and Biology*, 49(19):4543–4561, oct 2004.

[53] Jian Zhou and Jinyi Qi. Adaptive Imaging for Lesion Detection Using a Zoom-in PET System. *IEEE Transactions on Medical Imaging*, 30(1):119–130, jan 2011.

[54] C. A. Johnson, Yuchen Yan, R. E. Carson, R. L. Martino, and M. E. Daube-Witherspoon. A system for the 3d reconstruction of retracted-septa pet data using the em algorithm. *IEEE Transactions on Nuclear Science*, 42(4):1223–1227, Aug 1995.

[55] Chien-Min Kao. *Pre-reconstruction sinogram restoration for positron emission tomography*. PhD thesis, University of Chicago, 1997.

[56] Nicolaos B Karayiannis and Anastasios N Venetsanopoulos. Regularization theory in image restoration-the stabilizing functional approach. *IEEE Transactions on Acoustics, Speech, and Signal Processing*, 38(7):1155–1179, 1990.

[57] Joel S Karp, Gerd Muehllehner, D A MankofF, Caesar E Ordonez, J M Ollinger, M E Daube-Witherspoon, Arthur T Haigh, and Daniel J Beerbohm. Continuous-slice PENN-PET: a positron tomograph with volume imaging capability. *Journal of Nuclear Medicine*, 31(5):617–27, 1990.

[58] Sue C Kaste. Pet-ct in children: where is it appropriate? *Pediatric radiology*, 41(2):509, 2011.

[59] Daniel B Keesing, Aswin Mathews, Sergey Komarov, Heyu Wu, Tae Yong Song, Joseph a O'Sullivan, and Yuan-Chuan Tai. Image reconstruction and system modeling techniques for virtual-pinhole PET insert systems. *Physics in medicine and biology*, 57(9):2517–38, may 2012.

[60] Misha E Kilmer and Dianne P O'Leary. Choosing regularization parameters in iterative methods for ill-posed problems. *SIAM Journal on matrix analysis and applications*, 22(4):1204–1221, 2001.

[61] Paul E Kinahan, Michel Defrise, and Rolf Clackdoyle. Analytic image reconstruction methods. In Miles Wernick and John Aarsvold, editors, *Emission Tomography*, chapter 20, pages 421–442. Academic Press, Cambridge, Massachusetts, 2004.

[62] Jeffrey A Kolthammer, Kuan-Hao Su, Anu Grover, Manoj Narayanan, David W Jordan, and Raymond F Muzic. Performance evaluation of the ingenuity tf pet/ct scanner with a focus on high count-rate conditions. *Physics in Medicine & Biology*, 59(14):3843, 2014.

[63] Sergey A. Komarov, Heyu Wu, Daniel B. Keesing, Joseph A. O'Sullivan, and Yuan Chuan Tai. Compton scattering in clinical PET/CT with high resolution half ring PET insert device. *IEEE Transactions on Nuclear Science*, 57(3 PART 1):1045–1051, 2010.

[64] Sun Il Kwon, Alberto Gola, Alessandro Ferri, Claudio Piemonte, and Simon R. Cherry. Bismuth germanate coupled to near ultraviolet silicon photomultipliers for time-of-flight PET. *Physics in Medicine and Biology*, 61(18):L38–L47, 2016.

[65] David S. Lalush and Miles N. Wernick. Image reconstruction algorithms in pet. In Miles N. Wernick and John Aarsvold, editors, *Emission Tomography*, chapter 21, pages 443–472. Academic Press, Cambridge, Massachusetts, 2004.

[66] Kenneth Lange and Richard Carson. EM Reconstruction Algorithms for Emission and Transmission Tomography. *Journal of Computer Assisted Tomography*, 8(2):306–316, 1984.

[67] Tom K Lewellen. Recent developments in PET detector technology. *Physics in medicine and biology*, 53(17):R287–317, sep 2008.

[68] X. Li, A. M. Alessio, T. H. Burnett, T. K. Lewellen, and R. Miyaoka. Performance evaluation of small animal pet scanners with different system designs. *IEEE Transactions on Nuclear Science*, 60(3):1495–1502, June 2013.

[69] Jeih-S Liow and SC Strother. The convergence of object dependent resolution in maximum likelihood based tomographic image reconstruction. *Physics in Medicine & Biology*, 38(1):55, 1993.

[70] Jingjing Liu, Chien-Min Kao, Shuguo Gu, Peng Xiao, and Qingguo Xie. A PET system design by using mixed detectors: resolution properties. *Physics in Medicine and Biology*, 59(13):3517–3532, jul 2014.

[71] Aswin John Mathews, Sergey Komarov, Heyu Wu, Joseph a O'Sullivan, and Yuan-Chuan Tai. Improving PET imaging for breast cancer using virtual pinhole PET half-ring insert. *Physics in medicine and biology*, 58(18):6407–27, 2013.

[72] Aswin John Mathews, Ke Li, Sergey Komarov, Qiang Wang, Bosky Ravindranath, Joseph A. O'Sullivan, and Yuan-Chuan Tai. A generalized reconstruction framework for unconventional PET systems. *Medical Physics*, 42(8):4591–4609, jul 2015.

[73] Michael Miller, Jun Zhang, Katherine Binzel, Jerome Griesmer, Thomas Laurence, Manoj Narayanan, Deepa Natarajamani, Sharon Wang, and Michael Knopp. Characterization of the vereos digital photon counting pet system. *Journal of Nuclear Medicine*, 56(supplement 3):434–434, 2015.

[74] William W. Moses. Fundamental limits of spatial resolution in PET. *Nuclear Instruments and Methods in Physics Research, Section A: Accelerators, Spectrometers, Detectors and Associated Equipment*, 648(SUPPL. 1):S236–S240, 2011.

[75] E. U. Mumcuoglu, R. M. Leahy, S. R. Cherry, and E. Hoffman. Accurate geometric and physical response modelling for statistical image reconstruction in high resolution pet. In *1996 IEEE Nuclear Science Symposium. Conference Record*, volume 3, pages 1569–1573 vol.3, Nov 1996.

[76] National Electrical Manufacturers Association. NEMA Standard Publication NU 4-2008: Performance Measurements of Small Animal Positron Emission Tomographs. Technical report, National Electrical Manufacturers Association, Rosslyn, VA, 2008.

[77] Josep F. Oliver and M. Rafecas. Modelling random coincidences in positron emission tomography by using singles and prompts: A comparison study. *PLOS ONE*, 11(9):1–22, 09 2016.

[78] Debashish Pal. *Image reconstruction for a high resolution PET-insert scanner*. PhD thesis, Washington University in St. Louis, 2008.

[79] V. Y. Panin, F. Kehren, C. Michel, and M. Casey. Fully 3-d pet reconstruction with system matrix derived from point source measurements. *IEEE Transactions on Medical Imaging*, 25(7):907–921, July 2006.

[80] S Park, W L Rogers, N H Clinthorne, Keywords Egs, and Compton Pet. Effect of Recoil Electron Range on Efficiency and on Spatial Resolution of Very High Resolution Animal PET. *Energy*, 00(C):2–5, 2002.

[81] Sang-June Park, W Leslie Rogers, and Neal H Clinthorne. Design of a very high-resolution small animal PET scanner using a silicon scatter detector insert. *Physics in medicine and biology*, 52(15):4653–77, 2007.

[82] L Parra and H H Barrett. List-mode likelihood: EM algorithm and image quality estimation demonstrated on 2-D PET. *IEEE transactions on medical imaging*, 17(2):228–35, apr 1998.

[83] Maria Picchio and Paolo Castellucci. Clinical indications of 11c-choline pet/ct in prostate cancer patients with biochemical relapse. *Theranostics*, 2(3):313, 2012.

[84] Jinyi Qi, R. M. Leahy, Chinghan Hsu, T. H. Farquhar, and S. R. Cherry. Fully 3d bayesian image reconstruction for the ecat exact hr+. *IEEE Transactions on Nuclear Science*, 45(3):1096–1103, Jun 1998.

[85] Jinyi Qi, Richard M Leahy, Simon R Cherry, Arion Chatziioannou, and Thomas H Farquhar. High-resolution 3d bayesian image reconstruction using the micropet small-animal scanner. *Physics in Medicine & Biology*, 43(4):1001, 1998.

[86] Jinyi Qi, Yongfeng Yang, Jian Zhou, Yibao Wu, and Simon R Cherry. Experimental assessment of resolution improvement of a zoom-in PET. *Physics in Medicine and Biology*, 56(17):N165–N174, sep 2011.

[87] J. Radon. On the determination of functions from their integral values along certain manifolds. *IEEE Transactions on Medical Imaging*, 5(4):170–176, Dec 1986.

[88] Johann Radon. Uber die bestimmung von funktionen durch ihre integralwerte langs gewissez mannigfaltigheiten, ber. *Verh. Sachs. Akad. Wiss. Leipzig, Math Phys Klass*, 69, 1917.

[89] A. Rahmim, M. Lenox, C. Michel, A. J. Reader, and V. Sossi. Space-variant and anisotropic resolution modeling in list-mode em reconstruction. In *2003 IEEE Nuclear Science Symposium. Conference Record (IEEE Cat. No.03CH37515)*, volume 5, pages 3074–3077 Vol.5, Oct 2003.

[90] Ivo Rausch, Jacobo Cal-González, David Dapra, Hans Jürgen Gallowitsch, Peter Lind, Thomas Beyer, and Gregory Minear. Performance evaluation of the Biograph mCT Flow PET/CT system according to the NEMA NU2-2012 standard. *EJNMMI Physics*, 2(1):1–17, 2015.

[91] A.J. Reader, P.J. Julyan, H. Williams, D.L. Hastings, and J. Zweit. EM Algorithm System Modeling by Image-Space Techniques for PET Reconstruction. *IEEE Transactions on Nuclear Science*, 50(5):1392–1397, oct 2003.

[92] Gabriel Reynés-Llompart, Cristina Gámez-Cenzano, Inmaculada Romero-Zayas, Laura Rodríguez-Bel, José L. Vercher-Conejero, and Josep M. Martí-Climent. Performance Characteristics of the Whole-Body Discovery IQ PET/CT System. *Journal of Nuclear Medicine*, 58(7):1155–1161, 2017.

[93] Emilie Roncali and Simon R Cherry. Application of silicon photomultipliers to positron emission tomography. *Annals of biomedical engineering*, 39(4):1358–77, apr 2011.

[94] Steve Ross. Q. clear. *GE Healthcare, White Paper*, pages 1–9, 2014.

[95] Pierre C Sabatier. Past and future of inverse problems. *Journal of Mathematical Physics*, 41(6):4082–4124, 2000.

[96] V. V. Selivanov, Y. Picard, J. Cadorette, S. Rodrigue, and R. Lecomte. Detector response models for statistical iterative image reconstruction in high resolution pet. *IEEE Transactions on Nuclear Science*, 47(3):1168–1175, Jun 2000.

[97] Vitali V. Selivanov, Martin D. Lepage, and Roger Lecomte. List-mode image reconstruction for real-time PET imaging. *Journal of Visual Communication and Image Representation*, 17(3):630–646, jun 2006.

[98] J. Sempau, E. Acosta, J. Bar, J. M. Fernndez-Varea, and F. Salvat. An algorithm for monte carlo simulation of coupled electron-photon transport. *Nuclear Instruments and Methods in Physics Research, Section B: Beam Interactions with Materials and Atoms*, 132(3):377–390, 1997.

[99] L. A. Shepp and Y. Vardi. Maximum likelihood reconstruction for emission tomography. *IEEE transactions on medical imaging*, MI-1(2):113 – 122, 1982.

[100] Robert L. Siddon. Fast calculation of the exact radiological path for a three-dimensional CT array. *Medical Physics*, 12(2):252, 1985.

[101] D. L. Snyder, M. I. Miller, L. J. Thomas, and D. G. Politte. Noise and edge artifacts in maximum-likelihood reconstructions for emission tomography. *IEEE Transactions on Medical Imaging*, 6(3):228–238, Sept 1987.

[102] C. W. Stearns, D. L. McDaniel, S. G. Kohlmyer, P. R. Arul, B. P. Geiser, and V. Shanmugam. Random coincidence estimation from single event rates on the discovery st pet/ct scanner. In *2003 IEEE Nuclear Science Symposium. Conference Record (IEEE Cat. No.03CH37515)*, volume 5, pages 3067–3069 Vol.5, Oct 2003.

[103] S. C. Strother, M. E. Casey, and E. J. Hoffman. Measuring pet scanner sensitivity: relating countrates to image signal-to-noise ratios using noise equivalents counts. *IEEE Transactions on Nuclear Science*, 37(2):783–788, Apr 1990.

[104] A. Studen, D. Burdette, E. Chesi, V. Cindro, N. H. Clinthorne, E. Cochran, B. Grošičar, H. Kagan, C. Lacasta, V. Linhart, M. Mikuž, V. Stankova, P. Weilhammer, and D. Žontar. Timing performance of the silicon PET insert probe. *Radiation Protection Dosimetry*, 139(1-3):199–203, 2010.

[105] F. C. Sureau, A. J. Reader, C. Comtat, C. Leroy, M.-J. Ribeiro, I. Buvat, and R. Trebossen. Impact of Image-Space Resolution Modeling for Studies with the High-Resolution Research Tomograph. *Journal of Nuclear Medicine*, 49(6):1000–1008, 2008.

[106] Yuan-Chuan Tai, Heyu Wu, Debashish Pal, and Joseph a O'Sullivan. Virtual-pinhole PET. *Journal of nuclear medicine : official publication, Society of Nuclear Medicine*, 49(3):471–9, mar 2008.

[107] Demetri Terzopoulos. Regularization of inverse visual problems involving discontinuities. *IEEE Transactions on pattern analysis and Machine Intelligence*, 8(4):413–424, 1986.

[108] Lampros Theodorakis, George Loudos, Vasilios Prassopoulos, Constantin Kappas, Ioannis Tsougos, and Panagiotis Georgoulias. A review of PET normalization: striving for count rate uniformity. *Nuclear medicine communications*, 34(11):1033–45, nov 2013.

[109] DM Titterington. General structure of regularization procedures in image reconstruction. *Astronomy and Astrophysics*, 144:381, 1985.

[110] D. W. Townsend, L. G. Byars, M. Defrise, A. Geissbuhler, R. P. Maguire, J. Missirner, R. Roddy, T. Brun, M. A. Mintun, and R. Nutt. Design and performance of a rotating positron tomograph, rpt-2. In *1993 IEEE Conference Record Nuclear Science Symposium and Medical Imaging Conference*, pages 1058–1062, Oct 1993.

[111] David W Townsend, Roberto A Isoardi, and Bernard Bendriem. Volume imaging tomographs. In *The theory and practice of 3D PET*, pages 111–132. Springer, 1998.

[112] DW Townsend, T Sprinks, T Jones, A Geissbuhler, M Defrise, MC Gilardi, and J Heather. Three dimensional reconstruction of pet data from a multi-ring camera. *IEEE Transactions on Nuclear Science*, 36(1):1056–1065, 1989.

[113] S. Vandenberghe, E. Mikhaylova, E. D'Hoe, P. Mollet, and J. S. Karp. Recent developments in time-of-flight PET. *EJNMMI Physics*, 3(1), 2016.

[114] Eugene Veklerov and Jorge Llacer. Stopping rule for the mle algorithm based on statistical hypothesis testing. *IEEE Transactions on Medical Imaging*, 6(4):313–319, 1987.

[115] Luyao Wang, Jun Zhu, Xiao Liang, Ming Niu, Xiaoke Wu, Chien-Min Kao, Heejong Kim, and Qingguo Xie. Performance evaluation of the trans-pet® biocaliburn® lh system: a large fov small-animal pet system. *Physics in Medicine & Biology*, 60(1):137, 2014.

[116] Luyao Wang, Jun Zhu, Xiao Liang, Ming Niu, Xiaoke Wu, Chien-Min Kao, Heejong Kim, and Qingguo Xie. Performance evaluation of the Trans-PET(®) BioCaliburn(®) LH system: a large FOV small-animal PET system. *Physics in medicine and biology*, 60(1):137–150, 2015.

[117] Miles N. Wernick and John Aarsvold. Introduction to emission tomography. In Miles Wernick and John Aarsvold, editors, *Emission Tomography*, chapter 2, pages 11–23. Academic Press, Cambridge, Massachusetts, 2004.

[118] Donald W Wilson and Benjamin MW Tsui. Noise properties of filtered-backprojection and ml-em reconstructed emission tomographic images. *IEEE transactions on nuclear science*, 40(4):1198–1203, 1993.

[119] H. Wu, D. Pal, J. a. O'Sullivan, and Y.-C. Tai. A Feasibility Study of a Prototype PET Insert Device to Convert a General-Purpose Animal PET Scanner to Higher Resolution. *Journal of Nuclear Medicine*, 49(1):79–87, 2007.

[120] H. Wu, D. Pal, T. Y. Song, J. a. O'Sullivan, and Y.-C. Tai. Micro Insert: A Prototype Full-Ring PET Device for Improving the Image Resolution of a Small-Animal PET Scanner. *Journal of Nuclear Medicine*, 49(10):1668–1676, 2008.

[121] Daoming Xi, Chen Zeng, Wei Liu, Xiang Liu, Lu Wan, Heejong Kim, Luyao Wang, Chien Min Kao, and Qingguo Xie. A PET detector module using FPGA-only MVT digitizers. *IEEE Nuclear Science Symposium Conference Record*, pages 2–6, 2013.

[122] Q. Xie, L. Wang, J. Zhu, Y. Chen, J. Liu, M. Niu, X. Chen, Z. Wu, D. Xi, Z. Hu, B. Li, Y. Zheng, and P. Xiao. Development and initial performance measurements of trans-pet biocaliburn sh1.0. In *2012 IEEE Nuclear Science Symposium and Medical Imaging Conference Record (NSS/MIC)*, pages 3090–3092, Oct 2012.

[123] Xie, Qingguo, Chen, Yuanbao, Zhu, Jun, Liu, Jingjing, Wang, Xi, Liu, Wei, Chen, Xin, Niu, Ming, Wu, Zhongyi, Xi, Daoming, Wang, Luyao, Xiao, Peng, Chen, Chin Tu, and Kao, Chien Min. Implementation of LYSO/PSPMT block detector with all digital DAQ system. *IEEE Transactions on Nuclear Science*, 60(3):1487–1494, 2013.

[124] Soichiro Yoshida, Kazuaki Nakagomi, Shuichi Goto, Masami Futatsubashi, and Tatsuo Torizuka. 11c-choline positron emission tomography in prostate cancer: primary staging and recurrent site staging. *Urologia internationalis*, 74(3):214–220, 2005.

[125] Habib Zaidi and Kenneth F. Koral. Scatter modelling and compensation in emission tomography. *European Journal of Nuclear Medicine and Molecular Imaging*, 31(5):761–782, 2004.

[126] Habib Zaidi and Marie Louise Montandon. Scatter Compensation Techniques in PET. *PET Clinics*, 2(2):219–234, 2007.

[127] Jian Zhou and Jinyi Qi. Theoretical analysis and simulation study of a high-resolution zoom-in PET system. *Physics in medicine and biology*, 54(17):5193–208, sep 2009.

[128] Jun Zhu, Luyao Wang, Chien-Min Kao, Heejong Kim, and Qingguo Xie. Performance evaluation of the trans-petbiocaliburn sh system. *Nuclear Instruments and Methods in Physics Research Section A: Accelerators, Spectrometers, Detectors and Associated Equipment*, 777:148 – 153, 2015.